NTNU – Trondheim
Norwegian University of
Science and Technology

Tidal Boundary Layer Flow in Coastal Zones

Einar Kristiansen
Grønningsæter

Marine Technology
Submission date: June 2015
Supervisor: Dag Myrhaug, IMT
Co-supervisor: Forsker Lars Erik Holmedal, IMT

Norwegian University of Science and Technology
Department of Marine Technology

NTNU Trondheim
Norwegian University of Science and Technology
Department of Marine Technology – Group of Marine Structures

MASTER THESIS IN MARINE TECHNOLOGY

SPRING 2015

FOR

STUD. TECHN. EINAR K. GRØNNINGSÆTER

TIDAL BOUNDARY LAYER FLOW IN COASTAL ZONES

Tidal boundary layer flow in the ocean is of fundamental interest as it is important for transport of e.g. plankton, larvae, contaminated ballast water from ships, oil spills and sea bottom material. These flow components also represent important contributions in physical models for predicting flow circulations in coastal zones and on continental shelves.

The student shall:

1. Give an overview of the mechanisms generating and governing the tidal flows.
2. Give an overview of atmosphere-ocean interaction effects that may generate currents or interact with the tidal currents.
3. Investigate the tidal flow by using a one-dimensional two-equation turbulence closure model by first giving a background description of turbulence modelling and the computational tool.
4. Perform numerical simulations of tidal flow by comparing with field measurements from the Hebrides, including analysis and discussion of the results.

The work scope may prove to be larger than initially anticipated. Subject to approval from the supervisor, topics may be deleted from the list above or reduced in extent.

In the thesis the candidate shall present her personal contribution to the resolution of problem within the scope of the thesis work.

Theories and conclusions should be based on mathematical derivations and/or logic reasoning identifying the various steps in the deduction.

The candidate should utilize the existing possibilities for obtaining relevant literature.

The thesis should be organized in a rational manner to give a clear exposition of results, assessments, and conclusions. The text should be brief and to the point, with a clear language. Telegraphic language should be avoided.

The thesis shall contain the following elements: A text defining the scope, preface, list of contents, summary, main body of thesis, conclusions with recommendations for further work, list of symbols and acronyms, reference and (optional) appendices. All figures, tables and equations shall be numerated.

The supervisor may require that the candidate, in an early stage of the work, present a written plan for the completion of the work. The plan should include a budget for the use of computer and laboratory resources that will be charged to the department. Overruns shall be reported to the supervisor.

The original contribution of the candidate and material taken from other sources shall be clearly defined. Work from other sources shall be properly referenced using an acknowledged referencing system.

The thesis shall be submitted in two copies:

- Signed by the candidate
- The text defining the scope included
- In bound volume(s)
- Drawings and/or computer prints which cannot be bound should be organized in a separate folder.

Advisors: Research Professor Lars Erik Holmedal
Professor Dag Myrhaug

Deadline: 10.06.2015

Dag Myrhaug
Supervisor

Preface

This master thesis was written during the spring of 2015 at the Department of Marine Technology at the Norwegian University of Science and Technology. The thesis is the concluding work for the Master of Science degree in Marine Technology.

The process of writing this thesis and performing the analyses presented has been very educational. I have improved my understanding of hydrodynamics in general and physical oceanography in particular. I have also improved my skills with regards to programming and scientific writing. The choice of tides and tidal flow as subject was made because I am fascinated by nature and was intrigued by the possibility of studying the fundamental mechanisms governing oceanic motions.

I would like to express my gratitude towards my supervisor Professor Dag Myrhaug for his guidance throughout the semester. He has been an invaluable resource of expertise in oceanography, and I have felt welcome with all my questions. I would also like to thank my co-supervisor Professor Lars Erik Holmedal for his guidance and for providing me with the numerical model he developed during his doctoral thesis work. I also want to thank postdoctoral researcher Hong Wang for her contributions to our discussions. Without the help of these three, finding the appropriate paths of research and analyzing would have been much more difficult. Further, I would like to thank Arne Vögler, James Morrison, David Christie and Donald Armstrong, all from the University of the Highlands and Islands, for providing me with the field data that makes up the basis for the thesis.

Finally, I want to thank my friends and fellow students, especially the members of office A1.015 for being knowledgeable discussion partners and for making the past year a memorable year also non-academically.

Trondheim, June 9, 2015

Einar Grønningsæter

Summary

A one-dimensional hydrodynamic model with a two-equation turbulence closure has been used to model shallow-water tidal flow over a complex bottom. The intention was to investigate the applicability of the model on tidal flow in coastal zones, where effects of bottom conditions and constrictions due to coastlines and underwater topography are important. This is of interest because near-shore tidal flows are important for transport of biological material and pollutants. In addition, the present model and similar models are time-efficient and require little computational power. The turbulence closure known as the $k-\epsilon$ model was used.

Field data of current velocities and surface elevation measured outside the coast of the Hebrides, Scotland, have been processed and applied to the model. Frequency spectra of the current were calculated, and the main tidal constituents were identified. The velocity signals were filtered digitally to remove components not related to the tides. It was found that such components were present also in the range of tidal frequencies. These components could not be removed.

The model was run with the filtered field velocities at a specific height above the bottom as input. The filtered velocities in four points through the water column were used as references to assess the model results. The effect of the specified bottom roughness was investigated. Impacts of wind and wave conditions and tidal range (the vertical distance between low and high tide) on the model's accuracy were assessed. The former is of interest because effects of atmospheric conditions are believed to make up the most part of current contributions not induced by tides in the filtered data. The latter is of interest because the model assumes a constant water depth.

A bottom roughness of z_0 = 0.0006 cm was found to give the best results. With this roughness, the velocities at a specific vertical position was modeled with very good accuracy. The damping of the flow towards the bottom, however, was much smaller than in the field data. The damping in the field data is very strong. The main reason for this is believed to be the presence of tall seaweed at the bottom, together with boulders. It was found that the predicted boundary layer matched an empirical formula better than what the field data did.

With a bottom roughness of z_0 = 0.050 cm, the predicted boundary layer was a very good fit to the formula. The flow state was found to be hydrodynamically rough with this roughness, and smooth for z_0 = 0.0006 cm, which also indicates that the former roughness gives a more realistic damping than the latter. The velocity profile described by the formula is constant through the upper half of the water column, unlike the profiles in the field data. The formula has previously been verified against field measurements including shallow-water flow. Hence, we know that tidal flows may exhibit such boundary layers also in shallow water.

A tendency indicating that increasing wave activity decreases the model's accuracy was found, but a conclusion could not be drawn, because the accuracy difference was small. So was the difference between periods of low and high tidal ranges. A tendency was found, however, that for high tidal ranges, the tidal ellipses were rotated clockwise relative to the field data. This corresponds to the conclusions of the pre-master project thesis.

The main conclusion is that the results are relatively good, the simplicity and efficiency of the model taken into account. In its present form, the model is not applicable for predictions of transport of biological material, pollutants or other material in the specific complex conditions in the present field data. However, the results indicate that the model might be able to model shallow-water tidal flow boundary layers with better accuracy than obtained here, if the conditions are less complex. It is proposed that further works may assess this indication, and address the different types of boundary layers found in coastal tidal flows. An attempt of implementing the effect of seaweed in the model could also be made, as this is assumed to be the main reason for the discrepancies between the field data and the model results.

Sammendrag

Tidevannsstrømning på grunt vann over en kompleks bunn er modellert med en endimensjonal hydrodynamisk modell. En $k-\epsilon$-turbulensmodell er inkludert i modellen. Intensjonen har vært å undersøke hvorvidt modellen kan modellere tidevannsstrømning i kystområder, der bunnforhold, nærhet til kyst og bunntopografi påvirker strømningen i stor grad. Dette er av interesse fordi tidevannsstrømning i kystområder er viktig for transport av biologisk materiale og forurensende stoffer. I tillegg er modellen og liknende modeller tidsbesparende og krever lite datakraft.

Feltmålinger av strømhastigheter og overflatehevning utenfor kysten av Hebridene, Skottland, har blitt prosessert og benyttet i modellen. Frekvensspektra for strømhastighetene ble beregnet, og de viktigste tidevannskomponentene identifisert. Hastighetssignalene ble filtrert digitalt for å fjerne komponenter generert av andre effekter enn tidevann. Slike hastighetskomponenter ble imidlertid også påvist i frekvensområdet til tidevannet. Disse kunne derfor ikke fjernes.

Filtrerte strømhastigheter fra en gitt høyde over bunnen ble brukt som inndata i modellen. Filtrerte hastigheter ved fire ulike høyder gjennom vannsøylen ble brukt som sammenlikningsgrunnlag for å vurdere modellresultatene. Effekt av spesifisert bunnruhet ble undersøkt. Effekt av vind- og bølgeforhold på modellens nøyaktighet ble studert, fordi de uønskede hastighetskomponentene i de filtrerte signalene trolig er indirekte generert av atmosfæriske forhold. I tillegg ble effekt av vertikal avstand mellom flo og fjære (med ekstremverdier ved springflo og nippflo), undersøkt. Dette er av interesse fordi modellen antar konstant vanndyp.

De beste resultatene ble oppnådd med en bunnruhet $z_0 = 0.0006$ cm. Med denne ruheten ble hastighetene ved en gitt høyde over bunnen modellert med veldig god nøyaktighet. Dempingen av strømningen mot bunnen var imidlertid mye svakere enn i feltmålingene. Dempingen i feltmålingene er veldig sterk, noe som antas å være et resultat av høy vegetasjon og steiner på bunnen. Grensesjiktet predikert av modellen ble påvist å samsvare bedre med en empirisk formel enn hva grensesjiktet i feltmålingene gjør. Med en spesifisert bunnruhet $z_0 = 0.050$ cm var overensstemmelsen mellom hastighetsprofilene fra modellresultatene og fra målingene

veldig god. Det ble videre påvist at denne ruheten gav en hydrodynamisk ru strømning, mens z_0 = 0.0006 cm gav en hydrodynamisk glatt strømning, noe som også indikerer at z_0 = 0.050 cm gir en mer realistisk demping av strømningen mot bunnen. Hastighetsprofilet beskrevet av formelen er konstant gjennom den øvre halvdelen av vannsøylen. Formelen har tidligere blitt verifisert ved å sammenlikne med ulike feltdata, inkludert målinger fra grunt vann. Det er altså kjent at også tidevannsstrømning på grunt vann kan ha et slikt hastighetsprofil.

Det ble funnet indikasjoner på at økende bølgeaktivitet kan ha en negativ effekt på modellens nøyaktighet, men disse var for svake til at det kunne konkluderes. Effekten av vertikal avstand mellom flo og fjære var veldig liten. Det ble imidlertid funnet en tendens til at de modellerte tidevannsellipsene ble rotert med klokken ved stor vertikal avstand. Dette samsvarer med konklusjonene fra prosjektoppgaven skrevet som et forarbeid til denne oppgaven.

Oppgavens hovedkonklusjon er at resultatene er relativt gode, tatt i betraktning at modellen er svært effektiv og enkel. I dens nåværende form er den ikke egnet til å beregne transport av biologisk materiale, forurensende stoffer og liknende for de spesifikke komplekse forholdene vi har i feltmålingene. Resultatene indikerer imidlertid at modellen kan være i stand til å predikere tidevannsstrømning på grunt vann med bedre nøyaktighet enn hva det er oppnådd i dette arbeidet, under mindre komplekse forhold. Det foreslås at fremtidige arbeider kan undersøke denne indikasjonen, og ta i betraktning de ulike typer grensesjikt som opptrer i tidevannsstrømning i kystområder. Man kan også forsøke å implementere effekten av vegetasjon på bunnen i modellen, da dette antas å være hovedårsaken til avvikene mellom feltdataene og modellresultatene.

Contents

1 Introduction **1**

2 Tides **3**

2.1 Equilibrium model . . . 3

2.1.1 Lunar tides . . . 3

2.1.2 Combined lunar and solar tides . . . 8

2.2 Dynamic model . . . 11

2.3 Tidal prediction, harmonic constituents and tidal patterns . . . 13

2.4 Tidal currents . . . 15

2.5 Shallow-water effects . . . 17

2.5.1 Direct effects of bathymetry and coastal geometry . . . 17

2.5.2 Interaction with hydrodynamic phenomena . . . 21

3 Atmosphere-ocean interaction **23**

3.1 Wave-induced current . . . 23

3.1.1 Eulerian mass transport . . . 23

3.1.2 Lagrangian mass transport . . . 24

3.1.3 Longshore currents and rip currents . . . 26

3.2 Wind-induced current . . . 28

3.2.1 The Ekman layer . . . 29

3.2.2 The relation between theoretical and observed Ekman layers . . . 30

3.3 Wave-current interaction . . . 32

4 Turbulence and turbulence modeling **35**

4.1 Reynolds stress models . . . 36

4.2 Generalized eddy viscosity . . . 37

4.3 Turbulent-flow simulation methods . . . 41

4.4 Roughness effects and flow regimes . . . 41

5 Model formulation **43**

5.1 Governing equations . . . 43

5.2 Boundary conditions . . . 44
5.2.1 At the seabed . . . 44
5.2.2 At the surface . . . 44
5.3 Forcing function . . . 45
5.4 Numerical method . . . 45

6 Field data **47**
6.1 Data splining and filtering . . . 50
6.2 Vertical velocity . . . 59
6.3 Residual current . . . 62

7 Results and discussion **67**
7.1 Previous work . . . 67
7.2 Model setup . . . 67
7.3 Choice of bottom roughness . . . 68
7.4 Vertical current speed profiles . . . 75
7.5 Flow regime . . . 79
7.6 Effect of wind and wave conditions . . . 80
7.7 Effect of tidal range . . . 88

8 Conclusions **95**

9 Recommendations for further work **97**

Bibliography **99**

Appendices **I**

A Time series of model results with other bottom roughness values **III**

B Velocity plots in the horizontal plane **XIII**
B.1 Effect of bottom roughness . . . XIV
B.2 Effect of tidal range . . . XVI

C Results and conclusions from pre-master project work **XVII**

C.1 Verification of the model XVIII

C.2 Effect of bottom roughness XVIII

C.3 Effect of water depth XXI

C.4 Conclusions XXVII

D Deduction of the surface Ekman layer **XXIX**

List of Figures

1 Earth-moon system 5
2 Distribution of tide-generating forces on the earth in the equilibrium model . . 7
3 Tidal bulges in the equilibrium model 7
4 Effect of lunar declination 8
5 Interaction of lunar and solar tides in the equilibrium model 10
6 The dynamic model 12
7 Amphidromic systems in the North Sea 13
8 Types of tide 15
9 Tidal ellipse 17
10 Kelvin wave 19
11 Shelf wave 20
12 Lagrangian mass transport 25
13 Rip current structure 28
14 Ekman surface spiral with constant eddy viscosity 31
15 Wave-current interaction 33
16 Turbulent boundary layer over a flat plate 35
17 AWAC current and wave measuring system at seabed 47
18 Topographic maps of the measuring location 49
19 Satellite photo of the measuring location 50
20 Surface elevation during February and May 2013 51
21 Tidal component of the surface elevation during February and May 2013 52
22 Surface elevation during February 2013, long time series 53
23 Surface elevation during May 2013, long time series 54
24 Frequency spectra of the unfiltered velocities 56
25 Frequency spectrum with tidal components 57
26 Frequency spectra of the filtered velocities 57
27 Filtered and unfiltered velocities of the field measurements 58
28 Unfiltered velocities u, v, w of February 60
29 Unfiltered velocities u, v, w of May 61

30 Residual current of field data 64
31 Mean wind velocity 65
32 Squared error of the model results, February 70
33 Squared error of the model results, May 70
34 Model results and field data February, cell 1 and 2 71
35 Model results and field data February, cell 3 and 4 72
36 Model results and field data May, cell 1 and 2 73
37 Model results and field data May, cell 3 and 4 74
38 Mean current speed profiles compared with empirical formula 77
39 Mean current speed profiles for different bottom roughnesses compared with empirical formula 78
40 Model results and field data velocities during small wave activity, February . . . 82
41 Model results and field data velocities during high wave activity, February . . . 83
42 Model results and field data velocities during small wave activity, May 84
43 Model results and field data velocities during high wave activity, May 85
44 Mean turbulent kinetic energy profiles for different wave heights 86
45 Shear stress profiles for different wave conditions 87
46 Mean current speed profiles for periods of low and high wave activity 87
47 Model results and field data velocities during high tidal range, February 90
48 Model results and field data velocities during low tidal range, February 91
49 Model results and field data velocities during high tidal range, May 92
50 Model results and field data velocities during low tidal range, May 93
51 Mean turbulent kinetic energy profiles for different tidal ranges 94
52 Mean current speed profiles for periods of low and high tidal range 94
53 Model results and field data February, $z_0 = 0.010cm$, cell 1 and 2 IV
54 Model results and field data February, $z_0 = 0.010cm$, cell 3 and 4 V
55 Model results and field data February, $z_0 = 0.050cm$, cell 1 and 2 VI
56 Model results and field data February, $z_0 = 0.050cm$, cell 3 and 4 VII
57 Model results and field data May, $z_0 = 0.010cm$, cell 1 and 2 VIII
58 Model results and field data May, $z_0 = 0.010cm$, cell 3 and 4 IX
59 Model results and field data May, $z_0 = 0.050cm$, cell 1 and 2 X

60 Model results and field data May, $z_0 = 0.050cm$, cell 3 and 4 XI
61 Velocity plots in the horizontal plane, February XIV
62 Velocity plots in the horizontal plane, May XV
63 Velocity plots in the horizontal plane, different tidal ranges XVI
64 Field data from King et al. (1985) XVII
65 Comparison of tidal ellipses from simulation and field data XIX
65 (continued) XX
66 Definition of the tidal ellipse orientation XXI
67 Effect of bottom roughness on tidal ellipses XXII
68 Orientation of the tidal ellipses for different bottom roughnesses XXIII
69 Effect of depth on tidal ellipses XXV
70 Orientation of the tidal ellipses for different depths h XXVI
71 Boundary layer thickness as a function of depth XXVI

List of Tables

3 Properties of the vertical velocities in the field data 62
4 Residual current of field data 62
5 Friction velocities, Reynolds roughness numbers and flow regimes 79

Abbreviations

CO-OPS	The U.S. Government's Center for Operational Oceanographic Products and Services
DNS	Direct numerical simulation
LES	Large-eddy simulation
ME	Magnetic east
MERIKA	Marine Energy Research Innovation and Knowledge Accelerator
MN	Magnetic north
RANS	Reynolds averaged Navier Stokes
TE	True east
TN	True north
UHI	University of the Highlands and Islands

Symbols

General comments: All symbols are defined both in the below list and in the text. In the text, the symbols are defined the first time they occur. A symbol might be given several meanings.

a, b, c	Dimensionless coefficients
A, B	Dimensionless coefficients
$\boldsymbol{a}_E$	Translatory acceleration of the earth's center of mass
$\boldsymbol{a}_{P,abs}$	Absolute acceleration of a fixed point P on the earth
$\boldsymbol{a}_T$	Acceleration of the axis T
c_p	Phase velocity of waves
c_1	Dimensionless coefficient
$c_{\epsilon 1}$	Dimensionless coefficient
$c_{\epsilon 2}$	Dimensionless coefficient
C_D	Dimensionless coefficient
C_μ	Dimensionless coefficient
D_k	Diffusion of turbulent kinetic energy
f	Coriolis parameter
f	Frequency
f_c	Cut-off frequency
F	Force
F	The ratio of the sum of the amplitudes of the main diurnal components (K_1 and O_1) to the sum of the amplitudes of the main semidiurnal components (M_2 and S_2)
g	Standard acceleration of free fall on Earth
$\boldsymbol{G}$	Gravitational attraction
h	Water depth
$i = \sqrt{-1}$	Imaginary unit
l^*	Length scale
l_m	Length scale (in the mixing length model)
L	Characteristic length

L_2	Smaller lunar elliptic semidiurnal tidal constituent
k	Turbulent kinetic energy
k	Wave number
$\boldsymbol{k}$	Local vertical unit vector
$\overline{k}$	Mean turbulent kinetic energy
k_s	Nikuradse equivalent sand grain roughness
K	Coefficient of internal friction
K_1	Luni-solar declination diurnal tidal constituent
m	Mass
M	Mass (of the moon)
M	Mass flux
$\overline{M}$	Time averaged mass flux
M_2	Principal lunar semidiurnal tidal constituent
M_6	Shallow water overtides of principal lunar tidal constituent
M_8	Shallow water eight diurnal tidal constituent
n	Number of data points
N_2	Larger lunar elliptic semidiurnal tidal constituent
O_1	Principal lunar declination diurnal tidal constituent
p	Pressure
$\overline{p}$	Time averaged pressure
p'	Fluctuating component of pressure
P	A point on the surface of the earth
P_1	Principal solar declination diurnal tidal constituent
P_k	Production of turbulent kinetic energy
$\boldsymbol{r}$	Position vector of a point P in the earth-fixed relative coordinate system
$\boldsymbol{r}_E$	position vector of the earth's center of mass taken from the center of mass of the earth-moon system
Re	Reynolds number
Rr	Reynolds roughness number
$\boldsymbol{S}$	Total current integrated over the water column

S_2	Principal solar semidiurnal tidal constituent
S_6	Shallow water overtides of principal solar tidal constituent
SE	Squared error
$\overline{S_{ij}}$	Mean rate of strain
t	Time
T	An imagined axis through the combined center of mass of the earth and the moon, about which the earth-moon system rotates
T	Wave period
u, v, w	Velocities in x, y and z direction, respectively
u_i	Velocities in x, y and z direction for i=(1,2,3), respectively
$\overline{u}$	Time averaged velocity component
u_L	Lagrangian mass transport velocity
(u_g, v_g)	Geostrophic velocity components
u'	Fluctuating velocity component
u_*	Friction velocity
U	Return current
$U = \sqrt{u^2 + v^2}$	Current speed (or mean current speed, in which case it is specified clearly in the text)
U_d	Defect velocity
U_g	Geostrophic velocity
$\overline{U}$	Depth-averaged mean current speed
U_0	x-direction component of interior flow
V^*	Velocity scale
V_m	Velocity scale of the largest eddies in the flow
V_0	y-direction component of interior flow
w_a	Vertical velocity if the vertical velocity is greater than the horizontal
x_i	Coordinate system. $x_i(i = 1,2,3) = (x, y, z)$
x, y, z	Coordinate system. x towards East, y towards North, z upwards
(x_1, z_1)	Mean position of water particles
z_0	Bottom roughness height

z_a	Apparent bottom roughness height in the presence of waves
γ	Universal gravitational constant
δ	Boundary layer thickness
δ_{ij}	Kronecker delta function
ϵ	Rate of dissipation of turbulent kinetic energy
ζ_a	Wave amplitude
(ζ, ϵ)	Local coordinate system in (x, y) directions, respectively
η	Relative vorticity
η	Surface elevation
θ	Latitude
κ	The von Karman constant
λ	Wavelength
ν	Kinematic viscosity
ν_T	Eddy viscosity
ω	Angular frequency (of waves or of the earth)
$\boldsymbol{\omega}$	Angular velocity (of the earth)
$\boldsymbol{\omega_z}$	Local vertical component of $\boldsymbol{\omega}$
$\dot{\boldsymbol{\omega}}$	Angular acceleration (of the earth)
$\boldsymbol{\Omega}$	Angular velocity (of the earth-moon system)
ρ	Fluid density
σ_k	Dimensionless coefficient
σ_ϵ	Dimensionless coefficient
$\boldsymbol{\tau} = (\tau_x, \tau_y)$	Shear stress
τ_0	Bottom shear stress
ϕ_{Ra}	Orientation angle of tidal ellipse

1 Introduction

Gravity forces from the moon and the sun, together with the relative motions of the earth, the moon and the sun, generate tides in the oceans. The most obvious effect of the tides is the vertical oscillation of the ocean surface. As the tides rise and fall, immense amounts of water are transported along with them. This transportation of water gives rise to tidal currents. These currents can be quite strong, especially over shallow grounds and in narrow inlets. Tidal currents are important for transport of e.g. plankton, larvae, contaminated ballast water, oil spills and sea bottom material. They may also be of interest in design and operation of offshore structures. Tidal flows are typically turbulent, and must therefore be modeled carefully. In coastal zones, the interaction of the tidal currents with other phenomena is stronger than anywhere else in the ocean. Due to shallow-water conditions, bottom friction may influence the flow all the way up to the surface. Irregular bottom topography and constrictions imposed by coastlines complicate the flow.

Many different models have been applied in studies of tidal flows. Three-dimensional models have extensively been applied to grids representing specific ocean areas (see e.g. Niwa and Hibiya (2004) and Cai et al. (2006)). Sakamoto and Akitomo (2008) investigated tidal boundary layers (not for a specific area), using three-dimensional direct numerical simulation (DNS). Salon and Armenio (2011) investigated turbulent oscillating and rotating boundary layers, such as those of tidal flow, using large-eddy simulations (LES). Such simulations require large amounts of computational power. In addition, it is challenging to include the effects of high Reynolds number and rough bottom when using DNS or LES (Holmedal and Myrhaug, 2013). Therefore, simpler models may often be advantageous. One-dimensional numerical models, where the grid points are located along a line from the bottom to the surface, have been successfully used to study different properties of tidal flow. Holmedal and Myrhaug (2013) investigated combined tidal and wind driven flows using such a model. The model used by Holmedal and Myrhaug (2013) is the same as the one used in this work.

The choice of turbulence model is essential. In early works, the assumptions of a constant eddy viscosity (see e.g. Prandle, 1982) or a time-invariant eddy viscosity increasing linearly with the distance from the bottom (see e.g. Grant and Madsen, 1979) were often used. In

modern works, two-equation turbulence closures are commonly used in one-dimensional models. These turbulence models include the Mellor-Yamada model (Mellor and Yamada, 1982), the $k-\omega$ model (Wilcox, 1988) and the $k-\epsilon$ model (Rodi, 1987), amongst several others. In the model used in the present work, a $k-\epsilon$ turbulence closure is applied.

A large number of scientific articles have been published on the topic of tidal boundary layers, many of which have applied one-dimensional two-equation turbulence closure models. Some of these have studied shallow-water tidal flows specifically. Jones and Monismith (2008) studied the ability of such models to reproduce the rate of dissipation of turbulent kinetic energy ϵ and mean velocity profiles for a shallow-water flow forced by tides and wind. They assessed three turbulence models: the $k-\omega$ model and two models based on the Mellor-Yamada model. Due to the complex nature of near-shore shallow-water geophysical flows, and the vast amount of possible bottom conditions, it is still appropriate to assess the applicability of such models under different conditions. The main objective of the present work is to investigate the applicability of a one-dimensional model with a $k-\epsilon$ turbulence scheme on a shallow-water tidal flow over a complex bottom. The bottom consists partly of boulders and tall seaweed.

The structure of the thesis is as follows. In chapters 2 - 4, relevant background theory is presented. Chapter 2 gives an introduction to tides and tidal theory, spanning from simple early models to complex interaction effects. This chapter is important, because an understanding of the nature of the tides is crucial in more detailed tidal flow studies, like the present. In chapter 3, theory on atmosphere-ocean interaction is presented. The focus is on interaction effects that are likely to influence tidal flows. Turbulence theory and turbulence modeling is presented in chapter 4. These topics are of fundamental interest, as turbulence modeling is a challenging task, with great influence on the results. In chapter 5, the model is presented. The field data used as input for the forcing of the model and for comparison with model results are presented and discussed in chapter 6. The results of the modeling are presented and discussed in chapter 7. The conclusions are given in chapter 8, and recommendations for further work in chapter 9.

2 Tides

The tides are oscillating flows in the oceans caused by centrifugal forces and gravity from astronomical bodies. They cause the ocean surface to rise and fall in an oscillatory pattern. The tidal forcing from an astronomical body depends on the combination of the mass of the body and its distance from Earth. The main contributors to the tides on Earth are the moon and the sun. The tidal forcing from the moon is about twice the forcing from the sun. The forcing from other astronomical bodies is negligible in comparison. Tides are completely deterministic. However, due to complex interactions between different effects, they might be hard to model without field data, especially in coastal zones.

2.1 Equilibrium model

2.1.1 Lunar tides

From Newton's law of universal gravitation, we know that gravity forces decay with the squared distance between the involved masses. The tidal forcing from an astronomical object depends on the difference in the gravity force on an object on the side of the earth closest to the body, and the gravity force on the same object on the far side of the earth. A simplified understanding of tides can be obtained by studying the equilibrium model developed by Isaac Newton in the seventeenth century. The interpretation of the equilibrium model described here is mainly taken from Myrhaug (2012) and Brown et al. (1989), with Pinet (2006) as supplementary background. In this model, we consider an idealized earth consisting of water only (there are no landmasses, not even submerged), and a moon. The earth-moon system is considered to rotate about an axis T through its combined center of mass (see figure 1). In the case of the earth we live on and our moon, this axis penetrates Earth. The rotation of the system is what we normally think of as the moon's rotation about Earth. At this stage, we do not consider the rotation of the earth about its own axis. The rotary motion of the system results in a centrifugal force directed away from the moon. We should note that the centrifugal force is not a real, physical force, but an apparent force resulting from the effect of centripetal acceleration when observation is done from the earth. We assume the distance between the earth and the moon to be constant, i.e. the earth and the moon

move in circles, not in ellipses.

The absolute acceleration of a fixed point P on the surface of the earth can be written

$$\boldsymbol{a}_{P,abs} = \boldsymbol{a}_E + \dot{\boldsymbol{\omega}} \times \boldsymbol{r} + \boldsymbol{\omega} \times \boldsymbol{\omega} \times \boldsymbol{r}, \tag{2.1}$$

where $\boldsymbol{a}_E$ is the translatory acceleration of the earth's center of mass, $\boldsymbol{\omega}$ is the angular velocity of the earth, $\dot{\boldsymbol{\omega}}$ is the angular acceleration of the earth and $\boldsymbol{r}$ is the position vector of P in the earth-fixed relative coordinate system, as shown in figure 1. The last term in equation (2.1) is directed normal to the earth's axis and has the same magnitude for all points on the earth (if we assume the earth to be a perfect sphere). Hence, it does not contribute to the tidal forcing. The term $\dot{\boldsymbol{\omega}} \times \boldsymbol{r}$ is neglected because $\dot{\boldsymbol{\omega}}$ is very small. This gives

$$\boldsymbol{a}_{P,abs} = \boldsymbol{a}_E = \boldsymbol{a}_T + \boldsymbol{\Omega} \times \boldsymbol{\Omega} \times \boldsymbol{r}_E, \tag{2.2}$$

where $\boldsymbol{a}_T$ is the acceleration of the axis T, $\boldsymbol{\Omega}$ is the angular velocity of the earth-moon system and $\boldsymbol{r}_E$ is the position vector of the earth's center of mass taken from the center of mass of the combined system (see figure 1). $\boldsymbol{a}_T$ is small (the period of this motion is one year), and is therefore neglected. The resulting equation is

$$\boldsymbol{a}_{P,abs} = \boldsymbol{\Omega} \times \boldsymbol{\Omega} \times \boldsymbol{r}_E. \tag{2.3}$$

The right hand side of equation (2.3) is the centripetal acceleration due to the rotation of the earth-moon system. Inserted in Newton's second law, this gives

$$\frac{\sum \boldsymbol{F}}{m} = \boldsymbol{a}_{P,abs} = \boldsymbol{\Omega} \times \boldsymbol{\Omega} \times \boldsymbol{r}_E. \tag{2.4}$$

As mentioned, the effect of the centripetal acceleration will appear as a force to an observer standing on the earth. Because of this, we move the centripetal acceleration to the force side of the equation and call it the centrifugal force:

$$\frac{\sum \boldsymbol{F}}{m} - \boldsymbol{\Omega} \times \boldsymbol{\Omega} \times \boldsymbol{r}_E = 0. \tag{2.5}$$

The centrifugal force has the same magnitude and direction for all points on the earth. The direction is parallel to the line going from the center of the moon to the center of the earth, and always away from the moon. This might be hard to imagine, but to understand this we should keep in mind that the earth itself (at this stage of the model) does not rotate, but has

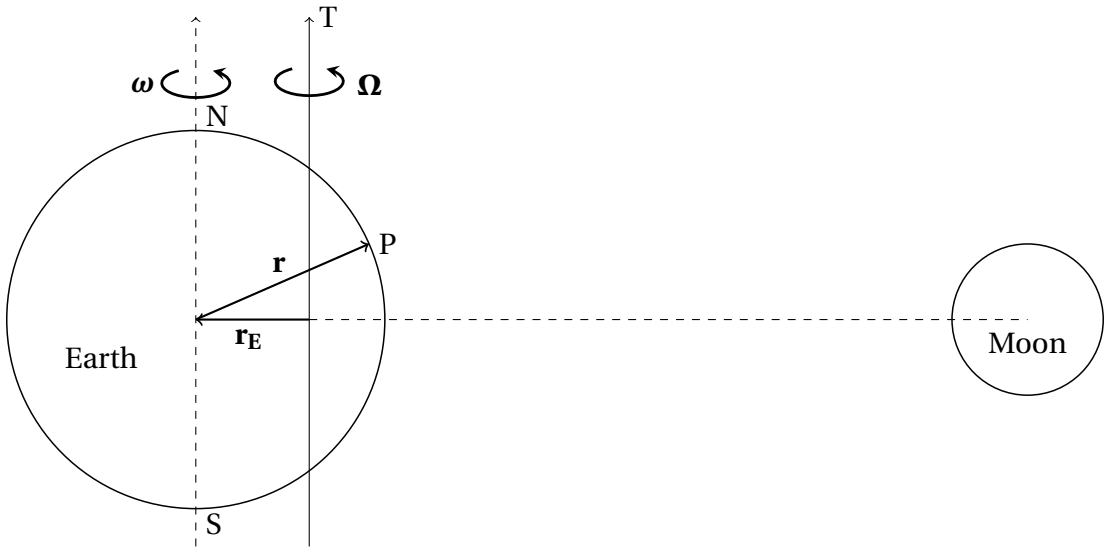

(a)

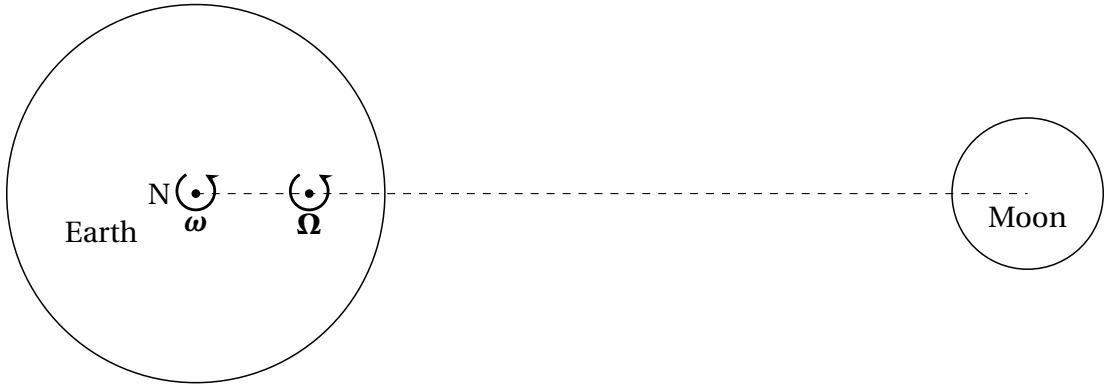

(b)

Figure 1: Definitions in the earth-moon system. In (a), the system is shown from a point on the plane of rotation (i.e. the moon will rotate into the paper). In (b), the system is shown from above, i.e. the moon will stay in the paper plane during rotation. N and S denote the north pole and the south pole, respectively. $\mathbf{r_E}$ *is a vector from the center of mass of the combined earth-moon system to the center of mass of the earth. The axis T, about which the earth-moon system rotates with angular velocity* $\boldsymbol{\Omega}$*, is shown. T goes through the combined center of mass. The earth's axis of rotation is also shown. The earth rotates about its own axis with angular velocity* $\boldsymbol{\omega}$*. In these figures, the lunar declination is zero.*

oscillatory circular motion. All points on the earth move in circles with the same radius r_E. We now consider the earth-moon system to be in equilibrium, in the sense that the earth and the moon do not move away from each other or towards each other. Hence, the total centrifugal force acting on the earth equals the gravitational attraction $\boldsymbol{G}$ between the earth and the moon:

$$\frac{\boldsymbol{G}}{m} - \boldsymbol{\Omega} \times \boldsymbol{\Omega} \times \boldsymbol{r}_E = 0. \tag{2.6}$$

However, if we consider a parcel of water located in point P on the earth, the two forces will not necessarily be in equilibrium (depending on the location of P). The gravitational attraction from the moon on a parcel of water with mass m is

$$F = \gamma \frac{mM}{r^2}, \tag{2.7}$$

directed towards the center of mass of the moon. γ is the universal gravitational constant and M is the mass of the moon. On the side of the earth closest to the moon, the gravitational attraction is larger than the centrifugal force. On the far side of the earth, the centrifugal force is dominating. The difference in the two forces gives rise to a resultant force, as shown in figure 2. This distribution of resultant force over the idealized earth creates two tidal bulges of water, as indicated in figure 3.

At this stage, we take into account the rotation of the earth about its own axis. So far, we have considered an idealized earth only consisting of water, which is distorted due to tidal forces. Now, we place a solid sphere inside the water, representing the real earth (see figure 3). The tidal bulges remains in line with the moon, while the earth spins beneath the bulges, with a period of one day. As a point on the earth passes through the tidal bulges, the tide rises and falls. Since the earth-moon system rotates as well, the rotation period of the earth seen from the moon is 24 hours and 50 minutes. This is called a lunar day. Since the tidal bulges move with the moon, this is also the period of the tides. Due to the declination of the moon (i.e. the angle of the moon relative to the normal of the earth's axis of rotation), which varies between 28.5° north and south with a period of 27.2 days, the tidal pattern varies from lunar day to lunar day (see figure 4). Another effect of lunar declination is that when the declination is high, the high latitudes will only experience one high tide per lunar day (diurnal tides), while the low latitudes experience two high tides (semidiurnal tides), as indicated in figure 4.

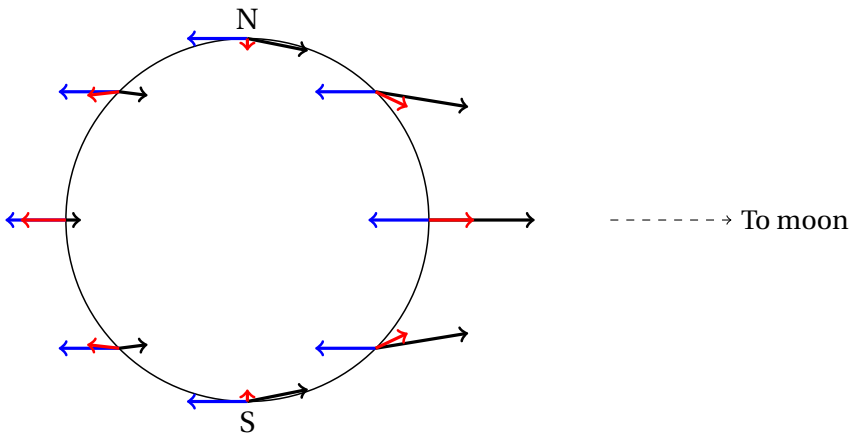

Figure 2: Gravity force (black) from the moon, centrifugal force (blue) and resultant force (red) for parcels of water at different locations on the earth's surface. In the equilibrium model, the distribution of resultant forces deform the simplified earth to an elliptic shape. The relative magnitudes of the forces are not to scale. The same applies for the size of the earth relative to the distance to the moon indicated by the arrows.

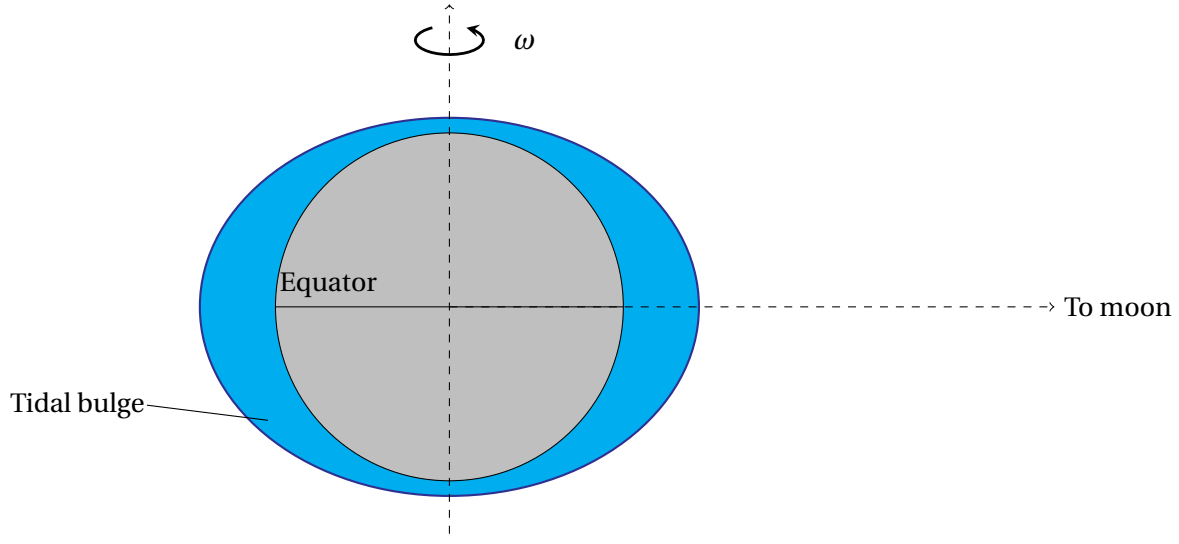

Figure 3: Tidal bulges in the equilibrium model. As the earth spins beneath the tidal bulges, points on the earth's surface experience an oscillating water depth, except at the poles.

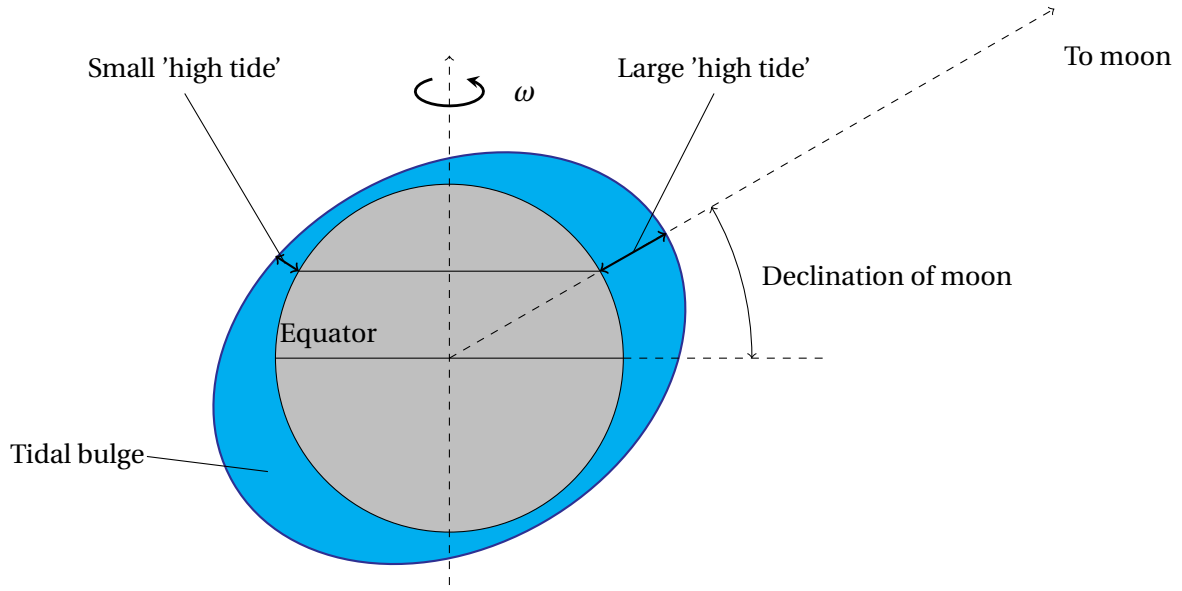

Figure 4: Effect of lunar declination in the equilibrium model. For high declinations, a point on a given latitude will experience both a small and a large 'high tide' during a lunar day. Here, the latitude of the considered point is the same as the moon's declination. (Reproduced after Brown et al., 1989).

2.1.2 Combined lunar and solar tides

The oceans on Earth are influenced by tidal forces due to both the moon and the sun. The tidal forcing from the sun works in the same way as described for the moon. Since the period of which the earth-moon system orbits the sun is different from the period of the rotation of the earth-moon system, these forces interact in an oscillatory way. For simplicity, we neglect the effects of declination of the moon and the sun. When the moon, the sun and the earth are aligned (i.e. at new moon and at full moon), the tidal forcing from the moon and from the sun works in the same direction. This results in a high tidal range (a large difference in height between high and low tide), known as *spring tide*. When the moon, the earth and the sun form a 90-degree angle, the lunar and solar tidal bulges have destructive interference. This results in a small tidal range, known as *neap tide*. This mechanism is illustrated in figure 5. The time interval between two succeeding full moons, and hence also the period of two spring tides and two neap tides, is 29.5 days.

There are several other astronomical effects complicating the tidal cycles. The effects of the declination of the moon and the sun results in maxima approximately every 14th day

and every half year, respectively (Myrhaug, 2012). The maxima occur when the moon or the sun crosses the equatorial plane. Further, the paths of the moon around the earth and of the earth around the sun are not circles, but ellipses. When the distance between the moon and the earth is at its smallest, we say that the moon is in *perigee*, and the tidal forcing from the moon has a maximum. It has a minimum when the moon is in *apogee*, i.e. when the distance is at its largest. The varying distance between the earth and the sun gives a similar effect on the tidal forcing from the sun, with maxima when the earth is at *perihelion* (minimum distance) and minima when it is at *aphelion* (maximum distance).

The equilibrium model gives us a basic understanding of how tides are generated. However, the tidal patterns we observe are very different from the ones predicted by this model. This is because we have neglected the effect of continents restraining the movement of water. If we use the equilibrium model as a basis, we can say that the effect of the presence of continents is that the tidal bulges are dragged away from where they would be in the equilibrium model. In addition, the bottom topography of the oceans affect the tides. An improved model corresponding better with the actual situation on Earth is the model known as the *dynamic model*.

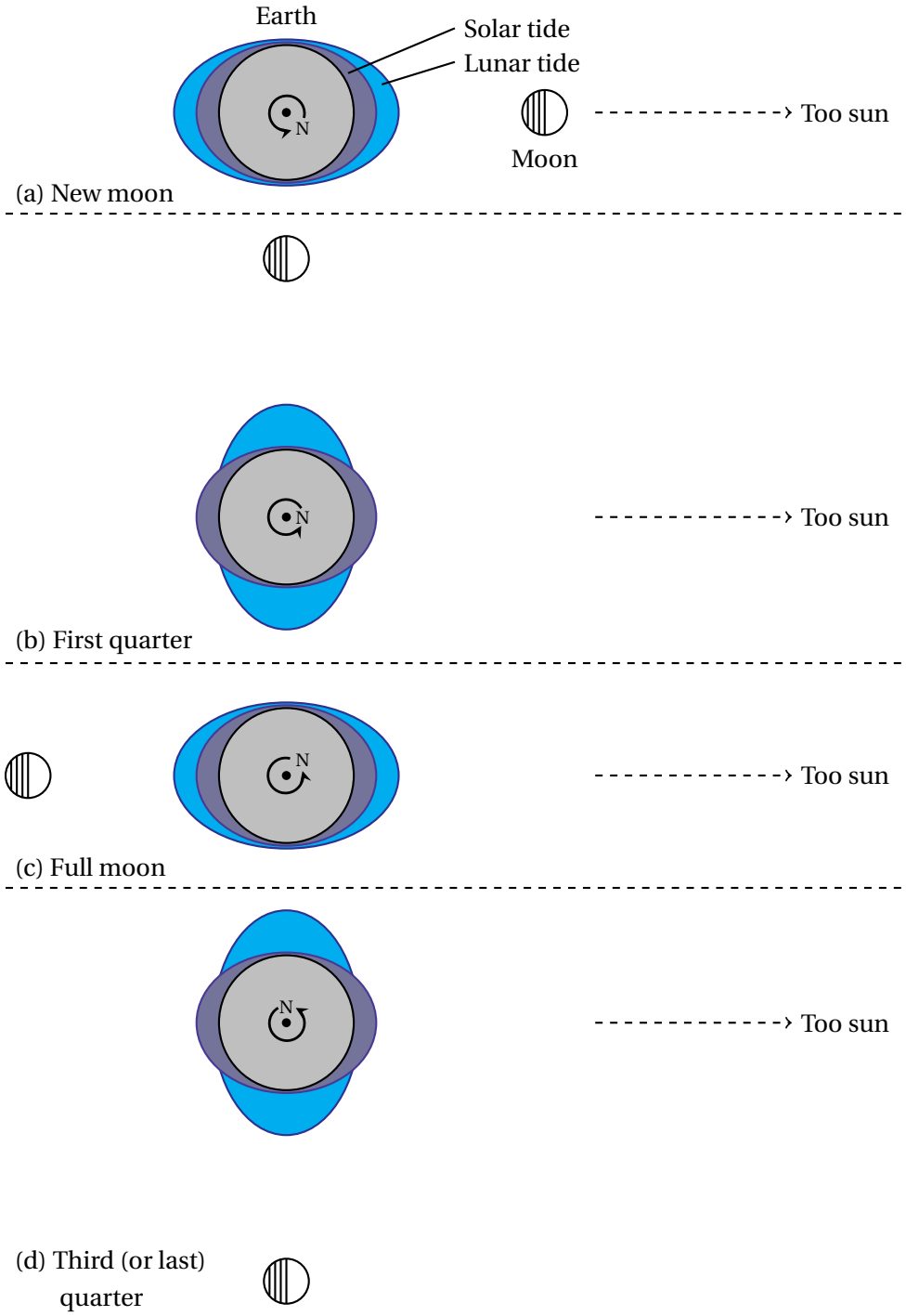

Figure 5: Interaction of lunar and solar tides in the equilibrium model. The situations causing spring tides are shown in (a) and (c), where the moon is in syzygy with the earth and the sun. This results in constructive interference of the solar and the lunar components. Situations (b) and (d) give neap tide due to destructive interference of the two components. Reproduced after Brown et al. (1989).

2.2 Dynamic model

The dynamic model was developed in the eighteenth century by Bernoulli, Euler, Laplace and others (Brown et al., 1989). They tried to take the effects of topography and continents into account. They also considered the Coriolis force, inertial forces and frictional forces. As noted by Brown et al. (1989), the dynamic theory is intricate with complex solutions. Here, a simplified version will be shown.

We consider a hypothetical earth with one ocean. The ocean has the same depth over its whole area, and is placed on the northern hemisphere, see figure 6. We only consider the tidal effect of the moon. Alternatively, we could say that we consider the situation when the sun and the moon are in syzygy (i.e. when they are aligned with the earth), the moon is between the sun and the earth, and they have the same declination. In this situation, the tidal forcing from the sun and the moon coincides. We further consider the declination to be such that the moon (or the moon and the sun) passes directly above the ocean as the earth rotates.

In the first situation in figure 6, the ocean basin has just passed the moon. The gravitational forces from the moon causes the water to pile up against the western border. This results in a pressure gradient that eventually will force the water back towards the east, when the basin has moved further away from the moon. Due to the Coriolis effect (the effect of the rotation of the earth about its own axis), the water will be deflected to the right when it flows back. This means that the water will now pile up against the southern border, as illustrated in the second situation in figure 6. This rotating flow continues around the basin, as illustrated. The flow will ultimately form a rotary wave and what we call an amphidromic system. The tidal wave rotates around what is called an amphidromic point, where the tidal range is zero. Lines connecting points where the tidal crest occur at the same time (i.e. at the same phase in the amphidromic system), are called *cotidal lines*. Lines connecting points with the same tidal range are called *corange lines*. In our idealized ocean basin, the cotidal lines are nearly straight and the corange lines are nearly parallel with the coastlines. However, due to bottom topography, the lines will be more or less irregular in the real oceans, as we can see in figure 7, where the amphidromic system in the North Sea is depicted. This is because the tidal waves act like shallow-water waves even in the deep oceans, due to their extremely large

wavelengths. The speed of shallow-water waves is a function of the water depth, so that we get wave refraction, which means that the direction of the waves is changed due to changing water depth.

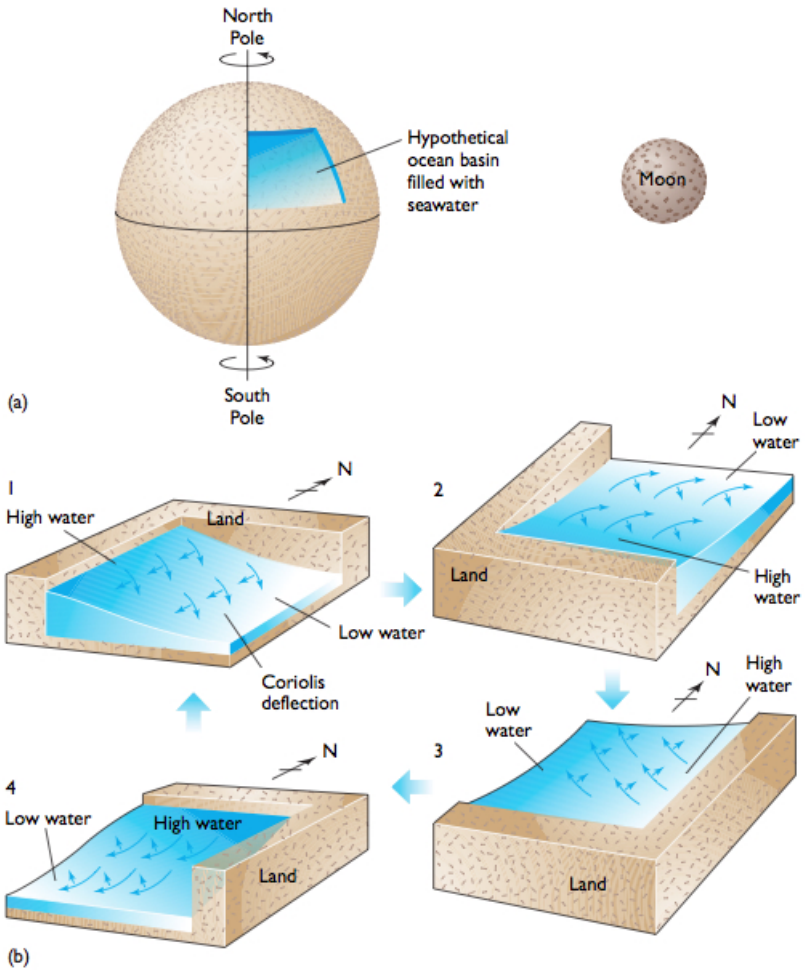

Figure 6: Idealized ocean basin of uniform depth. The tidal wave circulates the basin once during a tidal period, due to tidal forcing from the moon and the Coriolis effect. (Pinet, 2006).

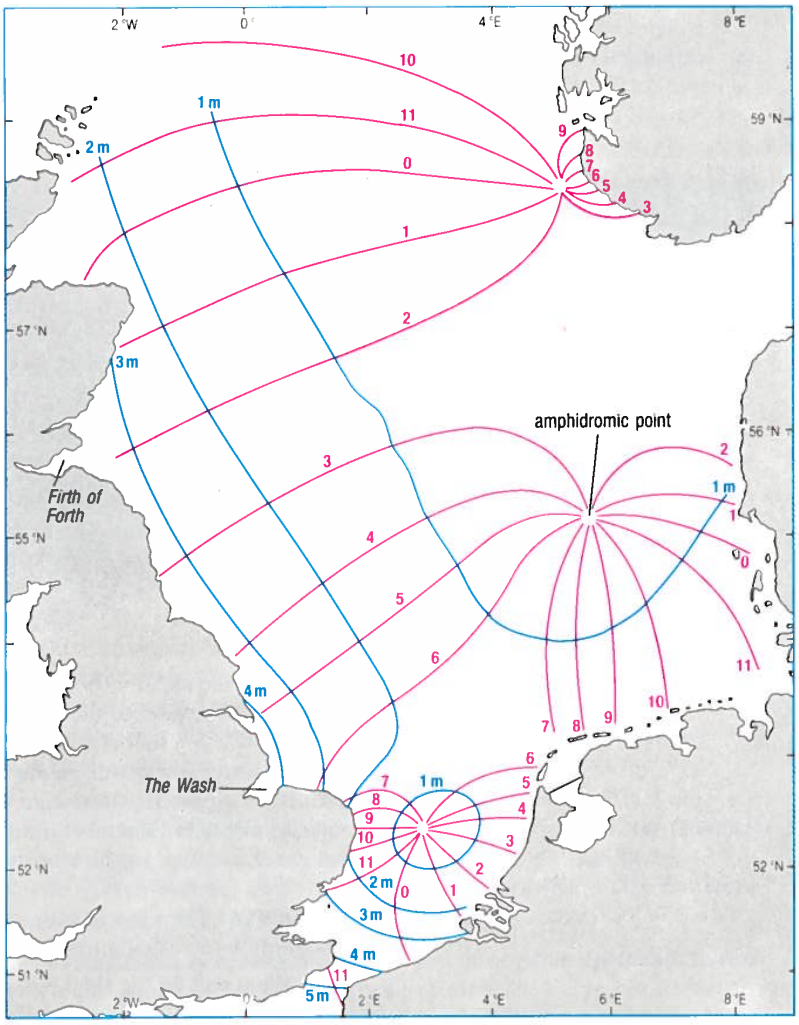

Figure 7: Amphidromic systems in the North Sea. The red lines are cotidal lines, and the blue are corange lines. The numbers on the cotidal lines indicate lunar hours (i.e. about 1 hour and 2 minutes). (Brown et al., 1989).

2.3 Tidal prediction, harmonic constituents and tidal patterns

As we have seen, the tides arise due to well-known and strictly periodic astronomical motions. However, due to effects such as irregular bottom topography and geometry of continents, there are large local variations in the tidal pattern. The simplest way of predicting tides is therefore to measure the water level (or the tidal currents) over some time, to identify how the different effects interact at the specific location. Each effect may be described by a simple sine function, which can be identified in the measured signal. By determining the harmonic constituents present in the signal, and their magnitudes, accurate tidal pre-

dictions for the future can be made.

The main tidal pattern caused by the moon, with two high tides per lunar day (semidiurnal tides), is represented by the constituent called *principal lunar semidiurnal*, denoted M_2. The period of this component is 12.42 hours, corresponding to one half of a lunar day. The *principal solar semiurnal* constituent, denoted S_2, has a period of 12.00 hours, one half of a solar day. The effect of the elliptic path of the moon around the earth is simulated by the constituents *larger lunar elliptic semidiurnal* (N_2) and *smaller lunar elliptic semidiurnal* (L_2). These are artificial constituents specifically designed to simulate the effect of the elliptic path. The effect of the moon's declination is simulated by the *luni-solar declination diurnal* (K_1) and *principal lunar declination diurnal* (O_1) constituents. Further, (K_1) together with the *principal solar declination diurnal* constituent (P_1) simulates the effect of the sun's declination.

Many more tidal constituents could be listed. According to Brown et al. (1989), 390 constituents have been identified. The U.S. Government's Center for Operational Oceanographic Products and Services (CO-OPS) uses 37 constituents for their tidal predictions at most locations, while some more complex locations require more than 100 constituents for the predictions to be accurate (Hicks, 2006).

The tidal pattern (i.e. semidiurnal, diurnal or mixed type) at a specific location may be determined directly from the amplitudes of the constituents. We find the dominating tidal period by considering the ratio of the sum of the amplitudes of the main diurnal components (K_1 and O_1) to the sum of the amplitudes of the main semidiurnal components (M_2 and S_2). This ratio is denoted F. For high values of F (Brown et al. (1989) suggests $F > 3.0$), we have diurnal tides. The main effect causing fluctuations in the tidal range in this case is the declination of the moon. For low values of F (Brown et al. (1989) suggests $F < 0.25$), we have semidiurnal tides. Fluctuations in the tidal range of semidiurnal tides mainly follow the interactions of lunar and solar tides described in chapter 2.1.2, giving the characteristic pattern of spring and neap tides. For values of F in the interval between diurnal and semidiurnal tides, we have *mixed tides*. The different tidal patterns are illustrated in figure 8.

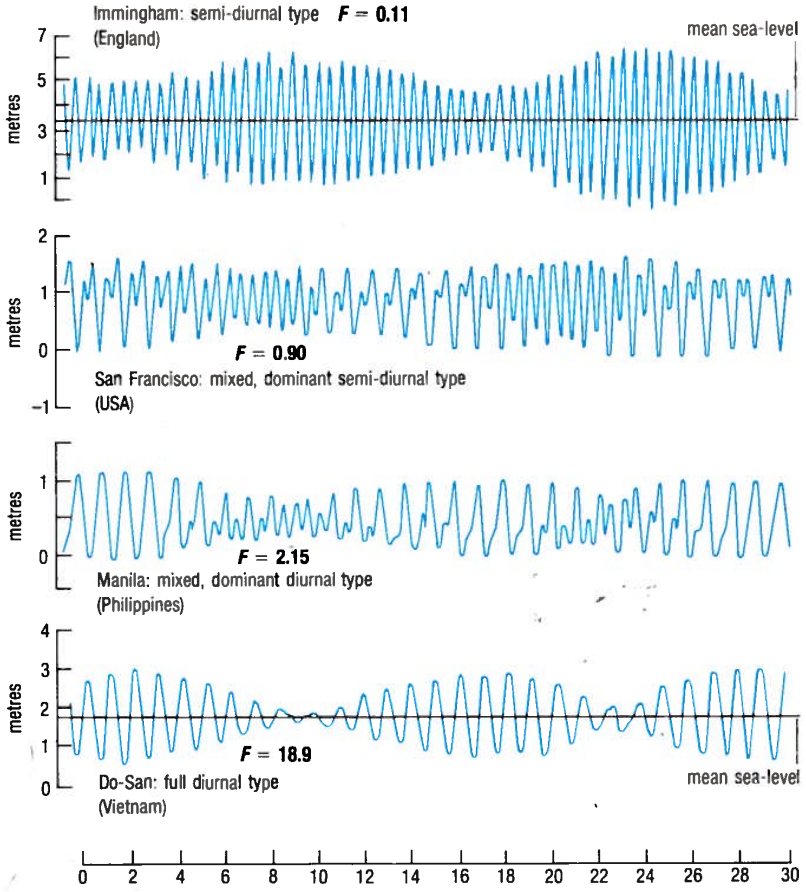

Figure 8: Time series of the surface elevation at different locations. The graphs from Immingham and Do-San illustrate semidiurnal and diurnal tides, respectively, while the tides at San Francisco and Manila are of the mixed type. The dependency of the ratio F is evident. (Brown et al., 1989).

2.4 Tidal currents

As described in chapter 2.2, the tidal motion in an amphidromic system form a rotary wave. It is hence appropriate to consider properties of waves to understand the motion of the water due to tides. In linear wave theory, the water particles under waves move in closed, orbital paths. In deep water, these paths form circles. The radius of the circular motion decays exponentially with increasing distance from the free surface down into the water. At a depth of about half of the wavelength, the radius goes to zero, so that the water below this depth is not influenced by the waves. In shallow water, i.e. for water depths less than half of the wavelength, we have wave-induced motion all the way to the bottom. In this case, the parti-

cle motion under the waves is elliptic. Close to the bottom, the vertical motion is very small, so that the motion is more or less a back-and-forth motion. In chapter 2.2, we noted that tidal waves are shallow-water waves even in the deep oceans. In fact, the wavelength is so much longer than the depth, that the tidal flow is predominantly horizontal. This motion of the water under tidal waves is known as *tidal currents*. The tidal currents oscillate with the same period as the tidal elevation of the surface.

In the open ocean, where the tidal currents are not restricted by landmasses, the currents rotate. This means that, if we plot the velocity vectors for a point in the ocean in the horizontal plane over a tidal period (this plot is called a *current rose*), the vectors will display a rotating nature, rotating 360 degrees during one tidal cycle. The current vectors of a tidal constituent plotted in the horizontal plane over its period forms an ellipse, as shown in figure 9. These kinds of plots are therefore referred to as *tidal ellipses*. In the open ocean, the current typically rotates *cum sole*, i.e. clockwise in the northern hemisphere and anticlockwise in the southern hemisphere, due to the Coriolis effect. In coastal waters, where frictional forces due to bottom topography and constraining landmasses influence the flow, the rotation may also be *contra solem*. The angle of the main axis of the ellipse relative to the x-axis is arbitrary and depends mainly on the restriction by shores and bottom topography. Along straight shorelines with nearly parallel bottom contours, the main axis is also more or less parallel to the shore.

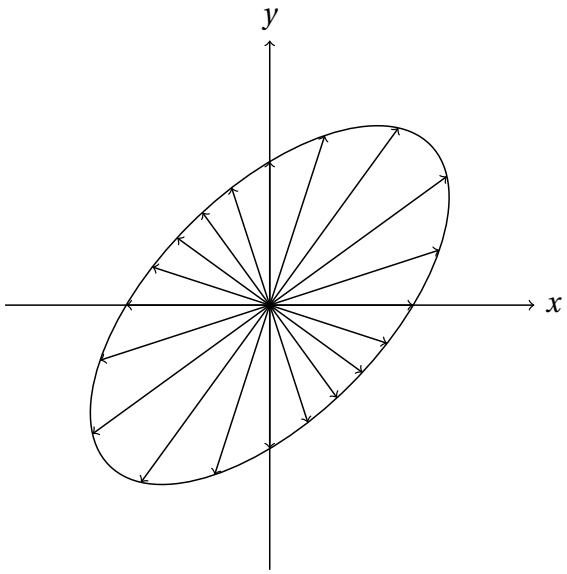

Figure 9: Sketch of a tidal ellipse. The velocity vectors of the tidal current (for one tidal constituent) plotted in the horizontal plane throughout the tidal period forms an ellipse. This type of current vector plot is called a current rose. Here, the current vector is plotted 20 times over a tidal period.

2.5 Shallow-water effects

In coastal areas, the tides are affected by the bathymetry (i.e. the underwater topography) and the geometry of the coasts to a much greater extent than in the open ocean. The interaction effects between tides and other phenomena are most significant in these areas. A review of such interaction effects is given in LeBlond (1991), which is the background for this section.

2.5.1 Direct effects of bathymetry and coastal geometry

Perhaps the most obvious effect of bathymetry and the geometry of the coast is the direct constriction of water flow. The presence of land, grounds and similar force the moving water masses in directions it would not take if flowing freely. The horizontal scales of the tidal flow is reduced due to both the direct constriction from straits and due to reduced water depth. The latter can be explained by referring to the Rossby radius of deformation, which for barotropic flows is defined as $\sqrt{gh}/f$, where g is the acceleration of free fall, h is the water depth and $f = 2\omega\sin(\theta)$ is the Coriolis parameter. ω is the angular velocity of the earth, and θ

is the latitude. The Rossby radius of deflection is an important length scale in oceanography, because it gives the scale at which rotational effects (such as the Coriolis effect) become as important as gravity effects. As the depth h decreases against the shore, the Rossby radius of deflection is reduced. According to LeBlond (1991) this means that, in coastal areas, the scale of the tidal flow is to a greater extent determined by continuity requirements than by dynamical balances. We have seen that the different tidal constituents have different periods. The wavelength λ and period T of finite-depth waves are linked through the relation

$$\lambda = \frac{g}{2\pi} T^2 \tanh(\frac{2\pi}{\lambda} h). \tag{2.8}$$

Hence, the constituents have different wavelengths, and are therefore influenced by spatial constrictions at different scales. This means that the type of tide, i.e. semidiurnal, mixed or diurnal type, may change over relatively small distances.

Tidal waves that travel along coasts have special characteristics, typically close to the characteristics of *Kelvin waves* or *shelf waves*. Noble et al. (1987) investigated the tidal currents along the northern California continental shelf. They found that the semidiurnal constituent M_2 propagated northwestward along the shelf as a Kelvinlike wave, primarily. The diurnal constituents travelled as a combination of Kelvin waves and continental shelf waves. Kelvin waves can only propagate with the coast on the right-hand side on the northern hemisphere and on the left-hand side on the southern hemisphere. They result from a balance between pressure forces due to surface inclination and the Coriolis effect (what Kraus and Businger (1994) refers to as a *quasi-geostrophic flow*). At the crest, the current flows in the wave propagation direction, so the Coriolis force acts towards the coast. However, the surface is inclined towards the coast, resulting in a pressure gradient forcing the water away from the coast. These forces should cancel each other. At the trough, the current is reversed, so that the Coriolis force is directed away from the coast and the pressure force due to the surface slope towards the coast, again canceling each other. A principal sketch of Kelvin waves is given in figure 10. Shelf waves are, unlike Kelvin waves, vorticity waves. Their propagation direction relative to the coast is similar to that of Kelvin waves. An essential ingredient in the understanding of shelf waves is the principle of potential vorticity conservation, which can be expressed as

$$\frac{\eta + f}{h} = constant \tag{2.9}$$

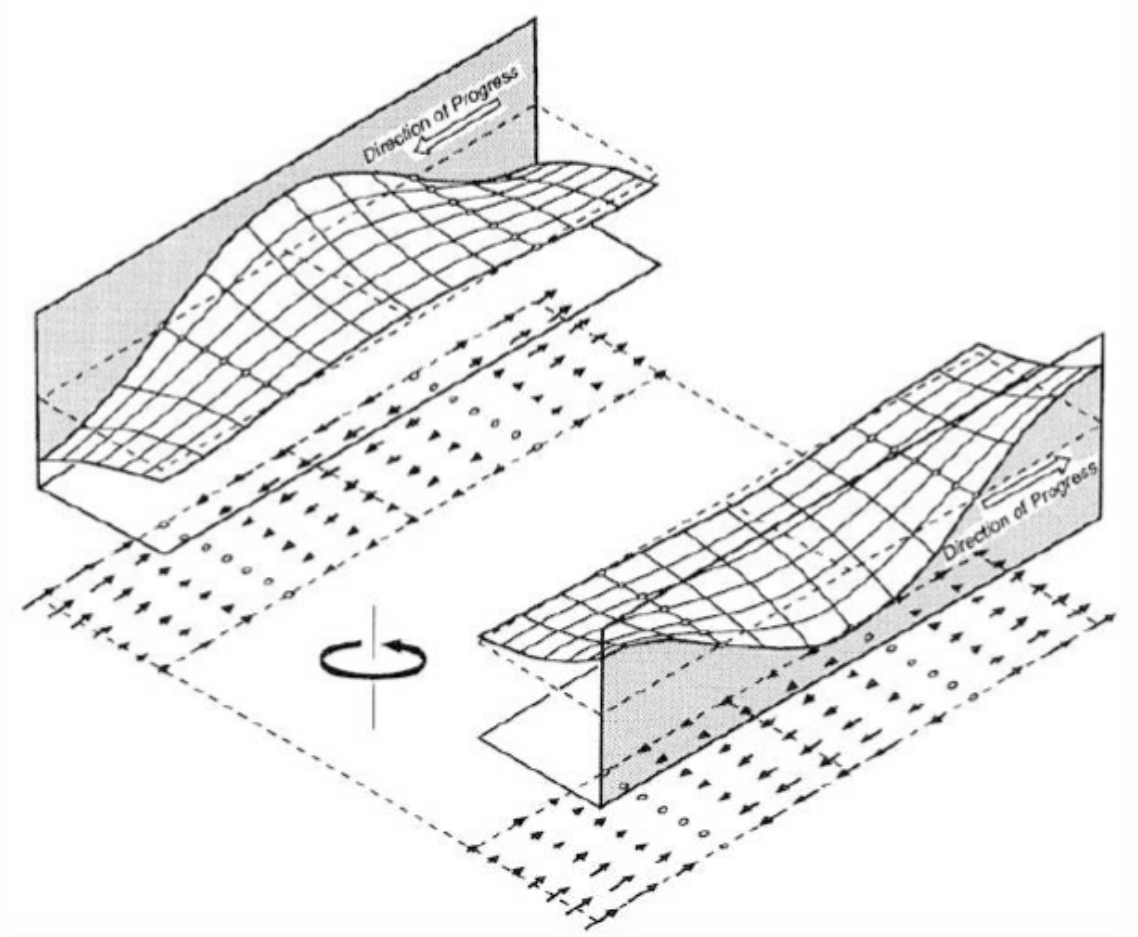

Figure 10: Principal sketch of Kelvin waves on the northern hemisphere. The arrows represent current velocities due to the waves. The Coriolis effect (due to the velocities) balances the pressure forces due to surface inclination. (Kraus and Businger, 1994).

for a water column, if it is not influenced by friction (Kraus and Businger, 1994). Here, η is the relative vorticity of the water column. We now consider an idealized coastline where the depth contours are parallel to the coast. A vertical sheet of water is initially also placed parallel to the coast, and the water has no relative vorticity. The sheet is displaced by a disturbance. According to equation (2.9), water columns displaced towards the coast, onto shallower water, will now experience a negative, i.e. anticyclonic, vorticity. Water columns displaced away from the coast will obtain cyclonic vorticity. As indicated in figure 11, the vorticity induces a current, which transports the sheet of water along the coast. Following water particles in the sheet as it is transported, we see that the described process will continue to transport the sheet along the coast.

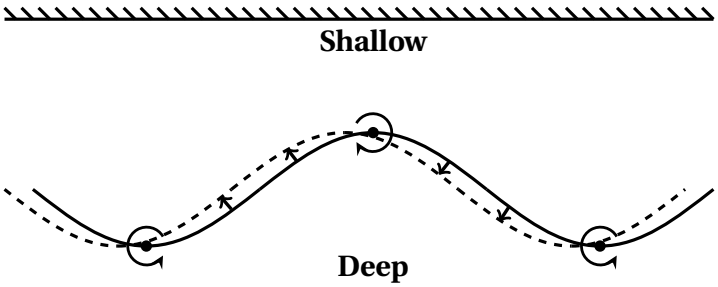

Figure 11: Principal sketch of a shelf wave. The depth contours are parallel to the coast. A vertical sheet of water, initially placed parallel to the coast and with no vorticity, is displaced by a disturbance. Its new form is represented by the solid line. According to the principle of potential vorticity conservation, the water will now experience vorticity as indicated by the circular arrows. The vorticity induces current, indicated by the straight arrows, transporting the sheet along the coast. Reproduced after Kraus and Businger (1994).

We can to some degree distinguish between Kelvin and shelf waves in field measurements by considering the tidal ellipses. For Kelvin waves they rotate cyclonic (counterclockwise on the northern hemisphere), and are parallel to the large-scale topography of the continental margin (Noble et al., 1987). The major axis of the ellipses under shelf waves may be either parallel or perpendicular to the topography. Determining the wave type of the tidal wave in the coastal area (note that it might well be a combination) is relevant because the magnitude of the current and wave propagation velocities, the decay scale towards the deep ocean and the wavelength of the two types are very different.

In some places, *tidal resonance* creates exceptionally high tidal ranges. The resonance period depends on frictional effects and topography, but the determination of it is heavily discussed (see e.g. LeBlond, 1991). In the Bay of Fundy, between Nova Scotia and New Brunswick, more than 146 km^3 of water flows into the bay during a period of 6.2 hours (one half of a semidiurnal period) at times of extreme tides, causing a tidal range exceeding 15 meters (Mossman, 2001). This is explained by a resonance period close to the period of the tidal forcing. Due to resonance periods in local coastal areas, tides may also excite *tidal ringing*, i.e. resonance at higher harmonics.

As the lateral scales of the flow is reduced, some areas will experience significant velocity gradients. This means that the importance of the inertial terms in the momentum equa-

tions will increase, and we may experience *inertial effects* such as generation of tidal residual currents, tidal jets and residual vorticity (LeBlond, 1991).

Another direct effect of the bathymetry in nearshore areas is the effect of friction. In shallow water, the bottom boundary layer covers the whole water depth, such that frictional effects are important in the dynamic balance.

2.5.2 Interaction with hydrodynamic phenomena

Since wind waves are present most of the time on the surface of all oceans, the possibility of them interacting with the tides should be considered. Tides certainly modify the waves in shallow-water areas, both through the variation of the mean water depth and through tidal currents. The phase velocity of surface waves is dependent on the depth, so that we get wave refraction in shallow water. Further, strong tidal currents will modify the waves. If the current is opposing the waves, they will steepen and might break. However, the effect of waves on tidal flow is less obvious. According to LeBlond (1991), wave steepening and breaking may only remove an insignificant part of the energy in the tidal flow, due to the considerable differences in scale. Hence, they will not influence the water level or the tidal currents except in extremely shallow water, in the surf zone. In the surf zone, the waves create a set-up (i.e. an increase of water depth) which is superposed with the expected water depth due to the tides. The waves also induce longshore currents in the surf zone, which might interact with the tidal flow. Longshore currents will be described in 3.1.3.

The phenomena of *storm surges* is caused by low atmospheric pressures e.g. below cyclonic storm systems. The surface is elevated due to the low pressure, and in coastal areas the elevation caused by storm surges may be several meters. Strong onshore winds related to the storm can contribute to the rise of the surface. Storm surges may cause great damage on both property and life, especially if coinciding with spring tides. Since the scales of tides and storm surges are comparable, we expect significant interaction between them. According to LeBlond (1991), these interactions could be simple superposition, but they may also be more complex. Therefore, modeling of storm surges should take the tides into account.

According to LeBlond (1991), interaction effects between the tides and the ocean currents (such as the Gulf Stream) are very small. The reason for this is that the ocean currents are very

slow relative to the propagation velocity of the tides at almost all locations in the ocean. Under such conditions, the ocean currents and the tidal currents are simply superposed. Note that the propagation velocity of the tide is the phase velocity of the tidal wave, i.e. the velocity of the wave crest, which is not the same as the velocity of the water particles. To get an impression of the phase velocities of tides, we consider the tides as propagating waves using linear wave theory. As explained in section 2.4, the tidal waves are shallow-water waves. In water of finite depth, the dispersion relationship for linear waves is $\omega^2 = kg\tanh(kh)$, where $\omega = 2\pi/T$ is the angular frequency of the waves and $k = 2\pi/\lambda$ is the wave number. The phase velocity is then given as $c_p = \lambda/T = \omega/k = \sqrt{(g/k)\tanh(kh)}$. For waves in very shallow water, or more correctly for $h/\lambda \to 0$, this simplifies to $c_p = \sqrt{gh}$. This means that, for a tidal wave in the North Sea, where the depth is less than 100 m almost everywhere, the phase speed is at least constricted to about 30 m/s. From the amphidromic systems depicted in figure 7, a typical maximum distance traveled by a tidal crest in the North Sea during a M_2 period can be estimated to about 1000 km. With the M_2 period of 12.42 h, this gives a phase velocity of $c_p = 22.4$ m/s. This velocity is obviously much larger than characteristic velocities of the ocean currents. We should note, however, that the phase velocity is reduced towards the amphidromic point.

A phenomenon which we may expect to interact with the tides is what is known as *internal tides*. Internal tides are internal waves in the ocean generated by interaction between tides and the bathymetry, typically continental slopes. The term internal waves is used for waves between layers of different densities in a fluid (i.e. in a stratified fluid). Since density differences are important, internal tides is a baroclinic phenomenon. The mechanisms are the same as for surface waves, like the ones in the intersection between the atmosphere and the ocean, but because the internal density differences in the ocean is much smaller than that of air and water, the scales are very different. The velocities of internal tides is much smaller than those of wind waves, and closer to that of tides, so interaction effects are more probable.

3 Atmosphere-ocean interaction

Complex interactions take place in the interface between the atmosphere and the ocean. These interactions are not fully understood, even though they have been studied in detail for more than a decade. Wave measurements, which make up an important basis for studies of atmosphere-ocean interaction, have been made for an even longer period of time; Leonardo da Vinci recorded waves about half a millennium ago. As stated by Kraus and Businger (1994), almost all motion in the oceans, except for the tides, are direct or indirect results of atmospheric influences. The most relevant effects for the present work are wave-induced current, wind-induced current and wave-current interaction.

3.1 Wave-induced current

In linear wave theory, valid for small-amplitude waves, the water particles move in closed circles or ellipses. Experiments show, however, a small net velocity (and hence also mass transport) in the direction of wave propagation. This effect can be derived from linear theory, as a second-order effect in the sense of ζ_a^2 dependency, where ζ_a is the wave amplitude. The effect can be studied in either the Eulerian frame, where the mean flow is studied in a fixed point, or in the Lagrangian frame, following the water particles. In the surf zone, close to the shore, incident waves generate longshore currents. Further, varying wave conditions along the shore contribute to the generation of rip-current patterns. These wave-related currents can be relatively strong.

3.1.1 Eulerian mass transport

Following Svendsen (2006), we write the mass flux through a vertical sheet of unit width as

$$M(t) = \int_{-h}^{\eta} \rho u(x,z,t)\,dz. \tag{3.1}$$

Here, a coordinate system with origin at the mean water level is used. η is the surface elevation, $\eta = \zeta_a * cos(\omega t - kx)$, where ζ_a is the wave amplitude. Averaging the mass flux over a wave period yields

$$\overline{M} = \overline{\int_{-h}^{\eta} \rho u(x,z,t)\,dz} = \overline{\int_{-h}^{0} \rho u(x,z,t)\,dz} + \overline{\int_{0}^{\eta} \rho u(x,z,t)\,dz}, \tag{3.2}$$

where the integral covering $z \in [-h, 0]$ is zero, using the standard expression for the horizontal velocity under linear waves. The reason for splitting the integral is that the linear description of waves is only valid to the mean surface level. When taking the first integral to be zero, we neglect the fact that at the wave trough, there is no water between the mean water level and the actual surface. According to Svendsen (2006), the error we make is cancelled by an equal contribution from the second integral. As the linear solution is not applicable in the interval $z \in [0, \eta]$, we must use the Taylor expansion of $u(x, z, t)$ for the last integral. Neglecting terms of order $O(\zeta_a^3)$ and higher, the resulting expression for the mean mass flux is (see Svendsen, 2006)

$$\overline{M} = \frac{\rho g \zeta_a^2}{2c_p}, \tag{3.3}$$

As the deduction shows, the non-zero contribution to the mass flux comes from the area between the wave trough and the crest only. In a wave tank or in the questionable assumption of a two-dimensional flow under waves propagating towards a shore, the total mean mass flux must be zero, from continuity considerations. Hence, there must exist a mean flow in the opposite direction of the wave propagation, with velocity

$$U = -(g\zeta_a^2)/(2c_p h), \tag{3.4}$$

if we assume that this *return current* is homogeneously distributed over the water column.

3.1.2 Lagrangian mass transport

To describe the flow under waves in the Lagrangian frame, we need expressions for the particle trajectories. Dean and Dalrymple (1984) denotes the particle position as $(x, z) = (x_1 + \zeta, z_1 + \epsilon)$, where (x_1, z_1) is the mean position. Using linear wave theory, ζ and ϵ can be found as (see Dean and Dalrymple, 1984)

$$\zeta = -\zeta_a \frac{\cosh k(h + z_1)}{\sinh kh} \sin(kx_1 - \omega t) \tag{3.5}$$

$$\epsilon = \zeta_a \frac{\sinh k(h + z_1)}{\sinh kh} \cos(kx_1 - \omega t), \tag{3.6}$$

for cosine waves. Dean and Dalrymple (1984) further approximates the instantaneous velocity of a water particle as

$$u_L(x_1 + \zeta, z_1 + \epsilon) = u(x_1, z_1) + \frac{\partial u}{\partial x}\zeta + \frac{\partial u}{\partial z}\epsilon. \tag{3.7}$$

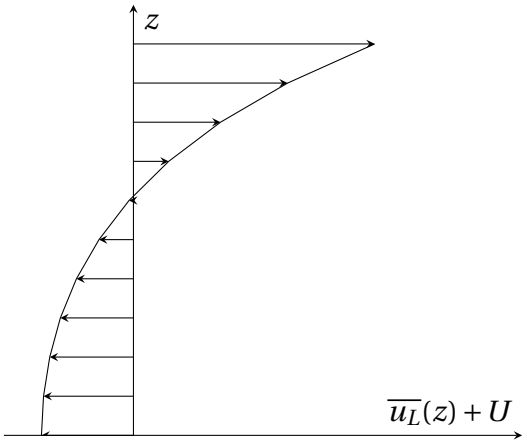

Figure 12: Distribution of the wave-induced Lagrangian current, including the return current U to satisfy conservation of mass. Note that the origin is at the seabed in the figure, although a local coordinate system with origin at the mean water level is used in the deduction of equation 3.8.

Inserting equations 3.5 and 3.6 into 3.7, and averaging over one wave period, gives

$$\overline{u_L}(z) = \frac{g\zeta_a^2 k^2 \cosh 2k(h+z)}{\omega \sinh 2kh}. \tag{3.8}$$

We notice that vertical integration of this velocity distribution yields the same mass transport over the water column as we found using the Eulerian frame. If we again argue that no total mean mass flux can exist due to continuity considerations, we find the same return current U as for the Eulerian frame. Hence, the difference between the velocity profiles predicted using the two frames is that, for the Eulerian frame, the current is homogeneous from the bottom to the wave trough, whereas for the Lagrangian frame, the velocity varies over the water column. It is largest and directed in the wave propagation direction at the mean surface, and decreasing towards the bottom, where it is directed against the propagation of the waves. Note that in this description of the Lagrangian velocity distribution, we have included the return current U, and again assumed it to be homogeneously distributed from the bed to the mean water level. A sketch of the distribution of the Lagrangian velocity over the water column is given in figure 12. In the figure, the origin is taken at the seabed to obtain consistency with the rest of the thesis, while equation 3.8 is valid for a local coordinate system with origin at the mean water level.

3.1.3 Longshore currents and rip currents

Waves travel without much energy loss, such that when they encounter the shore after building up at sea, energy must somehow be dissipated. Normally, most of the energy is dissipated through spilling breakers. The term spilling breakers denote the type of breaking waves where air is entrapped at the crest of a steep, close to symmetric wave, and forms a jet current down the front of the wave. This is the most common type of breaking wave, both in the deep sea and in shallow water near the shore (Myrhaug, 2006). To describe the near-shore currents induced by incident waves, we first need to describe the typical bottom topography near the shore. In the *inner shelf zone*, where the water depth is typically 10 to 30 meters (Dronkers, 2005), the bottom slope is very small. Shoreward of the inner shelf, we have the *shore face*, where the bottom becomes steeper. In the shore face, some distance from the beach, the waves start breaking. This position is denoted the *breaker line*, and varies with the wave conditions. From the breaker line to the shore, we have the *surf zone*, where the waves are smaller than outside the breaker line. The area at the beach that is alternating between being wet and dry due to the waves, is called the *swash zone*.

As explained by Dronkers (2005), the net momentum transferred from offshore to the surf zone is greater than what is transferred from the surf zone to the beach. This results in radiation stresses and subsequently pressure gradients. These cause the mean surface level in the area close to the beach to be higher than the offshore level (an effect called *wave setup*), and, for oblique incident waves, a longshore current. As we would expect, the magnitude of the current depends on the characteristics of the incident waves and on the bottom conditions. According to Dronkers (2005), it can exceed 1 m/s.

Another type of current system occurring in the near-shore area is *rip currents*. These are narrow jet currents typically on the order of 1 m/s, and possibly up to 2 m/s (MacMahan et al., 2006). Between the jets, there is a net mass transport in the onshore direction. The current magnitude in this area is much smaller than in the jet, because the distance between the jets is much greater than the typical width of the jets. Close to the shore, water is transferred from the area of shoreward mass transport to the rip currents, giving rise to longshore currents towards the jets. The generation of these circulation cells is not fully understood, although numerical models and improved techniques for field observations has contributed

to an increased understanding during the last years (see e.g. Yu and Chen, 2015). However, as stated by Yu and Chen (2015), it is generally accepted that a variation of the wave characteristics along the shore is necessary. Rip currents are often found in areas where the bottom conditions vary along the coast, e.g. with so-called rip channels. Due to wave shoaling and refraction, non-uniform topography along the shore may obviously contribute to non-uniform wave characteristics. It is not clear, however, if the rip channels are generated by the currents, or if they are important contributors to the generation of these. Non-stationary rip currents have been observed (see e.g. MacMahan et al., 2006), suggesting that non-uniform topography is not necessary for rip currents to form. Hence, there should exist a mechanism able to generate instability from an initially stable state of alongshore uniform conditions, also able to maintain the instability to generate rip-current patterns. Mechanisms that have been suggested are (Yu and Chen, 2015) variabilities due to sediment motions on the bottom and hydrodynamic instability due to wave-current interaction. The current systems of rip currents may exist together with, and interact with, the longshore currents described above. The structure of a rip-current is depicted in figure 13.

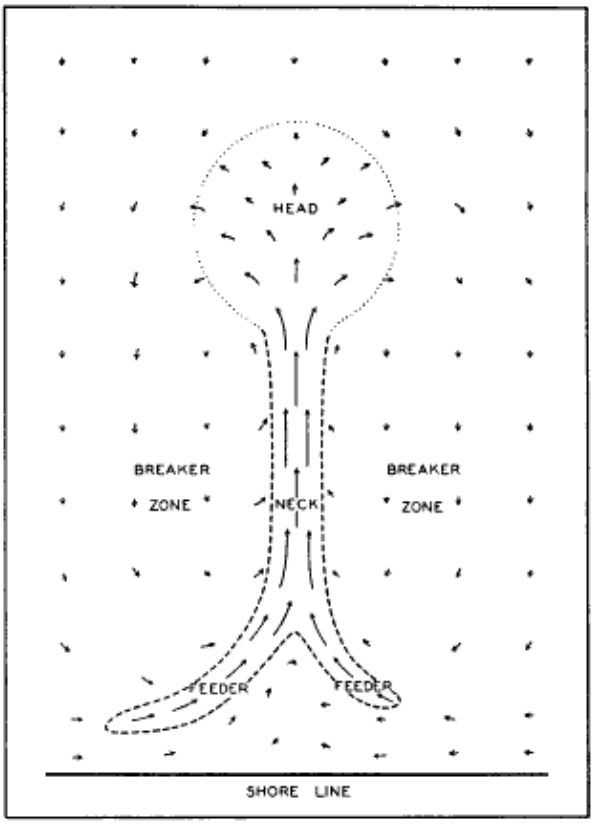

Figure 13: The structure of a rip current. (Shepard et al., 1941).

3.2 Wind-induced current

Wind blowing over the ocean surface will generate current in the upper part of the water column. The current results from shear stress on the surface due to the wind. Friction between succeeding layers of water will transfer the motion to deeper levels. Intuitively, one may think that the current will be in the direction of the near-surface wind. However, due to the rotation of the earth, the direction deviates through the water column. This phenomenon was studied after Fridtjof Nansen observed that ice drifted to the right of the wind direction on his expedition with «Fram» in the Arctic Ocean 1893-1896. In Nansen (1902), measurements of the drift of «Fram» (frozen in the ice) and of the wind is presented. Nansen (1902) writes that the results *"demonstrate clearly that for shorter periods the resultants of the drift deviate, with some few exceptions, towards the right of the corresponding wind-resultant, and generally the deviation is considerable. This deviation cannot be explained as being the effect of the current in the water, or of the resistance of land, for it occurs in whatever direction the*

wind blows". Nansen understood that the deviation was an effect of the Earth's rotation. He asked his colleague Vilhelm Bjerknes to let one of his students study the phenomenon. The task was given to Vagn Walfrid Ekman, who presented a solution for the wind-driven surface current in his doctoral thesis of 1902, today known as the classic Ekman layer solution.

3.2.1 The Ekman layer

Ekman's solution shows a deviation of the current direction to the right of the wind direction on the northern hemisphere, and to the left on the southern hemisphere. The current in the surface is directed 45° from the wind, and the angle increases towards the deeper sea. Simultaneously, the magnitude of the wind-induced current decreases. The total velocity integrated from the surface to the bottom (in absence of internal flow and with a water depth that exceeds the Ekman layer) is directed perpendicularly to the wind stress, to the right on the northern hemisphere. Hence, also the total mass transport is directed perpendicularly to the wind stress. This phenomenon is denoted *Ekman transport*, and is an important feature of the Ekman layer theory. For a homogeneous fluid with geostrophic internal current given by $(u, v) = (u_g, v_g)$, the surface Ekman layer is described by the following equations:

$$u = u_g + \frac{\sqrt{2}}{\rho f d} e^{\frac{z}{d}} \left\{ \tau_x \cos(\frac{z}{d} - \frac{\pi}{4}) - \tau_y \sin(\frac{z}{d} - \frac{\pi}{4}) \right\} \tag{3.9}$$

$$v = v_g + \frac{\sqrt{2}}{\rho f d} e^{\frac{z}{d}} \left\{ \tau_x \sin(\frac{z}{d} - \frac{\pi}{4}) - \tau_y \cos(\frac{z}{d} - \frac{\pi}{4}) \right\}, \tag{3.10}$$

where d is a distance defined by

$$d = \sqrt{\frac{2\nu}{f}}. \tag{3.11}$$

(u, v) are the velocity components in the (x, y) directions, respectively. ρ is the water density, ν is the kinematic viscosity and p is the dynamic pressure. (τ_x, τ_y) are the components of the shear stress vector $\boldsymbol{\tau}$ on the surface in the (x, y) directions. The deduction of these equations is shown in appendix D. As pointed out by Cushman-Roisin (1994), the thickness of the Ekman layer is on the order of d. Therefore, d is called the *Ekman depth*.

Ekman layers do not only exist in the ocean close to the surface. Corresponding boundary layers are found in the atmosphere close to the ground, and in the ocean close to the

seabed. These boundary layers are, similarly to the surface Ekman layer, formed by a combination of friction and the Coriolis effect (the effect of the earth being a rotating reference system). In the Ekman layers in the atmosphere and in the bottom of the ocean, the velocity deviates to the left of the internal flow towards the bottom, on the northern hemisphere. In Ekman's solution, the flow very close to the seabed is directed 45° to the left of the internal flow (Cushman-Roisin, 1994).

3.2.2 The relation between theoretical and observed Ekman layers

The kinematic viscosity ν of water is about $10^{-6}\,\mathrm{m^2 s^{-1}}$. If we plot the surface Ekman layer given by the equations (3.9) and (3.10) with this viscosity, we get a surface velocity that is very large compared with empirical data. In addition, we get an Ekman layer much thinner than in real flows. This is because the model does not account for turbulence. The wind stress on the surface is not only transferred through the boundary layer by molecular diffusion. In fact, what dominates the process is turbulent mixing. To get an impression of the importance of turbulence, we can replace the molecular kinematic viscosity with a constant eddy viscosity. Steele et al. (2001) states that *"scaling arguments suggests that [the magnitude of the constant eddy viscosity] may be as large as* $10^{-1}\,\mathrm{m^2 s^{-1}}$ *"*.

In figure 14, the Ekman layer with the proposed constant eddy viscosity of $10^{-1}\,\mathrm{m^2 s^{-1}}$ is shown. The water density is taken as $\rho = 1025\,\mathrm{kg/m^3}$, the latitude is 30° north, and the wind stress is taken as $0,1\,\mathrm{N/m^2}$, corresponding to a wind speed of about 10 m/s in a height of 10 m above the surface. The wind direction is towards the north.

Although the assumption of a constant eddy viscosity greater than the molecular viscosity gives a better representation of the surface layer than if we use the molecular viscosity, it is a very simple turbulence model and not a good representation of the real flow. Cushman-Roisin (1994) states that the eddy viscosity should at least vary in the vertical (first shown by Madsen, 1977). Ekman was, naturally, aware that the theoretical values obtained for the surface layer with his model did not represent real flows well. In Nansen (1902), some values of the thickness of the Ekman layer is calculated with standard values of the relevant parameters. Nansen writes *"these theoretical values of the depth of the stationary wind-current are of course absurd. In reality it generally becomes much deeper, chiefly perhaps because [the angle*

of deviation] α is diminished by the resistance of lands, and of the water in other regions of the Ocean, etc. But it is also probable that the assumed [coefficient of the internal friction of the water] K is much too small, and Mr. Ekman has therefore, at my request, made an attempt to calculate K from our observations". In addition to the uncertainty introduced by turbulence, the Ekman model does not account for vertical density stratification.

In real wind-driven surface layers, the angle between the surface stress and the surface current direction is less than the 45° predicted by the Ekman model. This angle is typically found to be between 5° and 20° (Cushman-Roisin, 1994). One possible contribution to this deviation is wave-induced current. The wind generates waves propagating in the wind direction. Wave-induced currents will also be in the direction of the wind. Hence, the resultant velocity of the wave-induced and the purely wind-induced current has a smaller angle to the wind direction than predicted, if wave-induced current is not taken into account.

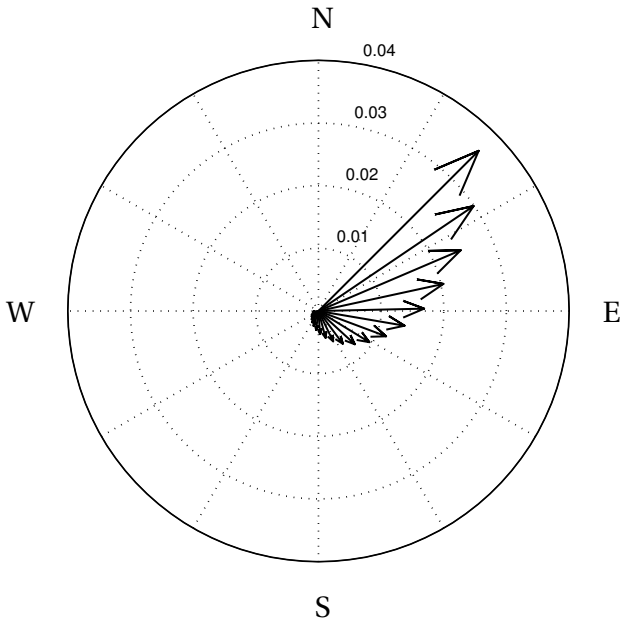

Figure 14: Ekman surface spiral with a constant eddy viscosity $\nu_T = 10^{-1}\, m^2 s^{-1}$. *The dimensions of the velocities are* m/s. *The vertical distance between the velocity vectors is 10 m. The wind direction is towards the north.*

3.3 Wave-current interaction

The most evident effect of interaction between waves and currents are the effects on the waves, i.e. changes in wave height and propagation direction. These effects are not of interest in this work, but interaction effects on the current structure are. Changes of the mean current profiles are mainly seen very close to the bed, where the current speed is suppressed in the presence of surface waves. The effect is analogous to that of an increased bottom roughness z_0. The reason for this behavior is wave-induced mixing close to the bed (Nielsen, 1992). This mixing decreases rapidly towards the surface, and the current profile in the first meters from the bottom in the presence of waves is therefore generally taken as the logarithmic profile

$$\overline{u}(z) = \frac{\overline{u_*}}{\kappa} \ln\left(\frac{z}{z_a}\right). \tag{3.12}$$

Here, z_a is the modified bottom roughness taking into account the apparent increase in bottom roughness felt by the flow in the presence of waves. Expectedly, z_a will be a function of current strength, bottom roughness and the direction of the waves relative to the current. Experiments indicate that the modified roughness is greater for waves opposing the current than for waves following the current (Nielsen, 1992). According to Nielsen (1992), the description of the current profile given above is reasonable when comparing with existing experimental data, although the logarithmic profile is not always obvious. The effect of waves on a current is visualized in figure 15. In figure (a), measurements in an oscillating water tank are shown, for current alone, waves alone and the combined flow of both a steady current and waves. The effect of suppressed velocities close to the bottom in the presence of waves is evident. In figure (b), a simple sketch of the theoretic logarithmic profile with a modified roughness z_a is shown.

It should be noted that, although the above discussion considers stationary currents only, the magnitude and direction of tidal flows vary so slowly that they can be considered as quasi-steady. Hence, the effect of waves on tidal currents should be approximately the same as described above.

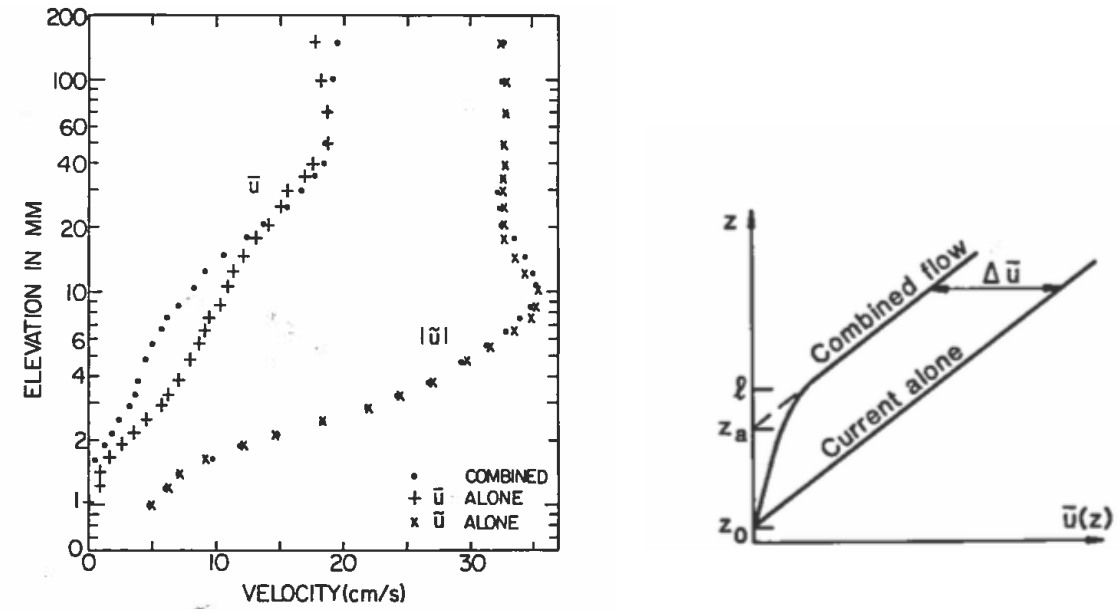

(a) *(b)*

Figure 15: Visualizations of the effect of surface waves on a steady current. In figure (a), the flow is decomposed into a steady component $\overline{u}$ and a periodic component $\tilde{u}$. (+) denotes pure current, (x) denotes oscillatory flow (waves) and (•) denotes the combined flow. The elevation from the bottom is plotted with a logarithmic scale. The data points are from measurements made by Van Doorn (1982) in an oscillating water tunnel. In (b), a simple illustration of the effect of waves on the current profile is given. Close to the bed, the velocity is smaller under the presence of waves, due to wave-induced mixing. A little further from the bed, from a distance l, the velocity profile of the combined flow has the well-known logarithmic shape (here, the z axis is logarithmic), but with an apparent bottom roughness $z_a > z_0$. Both figures are taken from Nielsen (1992).

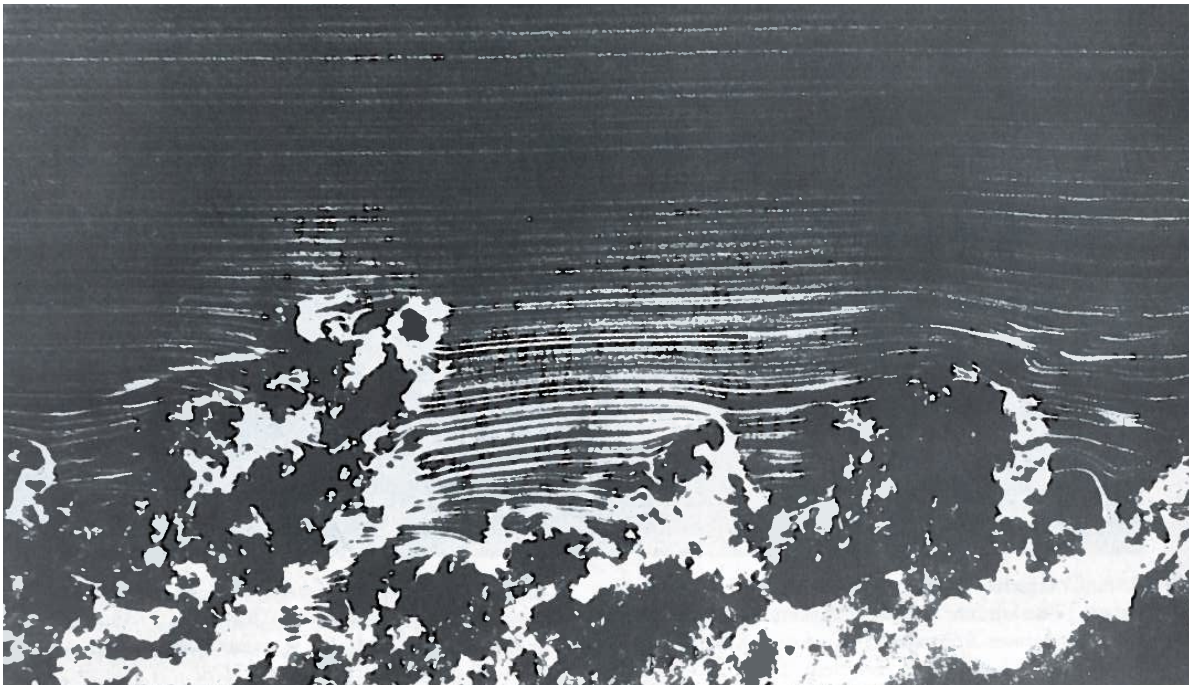

Figure 16: Turbulent boundary layer over a flat plate. A smoke wire generates streamlines in a wind tunnel. The chaotic nature of a turbulent boundary layer is evident. Photograph by Thomas Corke, Y. Guezennec and Hassan Nagib, from Van Dyke (1982).

4 Turbulence and turbulence modeling

Fluid flows are very often classified as either laminar, transitional or turbulent. A laminar flow is characterized by smooth, predictable fluid motion, while turbulent flows are unsteady and chaotic. As noted by Pope (2000), an important feature of turbulent flows is that the velocity field varies irregularly in both time and space. When a flow is going from laminar to turbulent state, or when it alternates between the two states, it is called transitional. Turbulence is a topic of great interest for physicists, engineers, meteorologists and oceanographers. The reason for this is that, while turbulence is a phenomenon not fully understood, proper modeling of turbulence is essential to predict or model flows that are turbulent, and this has proven to be a challenging task. The background for this chapter is primarily the doctoral thesis by Holmedal (2002) and *Turbulent flows* by Pope (2000).

Natural flows are often turbulent. Geophysical flows, like the large-scale flows in the oceans, typically have very high Reynolds numbers (see e.g. Cushman-Roisin, 1994). The flow state depends on several parameters, but it is to a large degree determined by the Reynolds

number, defined as the ratio of inertial forces to viscous forces, or $Re = (UL)/\nu$, where U is the current speed, L is a characteristic length scale, and ν is the kinematic viscosity. For high Reynolds numbers, the flow is turbulent.

There exist numerous methods for simulation or modeling of turbulent flows. The choice of turbulence model, or simulation method, is an essential part of the modeling of all turbulent flows, and it must be taken into account in each individual case. We define turbulent-flow simulations as methods where the solved equations describe the actual velocity field (u, v) for one realization of the flow. The definition of a turbulence model is that equations are instead solved for some mean values (Pope, 2000). Here, Reynolds stress models and the application of the generalized eddy viscosity are described in detail, and the simulation methods direct numerical simulation (DNS) and large-eddy simulation (LES) are discussed briefly.

4.1 Reynolds stress models

Using Einstein's summation convention, the incompressible Navier Stokes equations can be written as

$$\frac{\partial u_i}{\partial x_i} = 0 \tag{4.1}$$

$$\frac{\partial u_i}{\partial t} + \frac{\partial u_i u_j}{\partial x_j} = -\frac{1}{\rho}\frac{\partial p}{\partial x_i} + \nu\frac{\partial^2 u_i}{\partial x_j \partial x_j}. \tag{4.2}$$

Einstein's summation convention is a method for effectively writing equations involving sums, where all terms which include the same index two times is the sum of the same term for all the values of the index. Here, the values of the indices are $i = 1,2,3$, so that $x_i(i = 1,2,3) = (x, y, z)$ are the Cartesian coordinates and the velocity components are $u_i(i = 1,2,3) = (u, v, w)$. p is the pressure. This version of the Navier Stokes equations is adopted from Holmedal (2002).

To separate the average and fluctuating parts of the flow, we use the Reynolds decomposition proposed by Osborne Reynolds:

$$u(x_i, t) = \overline{u(x_i, t)} + u'(x_i, t) \tag{4.3}$$

$$p(x_i, t) = \overline{p(x_i, t)} + p'(x_i, t). \tag{4.4}$$

Here, $\overline{u(x_i,t)}$ and $\overline{p(x_i,t)}$ denotes the average velocity and pressure fields, respectively, while $u'(x_i,t)$ and $p'(x_i,t)$ denotes the fluctuations. By inserting (4.3) into (4.1), we obtain

$$\frac{\partial \overline{u_i}}{\partial x_i} + \frac{\partial u_i'}{\partial x_i} = 0. \tag{4.5}$$

Similarly, by inserting (4.3) and (4.4) into (4.2), we get

$$\frac{\partial \overline{u_i}}{\partial t} + \frac{\partial u_i'}{\partial t} + \frac{\partial \overline{u_i}\,\overline{u_j}}{\partial x_j} + \frac{\partial \overline{u_i} u_j'}{\partial x_j} + \frac{\partial u_i' \overline{u_j}}{\partial x_j} + \frac{\partial u_i' u_j'}{\partial x_j} = -\frac{1}{\rho}\frac{\partial \overline{p}}{\partial x_i} - \frac{1}{\rho}\frac{\partial p'}{\partial x_i} + \nu\frac{\partial^2 \overline{u_i}}{\partial x_j \partial x_j} + \nu\frac{\partial^2 u_i'}{\partial x_j \partial x_j}. \tag{4.6}$$

We now average the equations (4.5) and (4.6), and utilize that the mean of a fluctuation is zero and that averaging a mean value does not change the value. This results in the Reynolds averaged Navier Stokes (RANS) equations:

$$\frac{\partial \overline{u_i}}{\partial x_i} = 0 \tag{4.7}$$

$$\frac{\partial \overline{u_i}}{\partial t} + \frac{\partial \overline{u_i}\,\overline{u_j}}{\partial x_j} = -\frac{1}{\rho}\frac{\partial \overline{p}}{\partial x_i} + \nu\frac{\partial^2 \overline{u_i}}{\partial x_j \partial x_j} - \frac{\partial \overline{u_i' u_j'}}{\partial x_j}. \tag{4.8}$$

The last term in (4.8) is called *Reynolds stresses* or *turbulent stresses*, and they must be modeled.

4.2 Generalized eddy viscosity

One way to model the Reynolds stresses is by using the eddy viscosity concept introduced by Joseph Boussinesq in 1877. The concept involves an assumption that the Reynolds stresses are proportional to the mean velocity gradients (Holmedal, 2002). The generalized eddy viscosity concept can be written as

$$-\overline{u_i' u_j'} = \nu_T\left(\frac{\partial \overline{u_i}}{\partial x_j} + \frac{\partial \overline{u_j}}{\partial x_i}\right) - \frac{2}{3}k\delta_{ij}. \tag{4.9}$$

Here, k is the turbulent kinetic energy, defined as

$$k = \frac{1}{2}\overline{u_i' u_j'}. \tag{4.10}$$

δ_{ij} is the Kronecker delta function, defined as

$$\delta_{ij} = \begin{cases} 1, & \text{if } i = j \\ 0, & \text{if } i \neq j \end{cases}.$$

ν_T is the eddy viscosity. We want to insert the general eddy viscosity into the RANS equations. We use that the mean rate of strain is defined as

$$\overline{S_{ij}} \equiv \frac{1}{2} * \left(\frac{\partial \overline{u_i}}{\partial x_j} + \frac{\partial \overline{u_j}}{\partial x_i} \right).$$

We can now write the last term in (4.8) as

$$-\frac{\partial \overline{u_i' u_j'}}{\partial x_j} = 2\frac{\partial}{\partial x_j}(\nu_T \overline{S_{ij}}) - \frac{\partial}{\partial x_j}(\frac{2}{3}k\delta_{ij}). \tag{4.11}$$

The last term in (4.11) can, using Einstein's summation convention and the definition of the Kronecker delta function, be written as

$$\frac{\partial}{\partial x_j}\left(\frac{2}{3}k\delta_{ij}\right) = \sum_{j=1}^{3} \frac{\partial}{\partial x_j}\left(\frac{2}{3}k\delta_{ij}\right) = \frac{\partial}{\partial x_i}\left(\frac{2}{3}k\right). \tag{4.12}$$

Now, inserting (4.11) and (4.12) into (4.8), we get

$$\frac{\partial \overline{u_i}}{\partial t} + \frac{\partial \overline{u_i}\,\overline{u_j}}{\partial x_j} = -\frac{1}{\rho}\frac{\partial}{\partial x_i}(\overline{p} + \frac{2}{3}\rho k) + \nu\frac{\partial^2 \overline{u_i}}{\partial x_j \partial x_j} + 2\frac{\partial}{\partial x_j}(\nu_T \overline{S_{ij}}). \tag{4.13}$$

Here the pressure term and the term containing k have been combined. This can be done because both p and k are scalars. To make use of this result, we need to specify the eddy viscosity ν_T. Depending on how we do this, our model will normally be either a zero-equation model, a one-equation model or a two-equation model. In zero-equation models, the eddy viscosity is specified from experiments or from an empirical formula. Based on dimensional considerations, we can write the eddy viscosity as the product of a velocity and a length:

$$\nu_T = V^* l^*. \tag{4.14}$$

In the *mixing length model* introduced by Ludvig Prandtl, the length is called the mixing length, $l^* = l_m$, and the velocity scale is written

$$V^* = l_m |\frac{\partial \overline{u}}{\partial z}|, \tag{4.15}$$

such that the eddy viscosity is

$$\nu_T = l_m^2 |\frac{\partial \overline{u}}{\partial z}|. \tag{4.16}$$

As no transport equations are solved, the mixing length model is a zero-equation model. Equation (4.15) implies that the turbulent velocity scale is zero when the velocity gradient

$\frac{\partial \overline{u}}{\partial z}$ is zero. However, this is not in general true (see e.g. Pope, 2000), and the mixing length model is therefore generally taken as being erroneous.

Kolmogorov (1942) and Prandtl (1945) both proposed to write the velocity scale as $V^* = c\sqrt{k}$. This gives rise to one- and two-equation models. By still taking the mixing length l_m as the length scale, we obtain the Kolmogorov-Prandtl relation:

$$\nu_T = c\sqrt{k} l_m, \tag{4.17}$$

where c is a constant. If a transport equation for k is solved and this is the only transport equation used for turbulence quantities, our model is a one-equation model. In two-equation models, transport equations are solved for two turbulence quantities. A much used two-equation model is the $k-\epsilon$ model, where transport equations are solved for both k and ϵ. ϵ is the rate of dissipation of turbulent kinetic energy. The exact transport equation for k, obtained from manipulation of the Navier Stokes equations, is (Holmedal, 2002):

$$\frac{\partial k}{\partial t} + \overline{u_j}\frac{\partial k}{\partial x_j} = D_k + P_k - \epsilon, \tag{4.18}$$

where

$$D_k = -\frac{\partial}{\partial x_i}\left(\overline{u_i'(\frac{p'}{p} + k)}\right) - \nu\frac{\partial}{\partial x_i}\left(\overline{u_j'(\frac{\partial u_i'}{\partial x_j} + \frac{\partial u_j'}{\partial x_i})}\right) \tag{4.19}$$

$$P_k = -\overline{u_i' u_j'}\frac{\partial \overline{u_i}}{\partial x_j} \tag{4.20}$$

$$\epsilon = \overline{\nu(\frac{\partial u_i'}{\partial x_j} + \frac{\partial u_j'}{\partial x_i})(\frac{\partial u_i'}{\partial x_j} + \frac{\partial u_j'}{\partial x_i})}. \tag{4.21}$$

D_k is the diffusion term, which contains the diffusion of turbulent kinetic energy. The first term in D_k vanishes if we integrate it over the turbulence volume. We therefore skip this term. Based on physical considerations (see e.g. Holmedal, 2002), the last term in (4.19) is modeled as

$$D_k = \frac{\partial}{\partial x_j}(\frac{\nu_T}{\sigma_k}\frac{\partial k}{\partial x_j}). \tag{4.22}$$

Here, σ_k is a constant. P_k is the production term, and represents the production of turbulent kinetic energy. This term is modeled as

$$P_k = \nu_T\left(\frac{\partial \overline{u_i}}{\partial x_j} + \frac{\partial \overline{u_j}}{\partial x_i}\right)\frac{\partial \overline{u_i}}{\partial x_j}. \tag{4.23}$$

This model equation for P_k is found by inserting (4.9) and (4.1) into (4.20). To find a model equation for ϵ, we use the cascade theory introduced by Richardson (1922). In this theory, it is assumed that turbulent energy is transferred from larger eddies to smaller eddies all the way from the largest eddies in the flow to the smallest. From the smallest eddies, the energy is dissipated. We neglect viscous effects for the large eddies. This means that we can model the diffusion based on the velocity scale V_m and length scale l_m of the largest eddies in the flow. By considering the dimensions we can write $\epsilon \sim V_m^3/l_m$. We insert the assumption $V^* = V_m = c\sqrt{k}$ proposed by Prandtl and Kolmogorov, and obtain

$$\epsilon = C_D \frac{k^{\frac{3}{2}}}{l_m}. \tag{4.24}$$

C_D is an empirical constant. Inserting the model equations for D_k, P_k and ϵ into (4.18), we get the following equation for k:

$$\frac{\partial k}{\partial t} + \overline{u_j}\frac{\partial k}{\partial x_j} = \frac{\partial}{\partial x_j}(\frac{\nu_T}{\sigma_k}\frac{\partial k}{\partial x_j}) + \nu_T\left(\frac{\partial \overline{u_i}}{\partial x_j} + \frac{\partial \overline{u_j}}{\partial x_i}\right)\frac{\partial \overline{u_i}}{\partial x_j} - C_D\frac{k^{\frac{3}{2}}}{l_m}. \tag{4.25}$$

We have now found a transport equation for the length scale V_m. This can be used as a one-equation model, or we can find a transport equation for l_m as well, to obtain a two-equation model. Such models are generally more accurate than one-equation models. Often, a transport equation for $k^a l_m^b$ is used instead of a transport equation for l_m only. a and b are constants. According to Holmedal (2002), the most famous $k-\epsilon$ model is the one where $a = 3$ and $b = -1$. By solving the model equation for ϵ for l_m and inserting into the Kolmogorov-Prandtl relation (4.17) and using $V^* = V_m = c\sqrt{k}$, we get

$$\nu_T = C_D C_\mu \frac{k^2}{\epsilon} \equiv c_1 \frac{k^2}{\epsilon}. \tag{4.26}$$

Like C_D, C_μ is also an empirical constant. Similarly as for the turbulent kinetic energy k, a transport equation for ϵ can be obtained by manipulation of the Navier Stokes equations. The most common form of the $k-\epsilon$ model for high Reynolds numbers is (Holmedal, 2002):

$$\frac{\partial k}{\partial t} + \overline{u_j}\frac{\partial k}{\partial x_j} = \frac{\partial}{\partial x_j}(\frac{\nu_T}{\sigma_k}\frac{\partial k}{\partial x_j}) + \nu_T\left(\frac{\partial \overline{u_i}}{\partial x_j} + \frac{\partial \overline{u_j}}{\partial x_i}\right)\frac{\partial \overline{u_i}}{\partial x_j} - \epsilon \tag{4.27}$$

$$\frac{\partial \epsilon}{\partial t} + \overline{u_j}\frac{\partial \epsilon}{\partial x_j} = \frac{\partial}{\partial x_j}(\frac{\nu_T}{\sigma_\epsilon}\frac{\partial \epsilon}{\partial x_j}) + c_{\epsilon 1}\frac{\epsilon}{k}\nu_T\left(\frac{\partial \overline{u_i}}{\partial x_j} + \frac{\partial \overline{u_j}}{\partial x_i}\right)\frac{\partial \overline{u_i}}{\partial x_j} - c_{\epsilon 2}\frac{\epsilon^2}{k}, \tag{4.28}$$

where ν_T is given in equation (4.26). This model contains five constants $(c_1, \sigma_k, \sigma_\epsilon, c_{\epsilon 1}, c_{\epsilon 2})$. The normal procedure is to use standard empirical values for flow over a flat plate. Further, the boundary conditions must be chosen in each specific case.

4.3 Turbulent-flow simulation methods

In direct numerical simulation (DNS), the Navier Stokes equations are solved. The result is the velocity field for one realization of the flow. This method has a high degree of accuracy, and is simple to use. However, it requires large amounts of computational power, limiting its applicability. According to Pope (2000), the cost of running DNS simulations increases as Re^3, which means that it applies only for flows with low or moderate Reynolds number.

In large-eddy simulation (LES), large-scale turbulent motions are directly simulated, while smaller motions are modeled. The velocity is filtered, such that the flow is divided into one component representing the large eddies in the flow, and one representing the flow without the large eddies. The large amount of computational power needed for DNS is mainly due to the smaller eddies. LES is therefore less demanding with regards to computational power and cost. It is more demanding than RANS models, but for flows with large-scale unsteady motions, LES is expected to be more accurate (Pope, 2000).

4.4 Roughness effects and flow regimes

Depending on the bottom conditions, the velocity magnitudes and the fluid viscosity, turbulent flows along a boundary may be classified as hydrodynamically smooth, transitional or rough. A flow is said to be hydrodynamically smooth if the roughness elements (the small irregularities on the bottom) are submerged by the laminar sublayer close to the boundary. Correspondingly, the flow is hydrodynamically rough if the roughness elements penetrate the laminar sublayer (see e.g. Nielsen, 1992). The laminar sublayer is also called the viscous or linear sublayer. This is the flow region closest to the boundary. In this region, the velocity distribution is close to linear (Çengel and Cimbala, 2010). The type of flow regime can be identified from the Reynolds roughness number Rr, given as

$$Rr = \frac{u_* z_0}{\nu}, \tag{4.29}$$

where u_* is the *friction velocity* defined as

$$u_* = \sqrt{\frac{\tau_0}{\rho}}. \tag{4.30}$$

τ_0 is the bottom shear stress. For low values of Rr, i.e. for hydrodynamically smooth flows, we have no roughness effects. In other words, the flow is similar to what we would have in

the case of flow over a perfectly smooth plate. For high Reynolds roughness numbers, i.e. for fully rough flows, roughness effects dominate the flow, and the effect of molecular viscosity becomes negligible (see e.g. Schlichting et al., 2000). In Soulsby (1997), the limiting values for the three types of flow regimes are defined as functions of $u_* k_s/\nu$, where k_s is the Nikuradse equivalent sand grain roughness. Using the equation

$$z_0 = \frac{k_s}{30} + \frac{\nu}{9u_*}, \tag{4.31}$$

given in Soulsby (1997), first used by Colebrook and White (1937), we find the limiting values of Rr as

$Rr < 0.28$ for smooth flow

$0.28 < Rr < 2.44$ for transitional flow

$Rr > 2.44$ for rough flow

It should be noted that neither z_0 nor k_s is necessarily the actual height of the roughness elements on the bottom. Because different bed materials and configurations of the roughness elements affect the flow differently, we relate the roughness effects to those of sand beds through an equivalent sand roughness. k_s (or z_0) can be determined by measuring the velocity distribution above the bed and adapting the logarithmic profile.

5 Model formulation

The present model is the same model as the one used by Holmedal and Myrhaug (2013). It is a one-dimensional model, in the sense that the velocities are calculated at grid points along a vertical line from the seabed to the surface. The model is thoroughly described in Holmedal and Myrhaug (2013). A summary is given below.

5.1 Governing equations

We consider tidal flow over a flat bottom of infinite horizontal extent. The coordinate system (x,y,z) is placed such that the x-axis points to the east, and the y-axis to the north. The origin is placed on the sea floor, and the z-axis points towards the surface. The Reynolds averaged Navier-Stokes equations deduced in section 4 are simplified using the boundary layer approximation. The basis of the simplification is that, in a boundary layer, the vertical velocities are much smaller than the horizontal velocities. This can be shown by a scale analysis. The boundary layer approximation is considered valid for tidal flows over shallow and intermediate depths. Together with the assumption of horizontally uniform flow (no advective terms), this gives

$$\frac{\partial u}{\partial t} = -\frac{1}{\rho}\frac{\partial p}{\partial x} + \frac{\partial}{\partial z}\left(\nu_T \frac{\partial u}{\partial z}\right) + f v \tag{5.1}$$

$$\frac{\partial v}{\partial t} = -\frac{1}{\rho}\frac{\partial p}{\partial y} + \frac{\partial}{\partial z}\left(\nu_T \frac{\partial v}{\partial z}\right) - f u. \tag{5.2}$$

To properly model the turbulence, a $k-\epsilon$ model is used. The transport equations for k and ϵ given by equations (4.27) and (4.28) are subjected to the boundary layer approximation, yielding

$$\frac{\partial k}{\partial t} = \frac{\partial}{\partial z}\left(\frac{\nu_T}{\sigma_k}\frac{\partial k}{\partial z}\right) + \nu_T\left(\left(\frac{\partial u}{\partial z}\right)^2 + \left(\frac{\partial v}{\partial z}\right)^2\right) - \epsilon \tag{5.3}$$

$$\frac{\partial \epsilon}{\partial t} = \frac{\partial}{\partial z}\left(\frac{\nu_T}{\sigma_\epsilon}\frac{\partial \epsilon}{\partial z}\right) + c_{\epsilon 1}\frac{\epsilon}{k}\nu_T\left(\left(\frac{\partial u}{\partial z}\right)^2 + \left(\frac{\partial v}{\partial z}\right)^2\right) - c_{\epsilon 2}\frac{\epsilon^2}{k}, \tag{5.4}$$

where the eddy viscosity ν_T is given by (4.26). The standard empirical values for the constants are used: $(c_1, c_{\epsilon 1}, c_{\epsilon 2}, \sigma_k, \sigma_\epsilon) = (0.09, 1.44, 1.92, 1.00, 1.30)$.

5.2 Boundary conditions

5.2.1 At the seabed

The boundary conditions for the velocity at the bottom is the no-slip condition

$$u = 0,\ v = 0 \text{ at } \mathrm{z} = \mathrm{z}_0, \tag{5.5}$$

where z_0 is the seabed roughness height. The boundary conditions for the turbulence quantities k and ϵ are

$$k = \nu_T \sqrt{\frac{\left(\frac{\partial u}{\partial z}\right)^2 + \left(\frac{\partial v}{\partial z}\right)^2}{c_1}} \tag{5.6}$$

$$\epsilon = (c_1)^{3/4} \frac{k^{3/4}}{\kappa z_0}. \tag{5.7}$$

This is based on the assumption of local equilibrium between production and dissipation of turbulence (Holmedal and Myrhaug, 2013). Equation (5.6) and (5.7) is evaluated at the node closest to the sea floor.

5.2.2 At the surface

In linear (first order) wave theory, the boundary conditions at the surface are evaluated at the mean free surface. Linear wave theory is valid for small wave steepnesses. Due to the extremely long wavelengths of tidal waves, their steepness is very small. Therefore, similarly as in linear wave theory, the boundary conditions are evaluated at the mean free surface in this model, for simplicity. At the sea surface, the flow is assumed to be unaffected by the seabed, and there is no friction between the water and the atmosphere. Hence, there is no shear stress at the surface, such that

$$\frac{\partial u}{\partial z} = 0,\ \frac{\partial v}{\partial z} = 0. \tag{5.8}$$

The boundary conditions for the turbulence quantities at the surface is zero flux, giving

$$\frac{\partial k}{\partial z} = 0,\ \frac{\partial \epsilon}{\partial z} = 0. \tag{5.9}$$

5.3 Forcing function

The horizontal velocities in the interior flow is written $(u, v) = (U_0, V_0)$. It can be shown that the assumption of validity of the boundary layer approximation implies constant horizontal pressure gradients through the water column (see e.g. the deduction of the Ekman layer equations in appendix D). Equations (5.1) and (5.2) subjected to the conditions in the interior flow (with no shear) then yield

$$-\frac{1}{\rho}\frac{\partial p}{\partial x} = \frac{\partial U_0}{\partial t} - fV_0 \tag{5.10}$$

$$-\frac{1}{\rho}\frac{\partial p}{\partial y} = \frac{\partial V_0}{\partial t} + fU_0 \tag{5.11}$$

The values for U_0 and V_0 are taken from field measurements made by a research team at the University of the Highlands and Islands (UHI) in Scotland. These measurements were done at several elevations over the bottom, at a total depth of about 13 m. The values taken as U_0 and V_0 are the velocities measured at an elevation of 9.15 m above the sea floor, as these are assumed to be least affected by friction from the bottom or from wind over the surface. The measurements are discussed further in chapter 7.

5.4 Numerical method

The coupled governing equations (5.1) - (5.4) are solved by a finite difference method (see Holmedal and Myrhaug, 2013). The mesh is stretched such that the resolution increases towards the bottom, where the flow is more complex than towards the surface, for tidal flow alone. The four governing equations, for u, v, k and ϵ, must be solved simultaneously in time. In short, they are solved by integration in time.

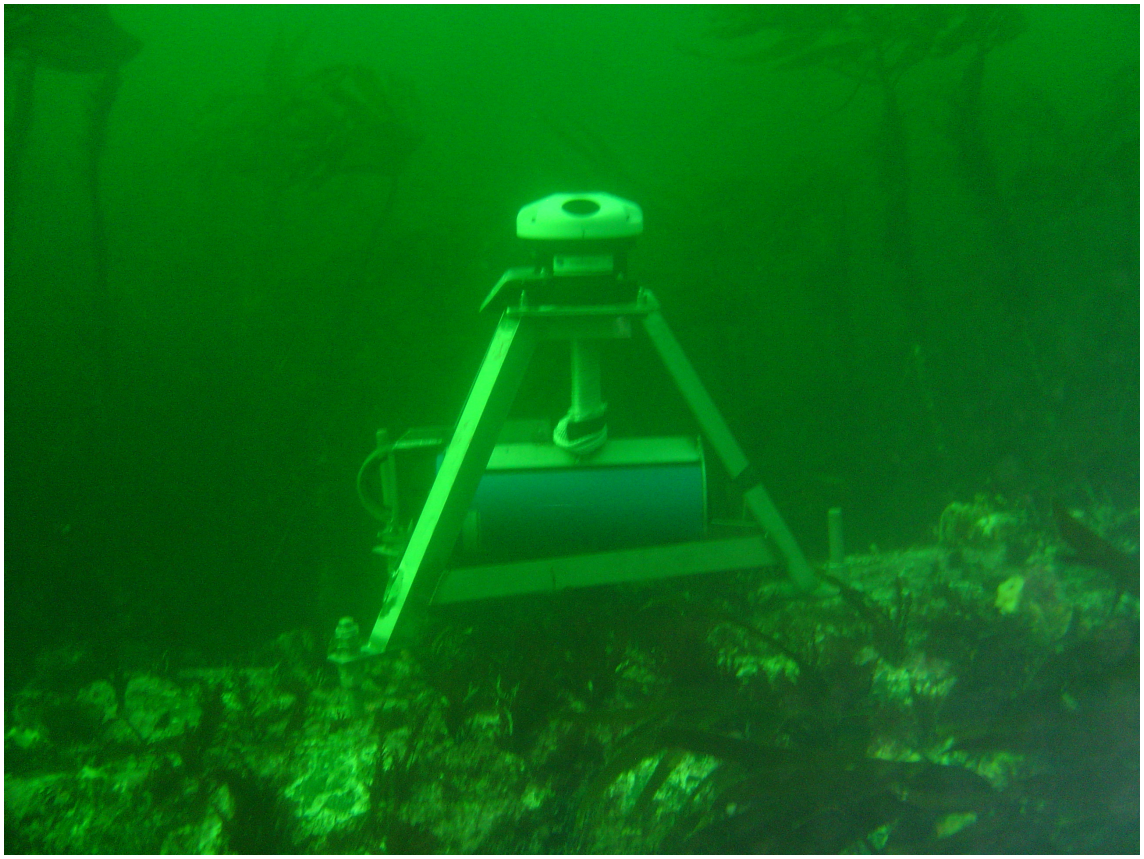

Figure 17: AWAC system placed on the seabed near the coast of the Hebrides. The picture illustrates the complex bottom conditions at the measuring site, with different types of vegetation. (Vögler, 2015).

6 Field data

The field data used in the present work was collected by a research team at the University of the Highlands and Islands (UHI) in Scotland, in association with the MERIKA (Marine Energy Research Innovation and Knowledge Accelerator) project. The measurements were made outside the coast of the Hebrides, Scotland, during February and May of 2013. They were made using an acoustic AWAC (Acoustic Wave And Current) system placed at the bottom about 700 m from the shore. This system records current and wave data by utilizing the Doppler effect. The current was recorded in cells of 1 m throughout the water column from the transducer head, which was placed 0.75 m above the bottom. The mean water depth at the measuring site is about 13 m, and the tidal range at spring tide is about 4.5 m. The bottom conditions are quite complex, consisting of bedrock with seaweed and boulders. Figure 17

illustrates the complexity of the bottom. The tall seaweeds vaguely visible in the background, of approximately 1 m length, are of the species Laminaria hyperborea.

Figures 18 and 19 show the location of the transducer. In figure 18, the depth contours are indicated by colors. The bottom contours and the coastline are relatively straight. The measured surface elevation time series during February and May 2013 are shown in figure 20. The oscillations with period approximately equal to the theoretical M_2 period of 12.42 hours are evident. In figure 21, the tidal component of the surface elevation is shown, without the wind wave oscillations. The wave oscillations, and other possible components of frequencies much higher than those of the tides, are excluded simply by averaging over each period of wave measurements, i.e. periods of one half hour. Note that figure 20, where wind waves are included, does not illustrate the spring-neap pattern in a good way. This is because time intervals of higher wave activity may be mistaken for spring tide. In figure 21, however, the spring-neap pattern is obvious. It is clear that the tides at the measuring location is of the semidiurnal type. The different types of tides are described in chapter 2.3. In figures 22 and 23, the full surface elevation data, including both tidal and wind wave components, are shown in time series of shorter periods. This allows for the varying wave conditions to be identified. In time intervals where the figures show a high degree of scatter, e.g. for about t $\in$ <310,360> h of February and t $\in$ <290,340> h of May, we have considerable wave activity. Where there is a low degree of scatter, e.g. for t $\in$ <540,590> h of February and t $\in$ <170,240> h of May, the wave activity is relatively small. Due to a storm during the first days of February, aeration in the water column disturbed the measurements. For the surface tracking, an alternative, but less accurate, measurement method was used, to account for this. Therefore, the high scatter in figures 20 and 22 during approximately hours 50 - 130 of February does not represent the real wave heights present at the time well. The measured velocities during this period (see figure 27) are also highly irregular and the magnitudes are very high. Therefore, the first 150 hours of the February data will be excluded from the analyses.

It should be noted that the coordinate system used in the measurements is defined according to magnetic north. The magnetic declination at the transducer location was 6.65 degrees west at the time when the measurements were done. The coordinate system is the same for the field data and the model results, so magnetic declination does not cause deviations between these. However, if we e.g. want to compare flow directions with the topogra-

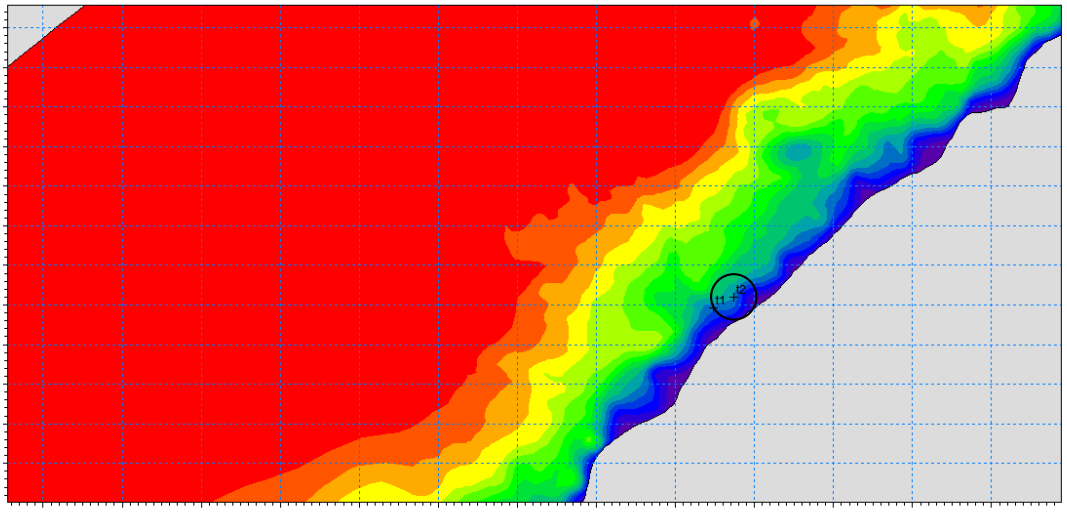

(a)

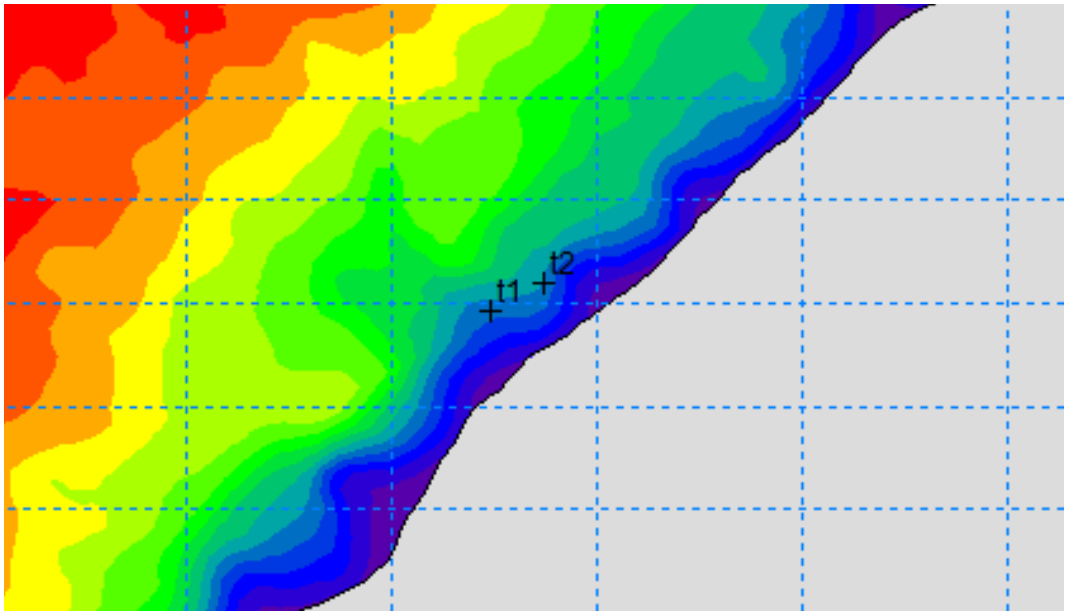

(b)

Figure 18: Topographic maps of the measuring location. The grey and purple areas are land, and the depth increases away from the coast in the north-west direction. The equidistance between succeeding colors is 2.667 m. In figure (b), the scale is reduced relative to in (a). In (a), the transducer location is in the center of the black circle. In (b), it is at the 't2' mark. The map is aligned according to true north. (Vögler, 2015).

Figure 19: Satellite photo of the measuring location. The transducer location is at the 'AWAC2' mark. The map is aligned according to true north. (Vögler, 2015).

phy map in figure 18, the magnetic declination must be taken into account.

6.1 Data splining and filtering

As the AWAC system cannot measure wave and current data simultaneously, it was set to alternate between recording the two in 30-minute periods. In other words, subsequent half-hours were dedicated to wave and current measurements, respectively. The current data were sampled three times during these half-our periods, with 10-minute intervals. For each current sample (of which there are three per hour), measurements were done over 60 seconds, and the averaged velocities over this time interval were filed. The wave data were recorded with one-second intervals. The white columns in the surface elevation plots (or wave plots) in figures 22 and 23 are the time intervals of current measurements.

To produce current-data of constant intervals, the data points were interpolated by cubic splining in MATLAB. As expected, both the surface elevation (or wave) signals and the current signals contain oscillations of higher frequencies than those of pure tidal flow. The main reasons for this are probably wave activity and currents induced by wind over the sea surface and by wind-generated waves. In the current measurements, the oscillating velocity compo-

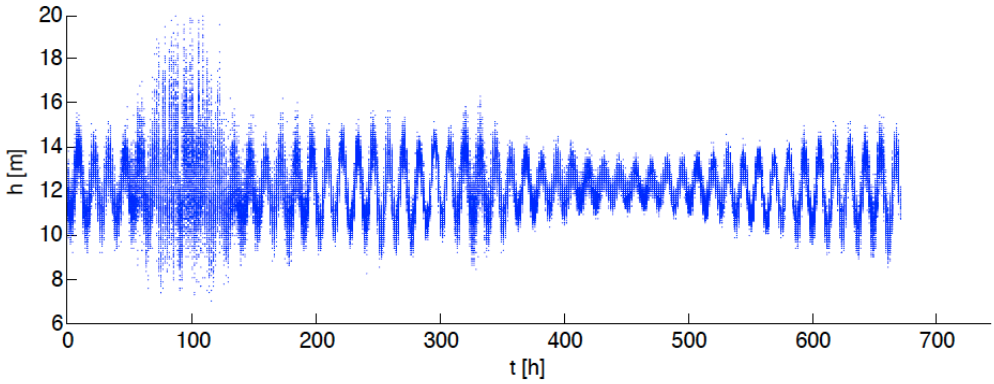

(a)

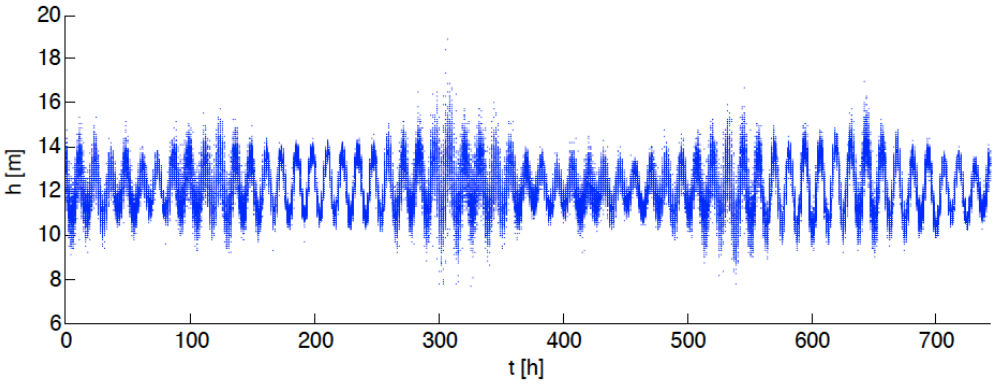

(b)

Figure 20: Scatter plot of the surface elevation during (a) February and (b) May 2013. The chaotic scatter in the area around 100 hours in (a) is due to the use of a less accurate measuring technique in this time interval. This technique was used because aeration in the water column disturbed the AST (Acoustic Surface Tracking) measurements, which are more accurate.

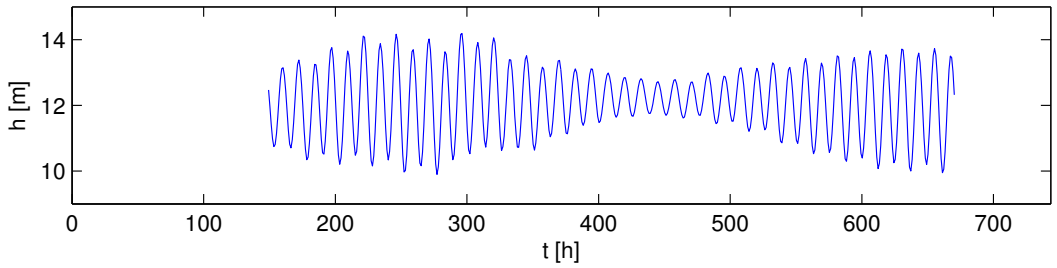

(a)

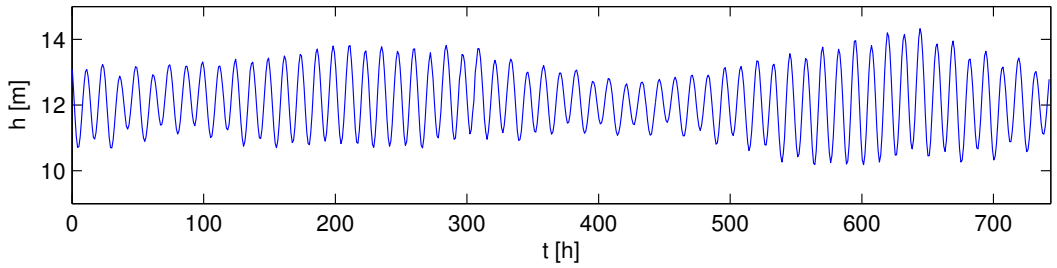

(b)

Figure 21: Tidal component of the surface elevation during (a) February and (b) May 2013. The surface elevation during the first few days of February is not evaluated due to the less accurate measuring technique that was used during this period.

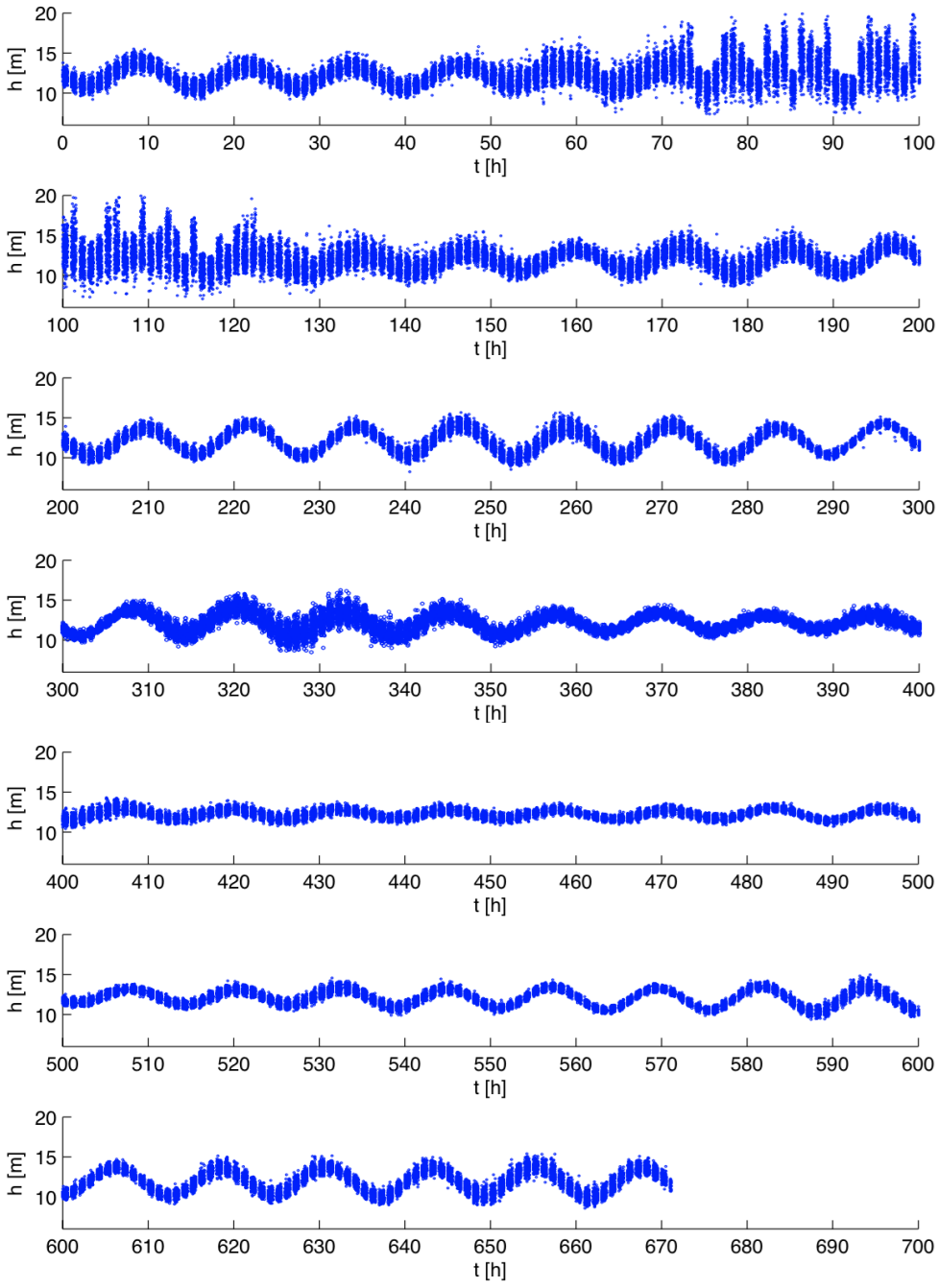

Figure 22: Scatter plot of the surface elevation during February 2013.

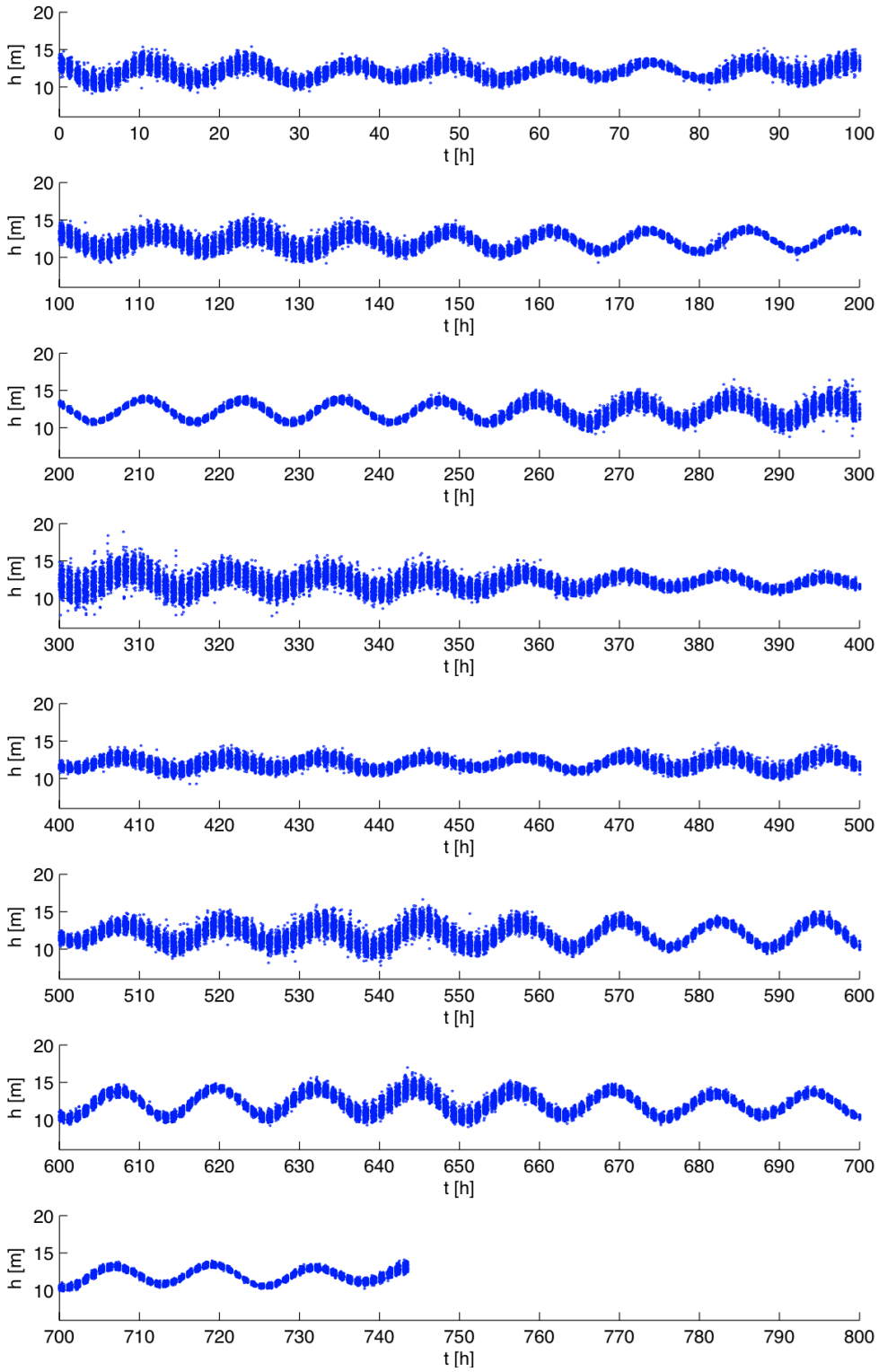

Figure 23: Scatter plot of the surface elevation during May 2013.

nents as a direct effect of the water particles' orbit motion under wind waves are removed by the time averaging mentioned above. Still, time series of the measured currents and their frequency spectra show that frequency components of non-tidal frequencies are present also in the current data. The frequency spectra of the signals are shown in figure 24. For all the plots except for the spectrum of the v component for February, the highest peak is at f = $2.24{\cdot}10^{-5}$ Hz, corresponding to a period of 12.40 h, very close to the theoretical M_2 period of 12.42 h. In figure 25, the seven basic tidal constituents described in chapter 2.3 is shown together with the frequency spectrum for the u velocity of May 2013. All of these correspond quite well to peaks of the frequency spectrum, except for the L_2 component. However, the theoretical magnitude of L_2 is only 3 percent of the M_2 magnitude and significantly smaller than the other five (Hicks, 2006).

To remove the unwanted frequency components, a lowpass Butterworth filter was applied in MATLAB. The built-in MATLAB function *filtfilt*, which filters both forwards and in reverse to avoid phase shift, was used. The choice of cut-off frequency is not obvious. Of the seven tidal constituents presented by Hicks (2006), related to the fundamental astronomical elements, the constituent period ranges from 12.00 h for the S_2 constituent to 25.82 h for O_1. However, these seven constituents are not sufficient to describe complex tidal flow in shallow water. The 37 constituents used by the U.S. Government's Center for Operational Oceanographic Products and Services (CO-OPS) for their tidal predictions at most locations (see chapter 2) are presented by Parker (2007). Of these, the constituents of the lowest periods are M_8 (3.11 h), S_6 (4.00 h) and M_6 (4.14 h). The highest periods found amongst the 37 is several hundreds, and even several thousand, hours. Ideally, we would keep all tidal-constituent frequencies unaffected by the filtering, and filter out all oscillations not related to tidal flow. However, meteorological phenomena of frequencies in the tidal-flow range are common. In Myrhaug (2006), a figure showing the power spectral density of long time series of wind measurements near the ground is given. This figure clearly shows that most of the energy is concentrated in two blocks, one in the micrometeorological range (wind gusts), and one in the macrometeorological range (weathermap fluctuations). The latter is in the range of tidal constituents. Hence, the ideal filtering described above is not possible. In addition, some energy will be lost from the frequency spectrum in the range lower than the cut-off frequency, and not all energy of frequencies higher than the cut-off frequency will be

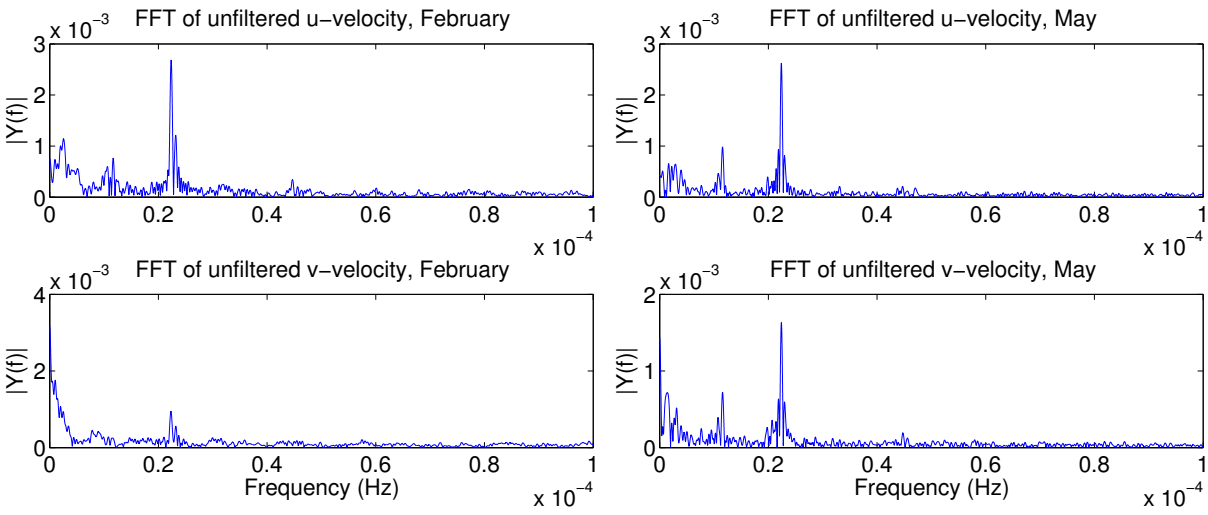

Figure 24: Frequency spectra (discrete Fourier transforms) of the unfiltered velocities, found using a Fast Fourier Transform (FFT) algorithm.

removed by the filtering. This complicates the question of choosing a cut-off frequency further. The cut-off frequency was chosen somewhat arbitrary as $f_c = 4*10^{-5}$ Hz, corresponding to a period of 6.94 h. Visualizations of the filtered velocities showed that this gave smooth time series of tidal flow behavior during periods of low wave activity, although disturbances were clearly present during periods of rough weather conditions. The frequency spectra of the filtered signals are shown in figure 26. This figure illustrates that not all energy of frequencies higher than the cut-off frequency in the signals is removed. Some energy remains up to about $5*10^{-5}$ Hz. The unfiltered and filtered time series are shown together in figure 27.

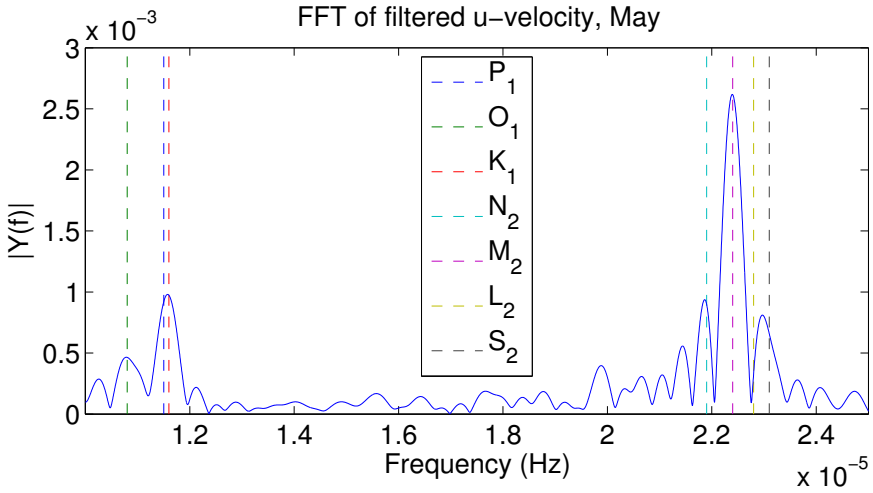

Figure 25: Frequency spectrum (discrete Fourier transform) of the u-velocity during May 2013. The frequencies of the seven tidal constituents described in section 2.3 is marked with stapled lines.

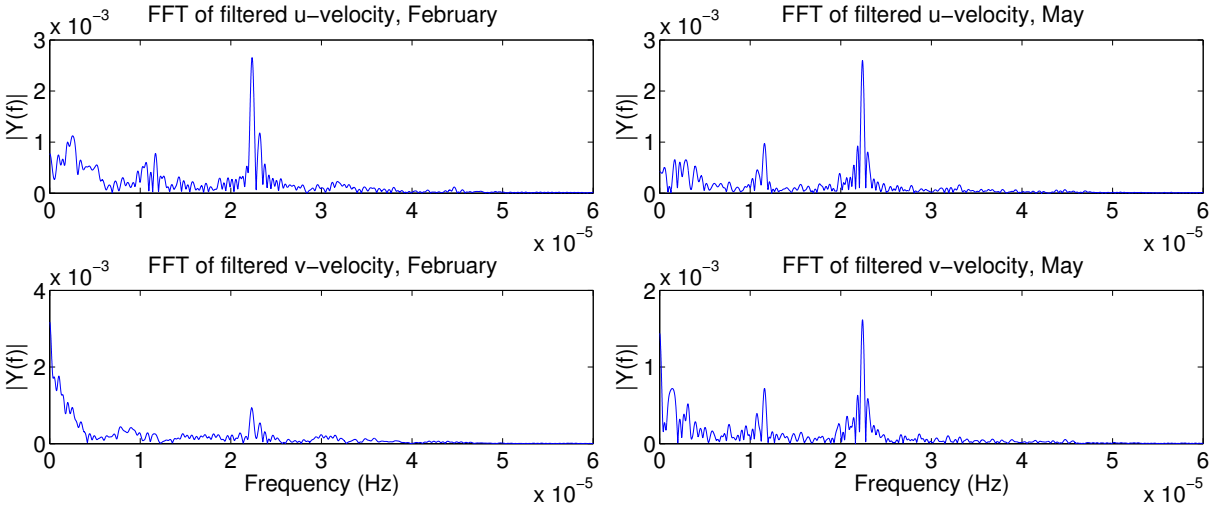

Figure 26: Frequency spectra (discrete Fourier transforms) of the filtered velocities, found using a Fast Fourier Transform (FFT) algorithm.

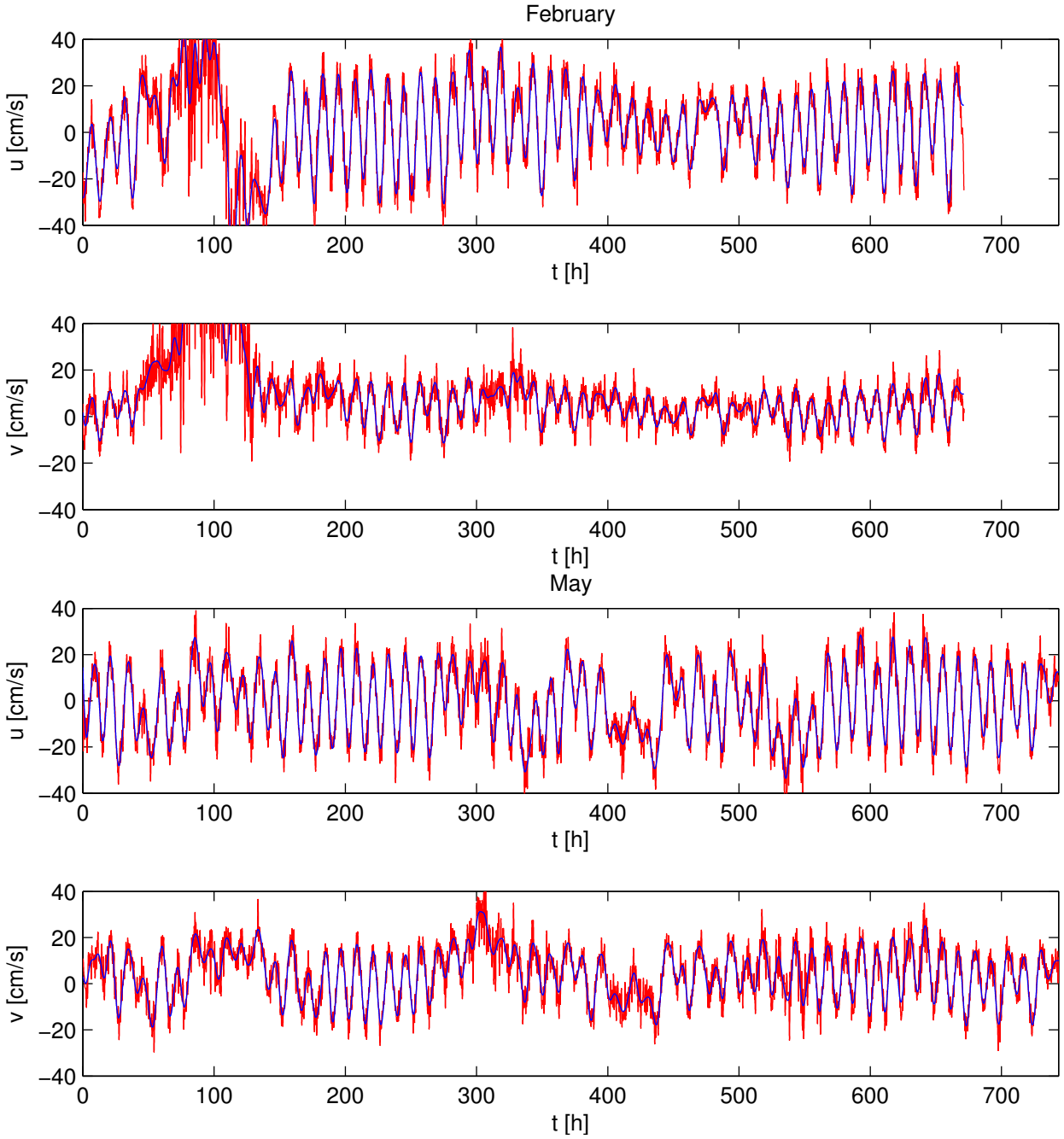

Figure 27: Filtered (blue) and unfiltered (red) velocities in cell 4 (z = 9.15 m) of the field measurements, for February and May of 2013.

6.2 Vertical velocity

In the model described in chapter 5, the boundary layer approximation is considered valid. This means that the horizontal velocities should be much larger than the vertical. The unfiltered time series of the velocity components u, v and w are shown in figures 28 and 29. These figures show that, generally, the horizontal velocities are much larger than the vertical. However, the figures do not show clearly the relative magnitudes of the components in the time intervals when the horizontal components are small. Due to the length of the time series, showing the detailed relative magnitudes of the velocities in these intervals graphically is not practical. Instead, we study some properties of the time series using MATLAB. The results are shown in table 3. The term *much larger than* is not specifically defined. Here, a difference of one order of magnitude (in base 10) is considered much larger. This does not necessarily mean that the boundary layer approximation is valid if the vertical velocity is less than 10 % of the horizontal, but it gives us an impression of the relative magnitudes. In the first row of the table, the fraction of measurements where the vertical velocity w is greater than 10 percent of the horizontal velocity, i.e. where $w > 0.1 \cdot \sqrt{u^2 + v^2}$, is given. The percentages are quite high, spanning from 25.8 % to 77.9 %. It is further of interest to investigate how large the magnitude of the vertical velocity is at the time steps satisfying $w > 0.1 \cdot \sqrt{u^2 + v^2}$. The vertical velocity at these time steps is denoted w_a. The sample averaged absolute value of w_a is shown in the second row of table 3. The velocities are relatively small. The vertical velocity as a possible error source in the modeling cannot be neglected. However, the low mean values of the vertical velocity at time steps where the magnitudes of the vertical and horizontal velocities are comparable makes it reasonable to attempt to model the flow with the present model.

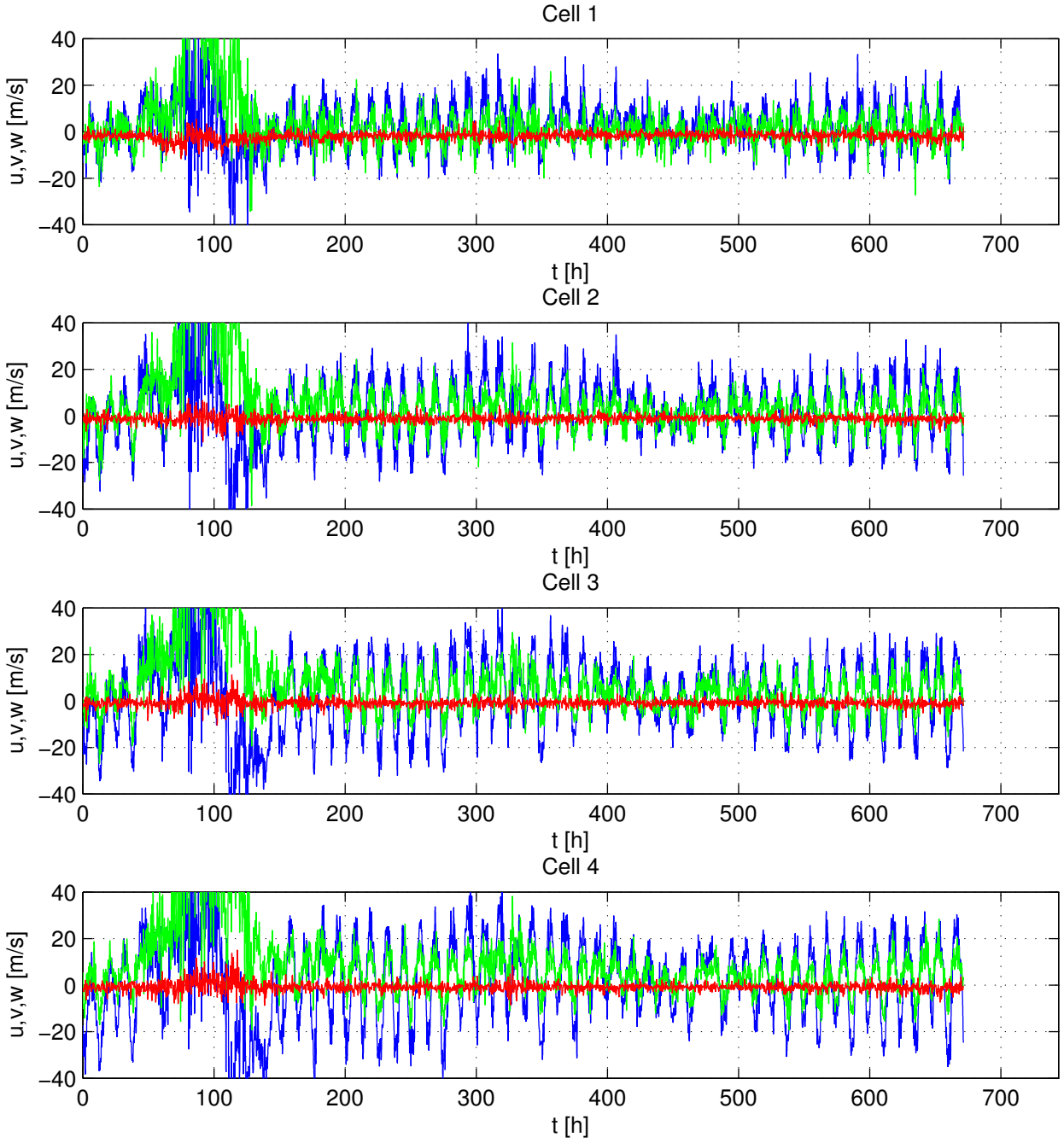

Figure 28: Unfiltered velocities u (blue), v (green) and w (red) of the field measurements, for February 2013. The vertical position of each cell is given in table 3.

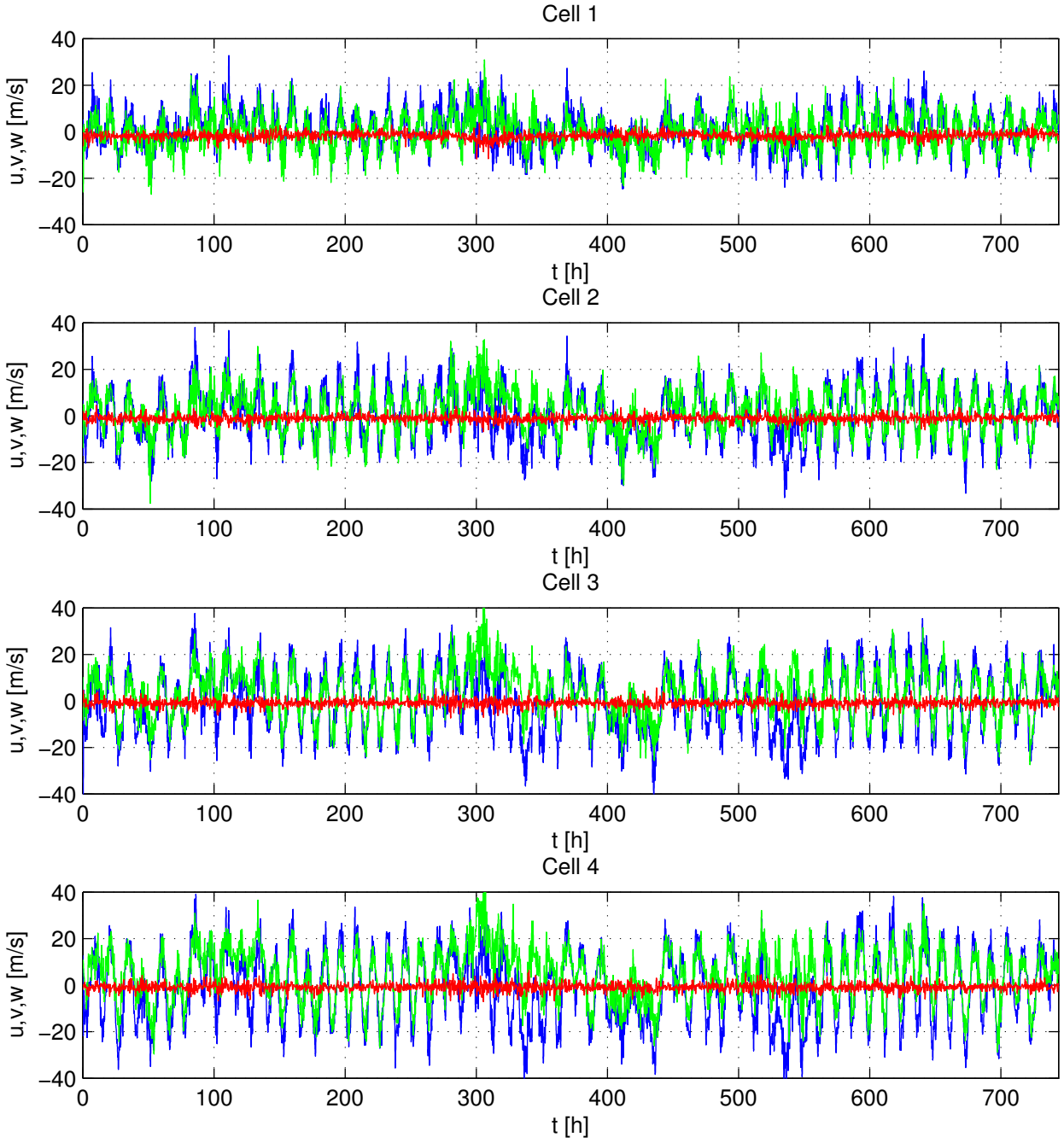

Figure 29: Unfiltered velocities u (blue), v (green) and w (red) of the field measurements, for May 2013. The vertical position of each cell is given in table 3.

	February				**May**			
Cell	**1**	**2**	**3**	**4**	**1**	**2**	**3**	**4**
z [m]	3.15	5.15	7.15	9.15	3.15	5.15	7.15	9.15
$\mathbf{w > 0.1 \cdot \sqrt{u^2 + v^2}}$	61.3 %	38.6 %	30.0 %	25.8 %	77.9 %	46.4 %	33.8 %	30.0 %
$\mathbf{\overline{\lvert w \rvert}}$ **[cm/s]**	1.2	0.6	0.5	0.5	1.6	0.8	0.6	0.6

Table 3: Properties of the vertical velocities in the field data. The fourth row shows the percentage of measurements where the vertical velocity is greater than 10 % of the total horizontal velocity. The fifth row shows the sample averaged absolute values of the velocities corresponding to the first row.

6.3 Residual current

As tides are purely oscillatory flows, any non-zero mean velocity over time is considered a residual current. The residual currents of the splined and filtered field data are shown in table 4. The averaging was done over a finite number of M_2 periods, although the calculated values showed little sensitivity with respect to the cut-off time.

Month	**February**				**May**			
Cell	**1**	**2**	**3**	**4**	**1**	**2**	**3**	**4**
z [m]	3.15	5.15	7.15	9.15	3.15	5.15	7.15	9.15
$\mathbf{\overline{u}}$ **[cm/s]**	3.0	3.0	3.2	3.0	0.8	0.1	-0.6	-1.4
$\mathbf{\overline{v}}$ **[cm/s]**	0.6	2.2	3.5	4.9	0.1	1.7	3.0	4.3

Table 4: Residual currents calculated from the splined and filtered field data.

The residual velocities given in table 4 are shown as vector plots in figure 30. In this figure, a clear tendency appears. The velocity direction deviates clockwise towards the bottom, similar to the surface Ekman layer described in chapter 3. This indicates that the residual current might be wind-induced. If it was driven by e.g. large-scale ocean currents or nonlinear interaction effects of the tides, we would expect a deviation in the opposite (i.e. anti-clockwise) direction, similar to the Ekman bottom layer. The reason for this is that the boundary layer of the field data covers the whole depth (see figure 38), meaning that bottom friction effects are

important through the whole water column. Figure 30 (b) shows the large-scale orientation of the coastline and of the bottom contours at the transducer location. These orientation angles are approximate values found from figure 18. The angles shown in figure 30 (b) are converted to the coordinate system corresponding to magnetic north, used in figure 30 (a). For the February data, the residual current is directed more or less along the coast. For the May data, it is (in the three upper cells) directed seawards at an oblique angle with the coastline. To investigate the hypothesis that the residual currents could be wind-generated, the mean wind velocities for the same time intervals were calculated. The wind measurements used were made at a weather station approximately 15 km south-west of the AWAC transducer. The mean wind velocities are shown in figure 31, with axes corresponding to those of figure 30 (a). In order for figure 31 to be consistent with figure 30, the first 150 h of February were not included in the calculation of the mean wind speed. The mean wind velocities do not correspond with the residual currents in figure 30, suggesting that the hypothesis that the residual currents are mainly wind-generated is erroneous. The residual currents could also be wave induced, but the wind directions indicate that this is not the case either. For the February data, the direction of the current along the coast could indicate that they were longshore currents as described in chapter 3.1.3. However, the direction of the mean wind during February indicates that the current would then be directed towards south-west, instead of north-east. In addition, the transducer is located about 700 m from shore. Longshore currents such as those described in chapter 3.1.3 are located in the surf zone, which is typically much closer to the shore. It might well be that the residual currents are made up by many components resulting from different effects, complicating the task of explaining how they are generated. The generation of the residual currents is not in the scope of this thesis, and will hence not be pursued further. The residual current might be an interesting topic to investigate in further works, however.

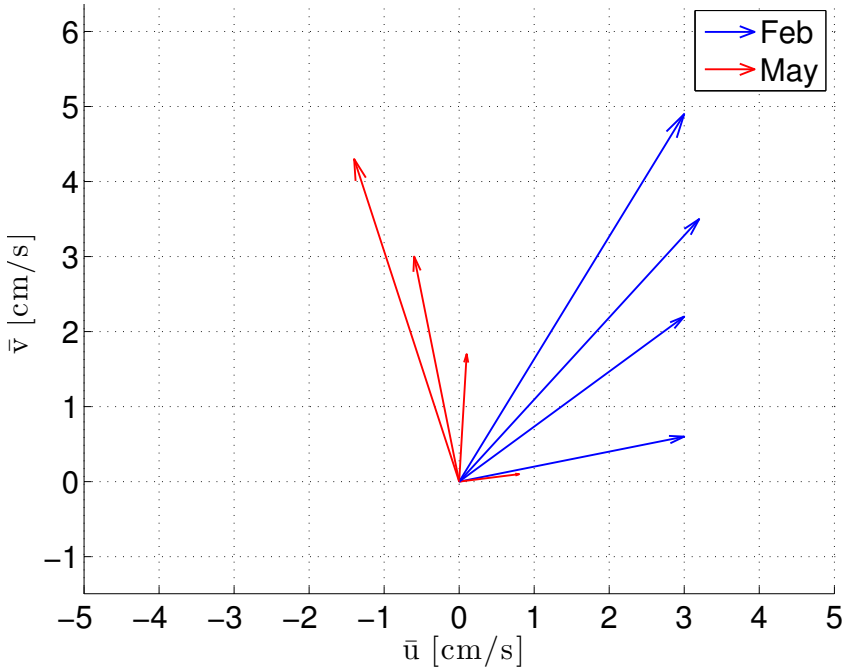

(a)

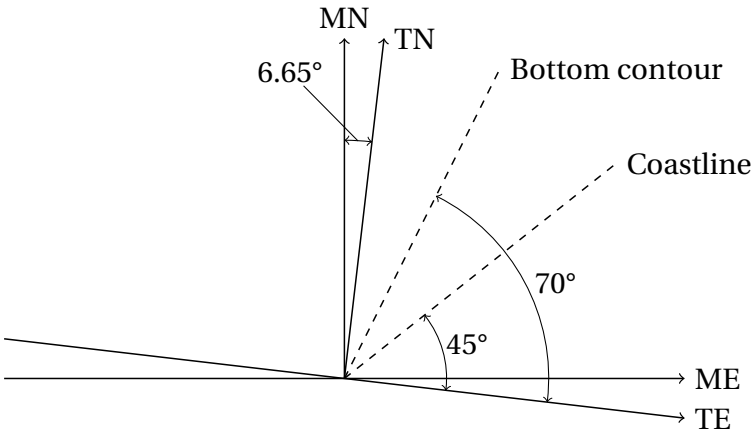

(b)

Figure 30: Vector plot of the residual currents calculated from the splined and filtered field data (a). For both months, the longest vector corresponds to the velocity in cell 4 (closest to the surface), and the velocity is decreasing for the succeeding cells towards the bottom. For February, the first 150 h of the measurements were omitted. Figure (b) indicates the large-scale orientation of the coastline and of the bottom contours at the transducer location. MN, ME, TN and TE denotes magnetic north, magnetic east, true north and true east, respectively. Figure (a) is aligned according to magnetic north.

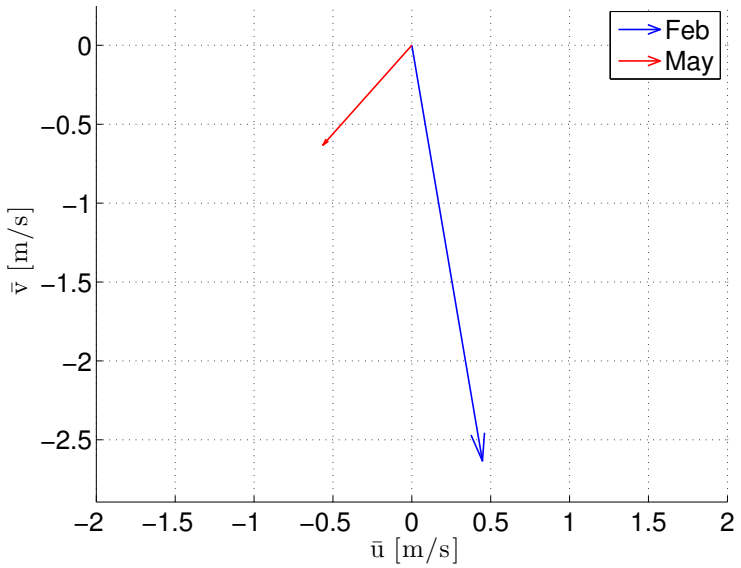

Figure 31: Mean wind velocities during the two months. These are calculated from wind measurements made at a weather station located close to the coast about 15 km south-west of the transducer measuring current and waves. The axes are aligned according to magnetic north, to obtain consistency with figure 30.

7 Results and discussion

7.1 Previous work

The model was used in a project work written during the fall of 2014, leading up to the present work. Field data from King et al. (1985) of tidal flow over a flat bottom at a depth of 120 m was used to study effects of bottom roughness and total water depth. The results and conclusions of this work are presented in appendix C, as the work is considered relevant for the present thesis. In addition, a verification of the model's applicability for modeling tidal flow in the given conditions is given in appendix C. The flow modeled in the project work is less complex than the field data presented in chapter 6. This is because the data from King et al. (1985) are measured in deep-water conditions, where the flow is generally less complex than in shallow water, and because the data are averaged over several tidal periods, giving averaged data for one period.

7.2 Model setup

The model was run with the splined and filtered field data. The data from cell 4, which has its center 9.15 m above the bottom, was chosen as the input data for the model. This is the measuring point closest to the surface that is submerged during low tide. The choice of this cell was made in order to minimize the effect of friction due to the seabed. When the model is applied to deep-water flows, the vertical position of the input data is chosen where the current is as close to geostrophic as possible, i.e. somewhere between the bottom boundary layer and the surface boundary layer induced by wind and waves. In shallow water, however, the bottom boundary layer covers the whole water column, complicating the choice. Since the frequencies corresponding to those of wind waves in the input signal used in this work is removed by time averaging and because the signal is passed through a lowpass filter, it should be reasonable to use a vertical position relatively close to the surface. The water depth was set to 12.9 m, as this was found to be the mean water depth from the surface elevation data.

The residual currents present in the field data (see chapter 6.3) were not subtracted before running the model. In hindsight, subtracting the residual currents would be more con-

sistent with the intention of modeling pure tidal flow. However, a test run was performed, where the residual currents were subtracted before running the model and then added to the results. The resulting velocities were compared to the velocities obtained without subtracting the residual current. The mean absolute values of the deviation between the two runs were 0.3 cm/s for the u component and 0.2 cm/s for the v component. Hence, the tidal component and the residual component of the flow is simply superposed (i.e. interaction effects are negligible), at least in the model. Not subtracting residual currents from the input velocities forcing the flow in the model should therefore not affect the results. Obviously, the velocities used for comparison with model results correspond to those used for forcing of the flow, i.e. the residual currents are not subtracted.

7.3 Choice of bottom roughness

As the bottom conditions for the field data are quite complex (see chapter 6), the choice of bottom roughness parameter z_0 is not obvious. To find the value giving the best agreement between the model results and the measured velocities, several simulations of both the February and May data were performed. z_0 was varied between 0.0006 cm and 0.050 cm. The results were evaluated both by visualization and by calculating the squared error of the results, defined by

$$SE = \frac{\sum_{i=1}^{n} (x_i - y_i)^2}{n} \tag{7.1}$$

where x_i and y_i are the model results and the field data, respectively. By visualization, the lower values of z_0 proved to give better agreement between the field data and the model results than the higher values. The trend for the higher values was that the time series for both the u and v component were phase shifted, in opposite directions. This resulted in broader tidal ellipses, very different from the back-and-forth movement of the field data. This is illustrated in the figures in appendix B.1, where the velocities over the whole months, for both February and May, are plotted in the horizontal plane. These figures show that the tidal current in the field data oscillates more or less along the coastline. They further illustrate that this behavior is replicated by the model runs with the smaller roughness values, but that the runs of higher z_0 values display a very different behavior. The velocities of these runs

form broad ellipses with main axis rotated clockwise relative to the direction of the current in the field data. The clockwise rotation of the main axis for increasing bottom roughness corresponds with the conclusions of the pre-master project work presented in appendix C.

Deciding which one of the lower bottom roughness values gave the best result visually, proved difficult. Therefore, the calculated squared errors were useful. The squared error at each cell for the different roughnesses is shown in figures 32 and 33. For the February data, the agreement is best with z_0 = 0.0006 cm, i.e. the lowest value of z_0. The exception is the u component of the velocity at cell 1, which is modeled with decreasing error for increasing roughness. The results for May are quite similar. Clearly, z_0 = 0.0008 cm gives the best result for the v component of the velocity. For the u component, however, the results are not as clear. z_0 = 0.0008 cm gives the best result in the two upper cells, but closer to the bottom the error decreases with increasing z_0, as for the lowest cell of the February simulations. The higher z_0 values give more consistent errors throughout the water column. The accuracy difference between the runs with z_0 = 0.0006 cm and z_0 = 0.0008 cm is very small, however. The general conclusion based on both the calculated squared errors and visualization is that the best result is obtained with z_0 = 0.0006 cm. The full time series of the model results for February and May 2013 with this bottom roughness is plotted together with the field data in figures 34 to 37. Time series from some of the runs with other roughnesses are given in appendix A, for comparison. The results for z_0 = 0.0006 cm are good in cell 4 and quite good in cell 3, for both months. In the two lower cells, the reproduction of the oscillations are good, but the magnitudes of the velocities are overestimated by the model. In other words, the model is not able to replicate the damping near the bottom well. One possible reason for this is the seaweed growing on the seabed, which might damp the flow differently than e.g. sand or gravel. However, the results must be said to be fairly good, the simplicity and efficiency of the model taken into account. Unless otherwise stated, all results presented in the following are from the model runs with bottom roughness z_0 = 0.0006 cm.

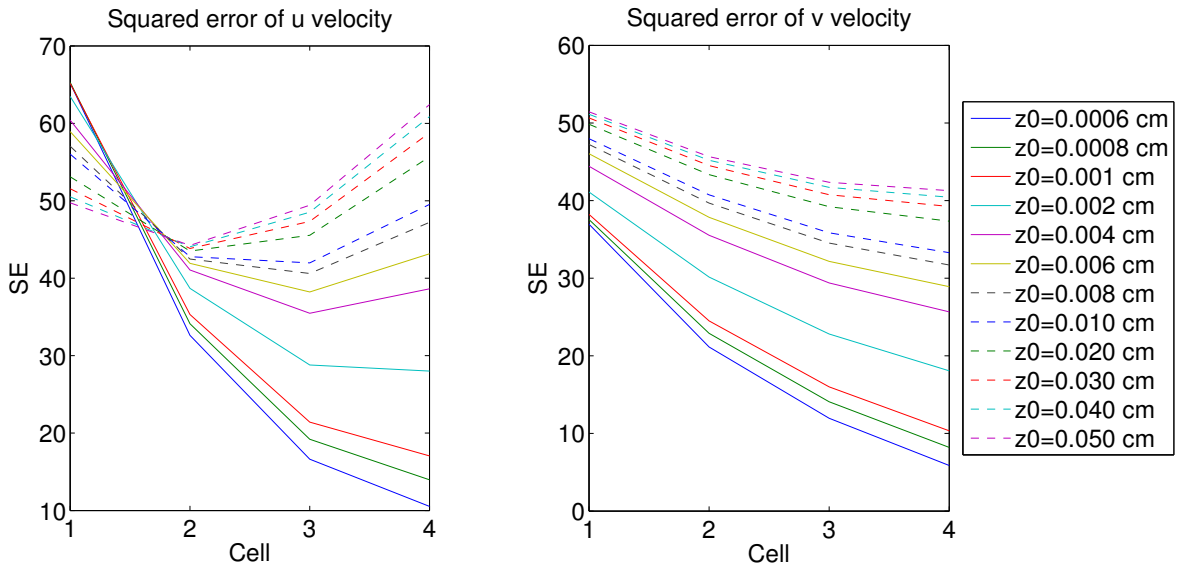

(a) *(b)*

Figure 32: Squared error of the model results for February, for different values of the bottom roughness z_0. Figures (a) and (b) show the error of the u and v component of the velocity, respectively.

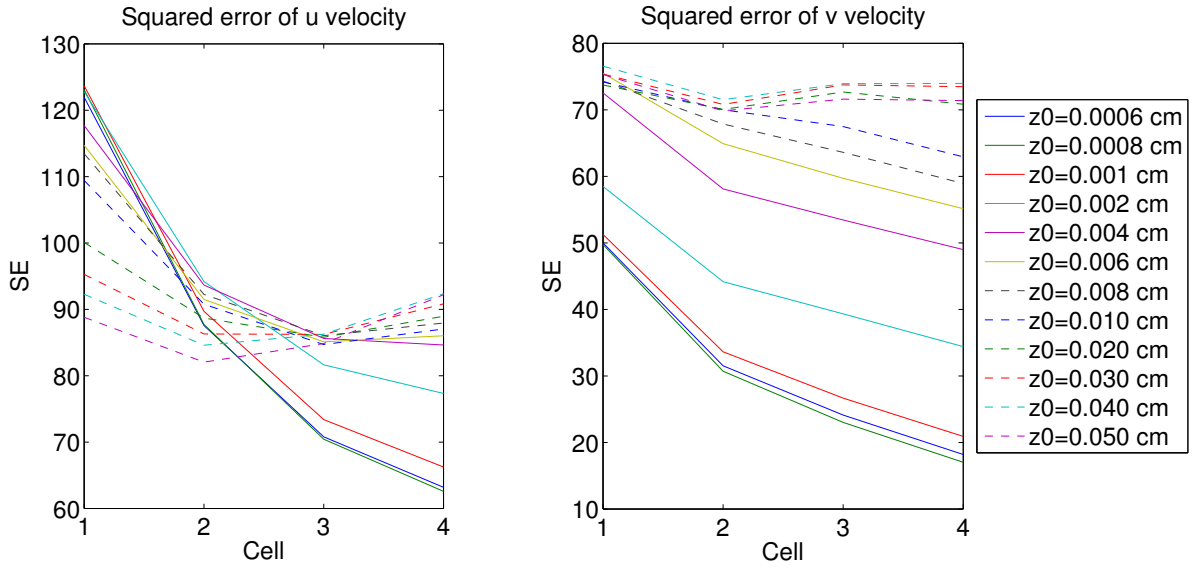

(a) *(b)*

Figure 33: Squared error of the model results for May, for different values of the bottom roughness z_0. Figures (a) and (b) show the error of the u and v component of the velocity, respectively.

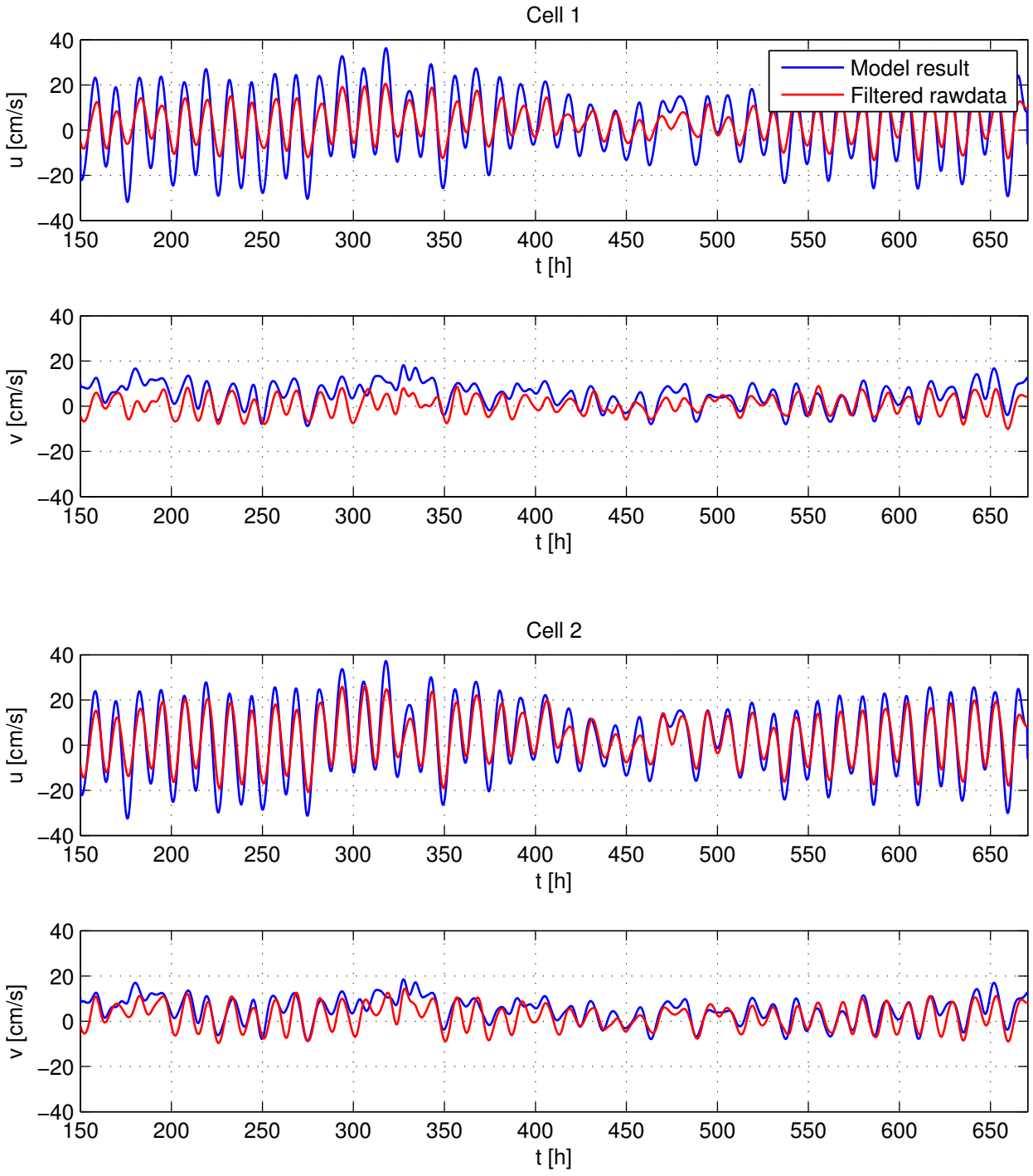

Figure 34: Model results and field data for February 2013, cell 1 and 2, with bottom roughness $z_0 = 0.0006cm$.

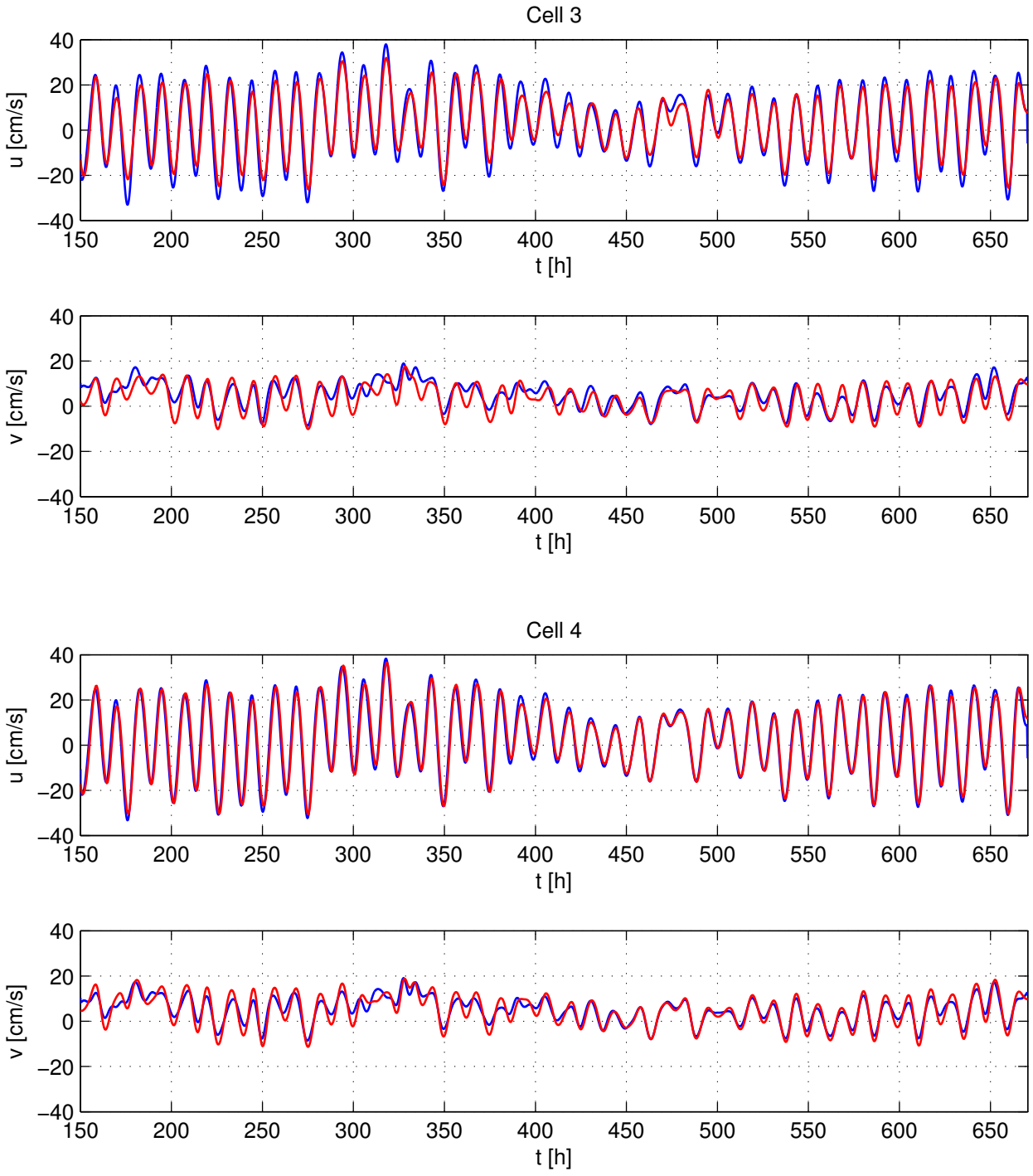

Figure 35: Model results and field data for February 2013, cell 3 and 4, with bottom roughness $z_0 = 0.0006cm$.

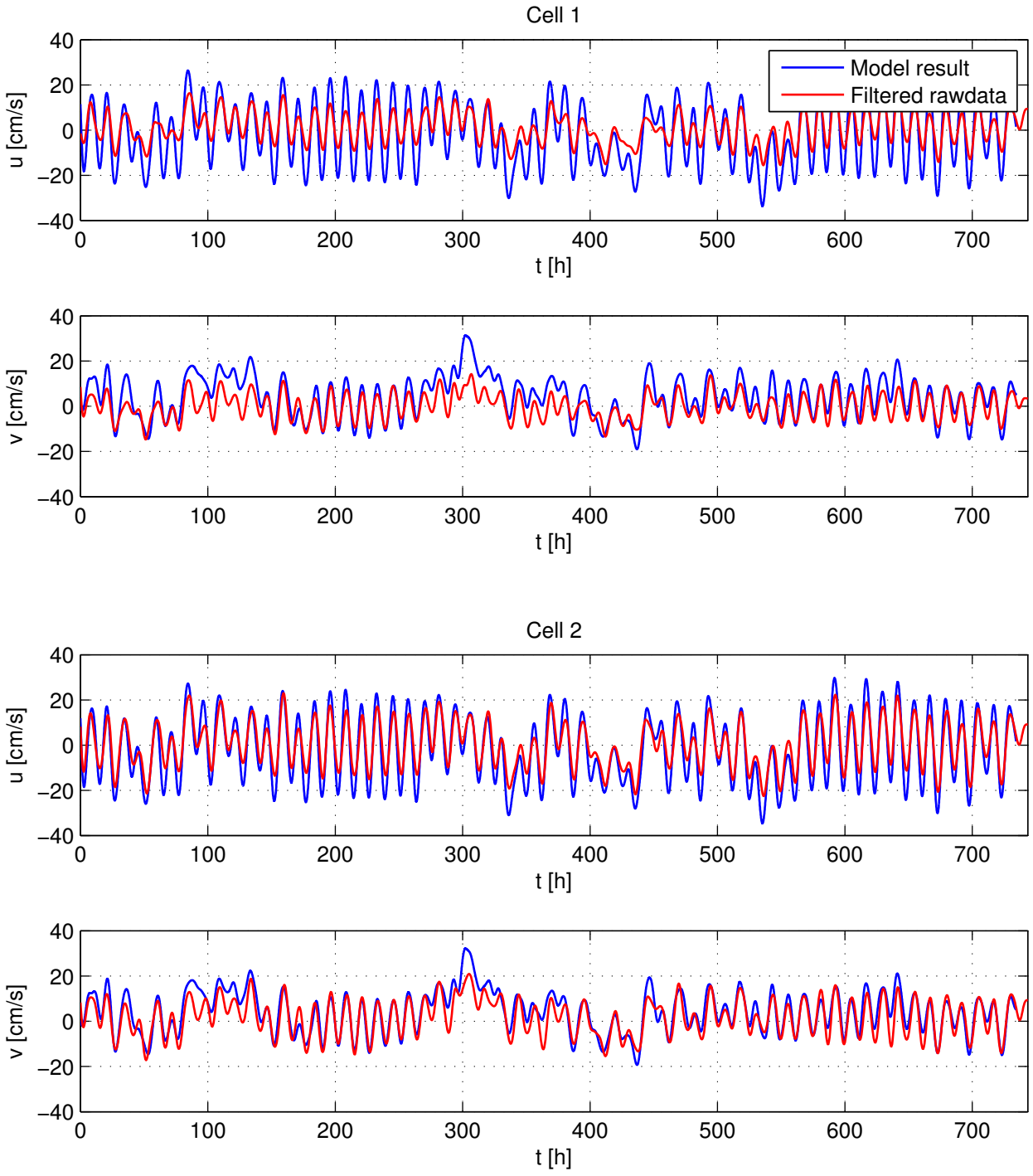

Figure 36: Model results and field data for May 2013, cell 1 and 2, with bottom roughness z_0 = 0.0006cm.

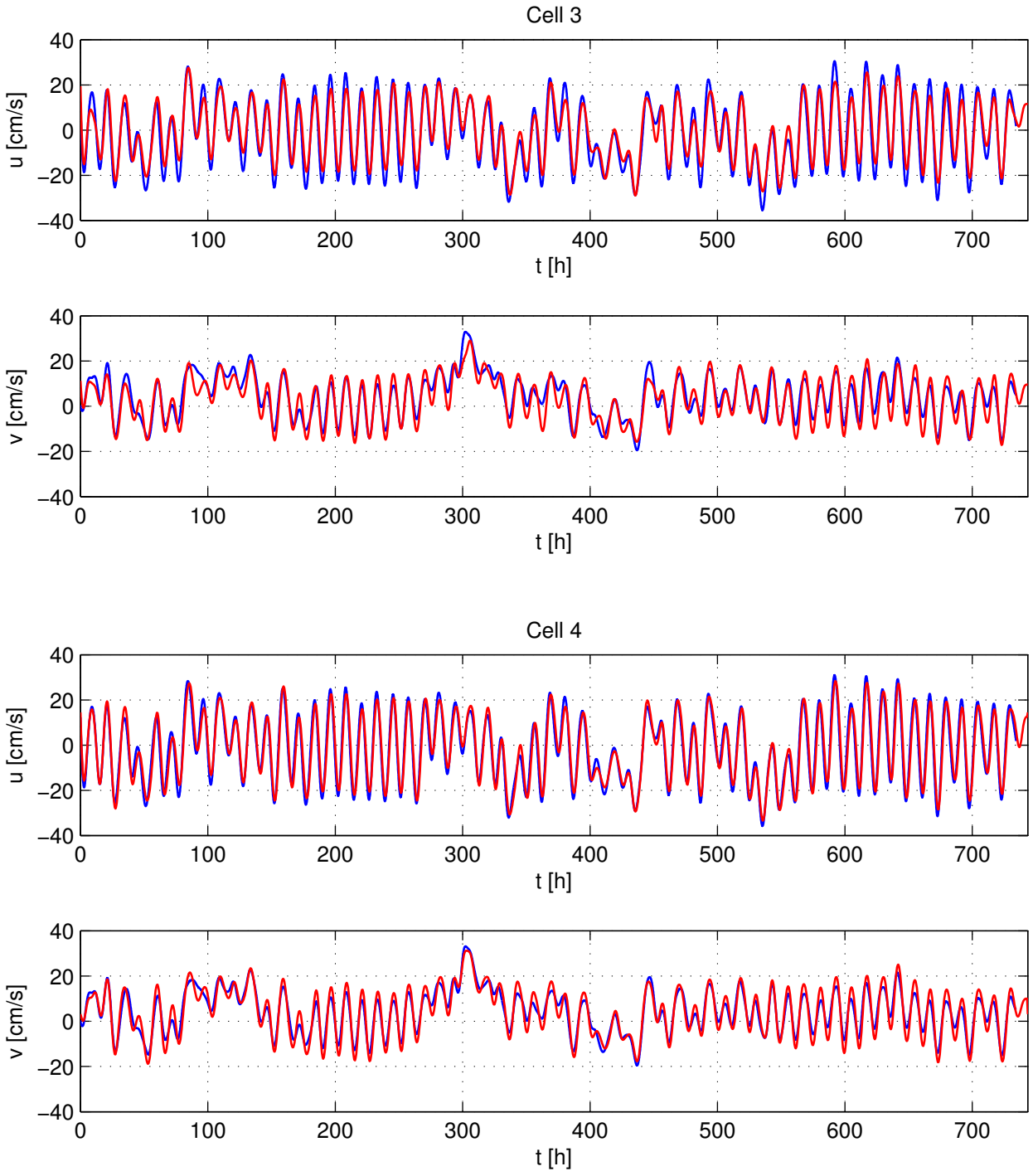

Figure 37: Model results and field data for May 2013, cell 3 and 4, with bottom roughness z_0 = 0.0006cm.

7.4 Vertical current speed profiles

Soulsby (1990) presents an empirical formula for the tidal current speed through the water column:

$$U(z) = \left(\frac{z}{0.32h}\right)^{1/7} \overline{U} \quad \text{for 0 < z < 0.5h} \tag{7.2a}$$

$$U(z) = 1.07\overline{U} \quad \text{for 0.5h < z < h,} \tag{7.2b}$$

where $U = \sqrt{u^2 + v^2}$ is the current speed, h is the water depth and $\overline{U}$ is the depth averaged current speed given by

$$\overline{U} = \frac{1}{h}\int_0^h U(z). \tag{7.3}$$

The present model results and field data are compared to this formula in figure 38 (b). Note that, in figure 38, U denotes the current speed averaged over the month, while $\overline{U}$ denotes U averaged over the water column. $\overline{U}$ was calculated separately for the model results and the field data. Soulsby (1997) presents a procedure for calculating $\overline{U}$ from measurements. The current speed at the bottom is taken to be zero, and the speed at the surface is assumed equal to the speed at the highest measuring point. The integral in equation (7.3) is approximated by the trapezoidal rule for non-uniform grids, which under the present assumptions is given by

$$\begin{aligned}\overline{U} = \frac{0.5}{h}\Big(&U_1 z_1 + (U_1 + U_2)(z_2 - z_1) + (U_2 + U_3)(z_3 - z_2) + \ldots + (U_{n-1} + U_n)(z_n - z_{n-1}) \\ &+ 2U_n(h - z_n)\Big).\end{aligned} \tag{7.4}$$

The grid used in the present work has 100 points and is non-uniform with increasing spacing towards the surface. This should give a calculated $\overline{U}$ of high accuracy for the model results, since the gradient of the modeled current speed decreases rapidly towards the surface. For the field data, however, the number of measuring points is too low, and the lowest point is too far from the bottom, for the calculated $\overline{U}$ to be accurate. According to Soulsby (1997), we should have at least six measuring points, and the lowest one should not be higher than 0.2 m above the bottom, for equation (7.4) to give a good approximation of $\overline{U}$. As we only have four measuring points, and the lowest is located 3.15 m above the bottom, these requirements are not fulfilled. Judging by the form of the current speed profiles for the field data through the

four measuring points (see figure 38 (a)), taking the surface current speed to be equal to the current in the highest measuring point is not a good approximation. Instead, the relationship between the current speed in the two upper measuring points and the current speed at the surface was taken to be linear. This is expected to give a contribution to $\overline{U}$ that is too high in the upper part of the water column. The lack of measuring points close to the bottom should give a contribution in the near-bottom area that is lower than the real value. In total, the calculated value of $\overline{U}$ for the field data is related to a high degree of uncertainty, but expectedly not too high for the field data graphs in figure 38 (b) to give a useful indication of the non-dimensionalized current profiles.

The dimensional current speed profiles shown in figure 38 (a) clearly show that the model is not able to replicate the boundary layer in the real flow. The damping of the flow towards the bottom is much greater in the field measurements than in the model results. The mean speed of the field data and the results are equal at approximately z = 9 m, i.e. close to the center of cell 4, which is what we would expect after studying the time series in figures 34 to 37. Figure 38 (b) shows that the speed profiles of the model results are closer to the empirical formula (7.2) by Soulsby (1990) than the measured speeds are. Although the damping towards the bottom predicted by the formula is also stronger than in the model results, the profile shapes of the model results are remarkably more similar to the formula profile than those of the field data. In figure 39, current speed profiles of the present model with different bottom roughnesses are shown. The graphs corresponding to the model runs with z_0 = 0.050 cm fits very good to the formula graph. However, as we saw in section 7.3, this roughness did not give time series or tidal ellipses corresponding well with the field data.

The empirical formula (7.2) is compared graphically to various field measurements in Soulsby (1990). The conditions under which these measurements are taken differ strongly. The most relevant condition here is the depth, which ranges from 3.5 m to 167 m in the measurements shown in Soulsby (1990). Hence, shallow-water conditions are covered. Of the 85 data points that are compared to formula (7.2) in Soulsby (1990), 82 points are within 10 percent of the formula. Further, none of the data-points indicate a boundary layer covering the whole water depth, like the field data used in this work do. This suggests that the poor agreement of our field data from the coast of the Hebrides with the formula is not exclusively caused by the shallow-water conditions. Parameters like the magnitude of $\overline{U}$ and the bottom

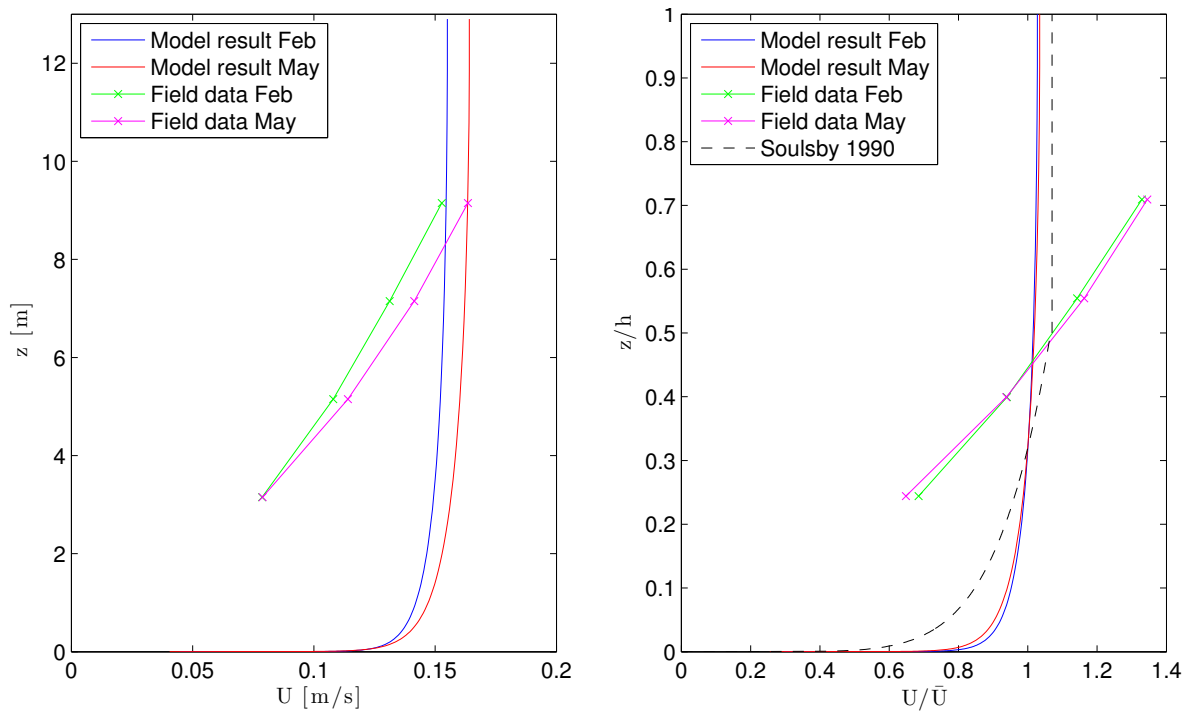

(a) *(b)*

Figure 38: Mean current speed profiles (a) and comparison of mean current speed profiles with empirical formula by Soulsby (1990) (b). The model result graphs are for bottom roughness z_0 = 0.0006 cm. Here, U denotes the current speed averaged over the month, while $\overline{U}$ denotes U averaged over the water column. The depth-averaged mean current speed $\overline{U}$ used in (b) was calculated separately for the field data and the model results.

conditions, or coupled effects of these with the depth, are likely to contribute to this difference. The most interesting thing to notice from the above considerations is that, although the present model is not able to replicate the boundary layer in the field measurements from the Hebrides, it predicts a speed profile that is close to the more general tidal boundary layer known from deep water, but also for shallow water under the right conditions. Hence, the model might be able to replicate shallow-water tidal flow through the whole water column, under less complex conditions than the present. However, this remains to be verified.

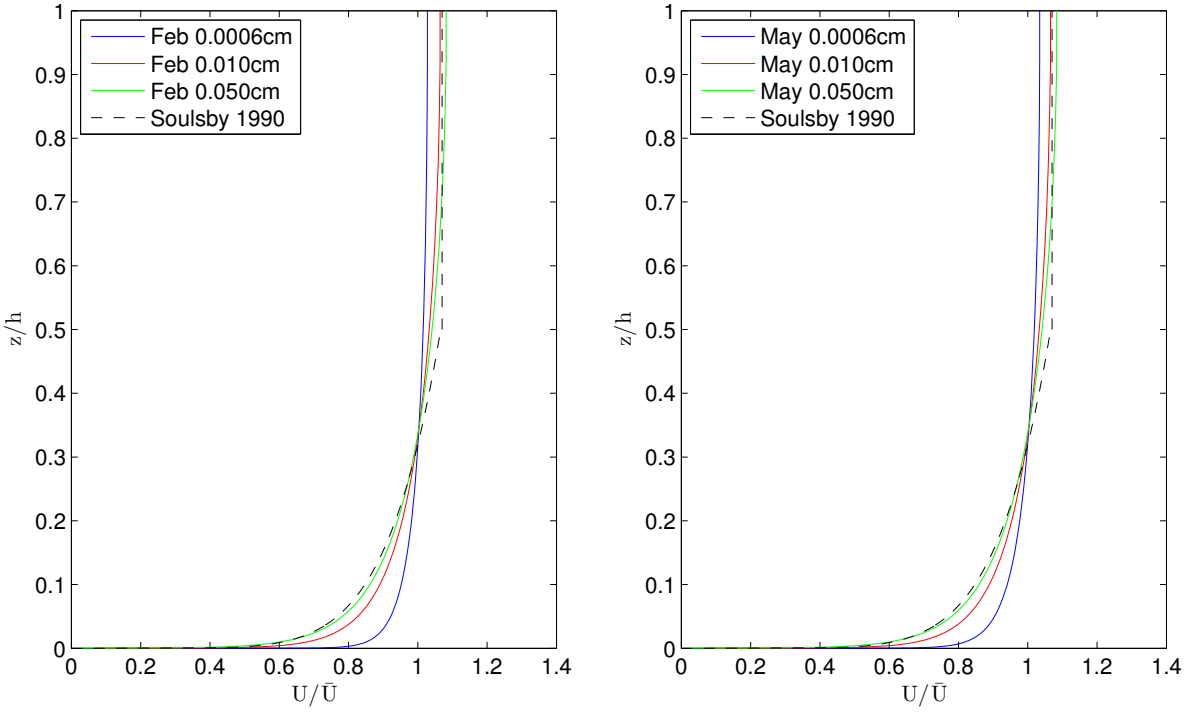

(a) *(b)*

Figure 39: Comparison of mean current speed profiles from the model for different bottom roughnesses with empirical formula by Soulsby (1990). Here, U denotes the current speed averaged over the month, while $\overline{U}$ denotes U averaged over the water column.

7.5 Flow regime

Effects of bottom roughness and the possible flow regimes of turbulent flows are described in section 4.4. The mean and maximum friction velocities, and the corresponding values of Rr, over the month are calculated for $z_0 = 0.0006$ cm and $z_0 = 0.050$ cm for both February and May. The friction velocity was found using the familiar formula for the logarithmic velocity profile (see e.g. Soulsby, 1997):

$$U(z) = \frac{u_*}{\kappa} \ln\left(\frac{z}{z_0}\right), \tag{7.5}$$

which generally is a quite good approximation of the boundary layer in the lower part of the water column (except for the area very close to the bottom, between the roughness elements) for stable flow. κ is the von Karman's constant, which was taken as the standard value $\kappa = 0.4$. The equation was evaluated at the node closest to the bottom. The calculated values of u_* and Rr are given in table 5. Table 5 shows that the flow in the model runs with bottom

		Mean			**Maximum**		
Month	z_0 **[cm]**	u_* **[m/s]**	**Rr [-]**	**Regime**	u_* **[m/s]**	**Rr [-]**	**Regime**
Feb	0.0006	0.0064	0.039	Smooth	0.0161	0.097	Smooth
May	0.0006	0.0068	0.041	Smooth	0.0146	0.088	Smooth
Feb	0.0500	0.0063	3.190	Rough	0.0134	6.690	Rough
May	0.0500	0.0068	3.415	Rough	0.0145	7.250	Rough

Table 5: Calculated friction velocities, Reynolds roughness numbers and corresponding flow regimes for different simulations.

roughness $z_0 = 0.0006$ cm, which gave the best agreement with the velocity time series and tidal ellipses of the field data, is hydrodynamically smooth. This is as expected, because the roughness is extremely small. For comparison, Holmedal and Myrhaug (2013) found that a bottom roughness of $z_0 = 0.1$ cm gave the best agreement with measurements made over a flat bottom of silty sand, with small ripples. The flow modeled with $z_0 = 0.050$ cm, which gave a mean current speed profile fitting well with various field measurements, is hydrodynamically rough. This result supports the findings in section 7.4, which suggest that $z_0 = 0.050$ cm gives a more realistic boundary layer.

7.6 Effect of wind and wave conditions

In the field data, each current sample is the average value of several measurements taken over a period of 60 seconds, to remove wind wave oscillations. In addition, the cut-off frequency used in the filtering is much lower than the frequencies of orbital wind wave motions. Still, effects of wind and wave conditions might be present in the filtered velocities, causing deviations between the modeled and the measured time series. Possible effects are wave-current interaction, wave-generated currents and wind-induced currents. These effects are described in chapter 3. To evaluate whether or not effects of wind and waves cause errors in the modeling, we compare model results from time intervals of low and high wave activity, respectively. Hours 540-590 of February and 180-230 of May were chosen as the time intervals of low wave activity, and hours 310-360 of February and 290-340 of May as those of high wave activity (see figures 22 and 23). Out of the several time intervals of low or high wave activity, these were chosen because the difference in tidal range is relatively low (see figure 21). The model results and the filtered field data from these time intervals are shown in figures 40 to 43. Clearly, rough weather affect the velocities. In the two time series of low wave activity, especially in the one from May, the velocity series are close to sinusoidal. This indicates that the flow is close to pure tidal flow. In the time series of higher wave activity, however, the signals are more irregular. In the two upper cells, closest to the surface, the agreement between the model and the field data are approximately equally good in all the intervals, although the agreement is slightly better in the low-wave period of February than in the other three. In cell 1 and 2, the difference is more noticeable. In the two February series, the best agreement is found in the small-wave interval, especially for the v component. In the May series, the results for the u component is best in the interval of high wave activity, while the v component result is better in the interval of low wave activity. These results indicate that the model result may be slightly better in periods of small wave activity. However, we cannot conclude that effects of wind and waves are significant contributions to the deviations between the results and the measurements. For this, the above results are too ambiguous.

To further investigate the effect of weather and wave conditions, we study the turbulent kinetic energy and the shear stress through the water column during the same periods. Vertical profiles of the mean turbulent kinetic energy $\bar{k}$ during the periods defined above are

given in figure 44. In subfigures (b) and (d), k is averaged over the whole periods. More precisely, the averaging was done over 49.6 hours, or four M_2 periods, instead of the 50 h periods given above. This was done to avoid inconsistencies due to choice of starting point in the tidal cycle. These two subfigures indicate that the turbulent kinetic energy is significantly higher during periods of rough weather. However, a further analysis, shown in subfigures (a) and (c), where the averaging is done over shorter time intervals (one M_2 period), reveals that the matter is more complex. These figures show that, for both months, one of the four M_2 periods contributes with most of the excessive kinetic energy. Still, the fact that the velocity series are quite irregular during the high wave intervals makes it more appropriate to use an interval of longer duration for the averaging.

In figure 45, shear stress profiles from periods of low and high wave activity are shown. Profiles are shown for each half hour of one M_2 period. Only the first M_2 period of each of the low and high wave intervals defined above are shown, as these proved to be good representations of the whole 50 hour periods. The shear stress is calculated as

$$\tau(z) = \rho(\nu + \nu_T)\frac{\partial U(z)}{\partial z}, \tag{7.6}$$

where U is the current speed given by $U(z) = \sqrt{u^2(z) + v^2(z)}$. Figure 45 indicates that the shear stress increases through the whole water column during rough weather, relative to periods of calm weather.

It should be emphasized that the profiles of turbulent kinetic energy in figure 44 and of shear stress in figure 45 is calculated from the modeled flow. As the input for the forcing function is simply the filtered velocities at a height of 9.15 m above the seabed, the model drive the flow as a current of shifting directions and varying magnitudes. Effects of e.g. wave-current interaction is not taken into account in the model. This means that if wave-current interaction was an issue, it would not be evident in the profiles of $\bar{k}$ and τ. The only possible weather-related effect that could be found in these plots is the direct effect of increased turbulence and shear stress due to increased velocities. In figure 46, the mean current speed profiles of the four periods of low and high wave activity, respectively, are shown. This figure clearly shows that the current speed is significantly increased during the periods of high wave activity. The increase in turbulence and shear stress in these periods is therefore most likely a direct effect of increased velocities.

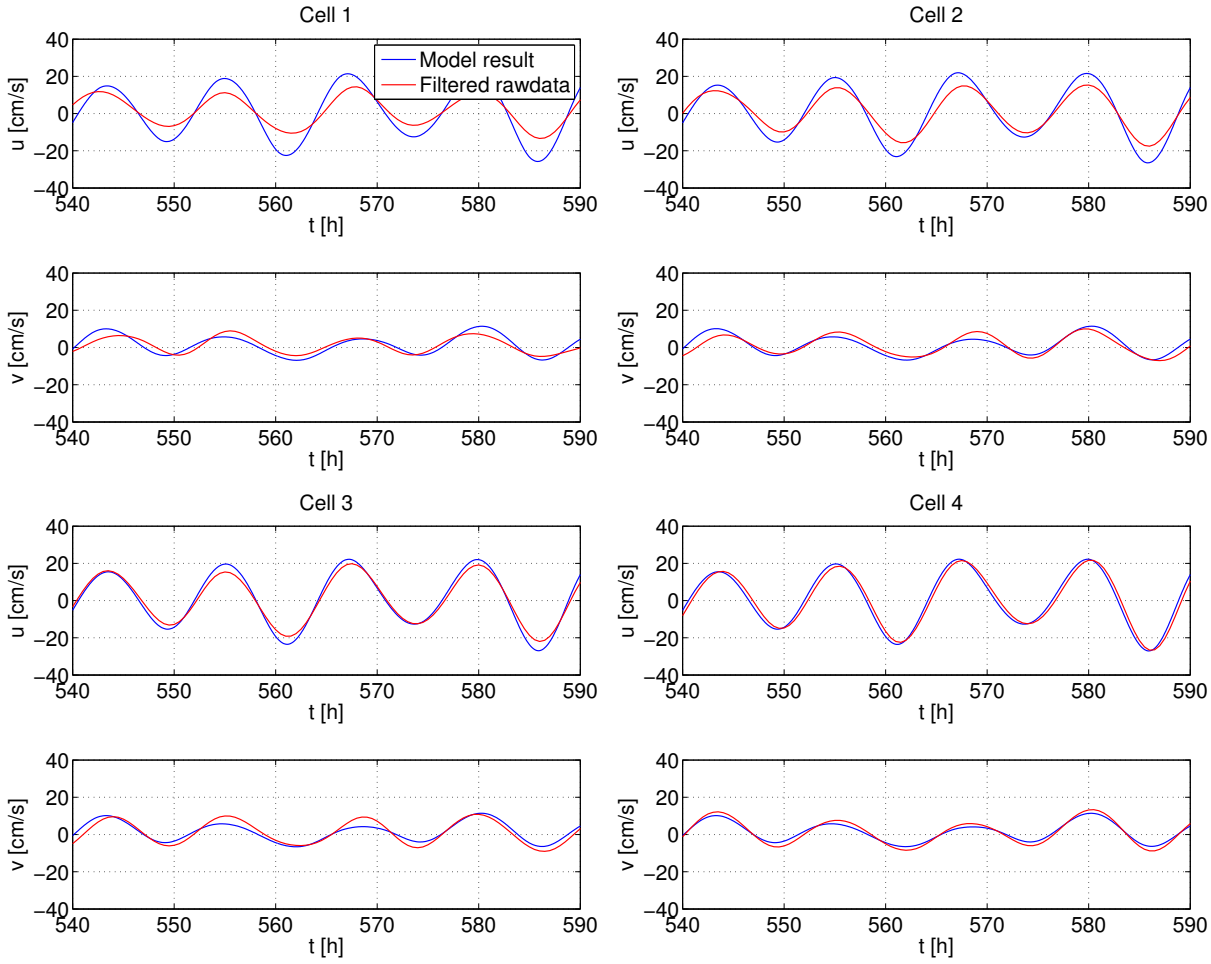

Figure 40: Model results and field data velocities in the time interval from 540 h to 590 h of February 2013. During this time interval, the wave activity was low.

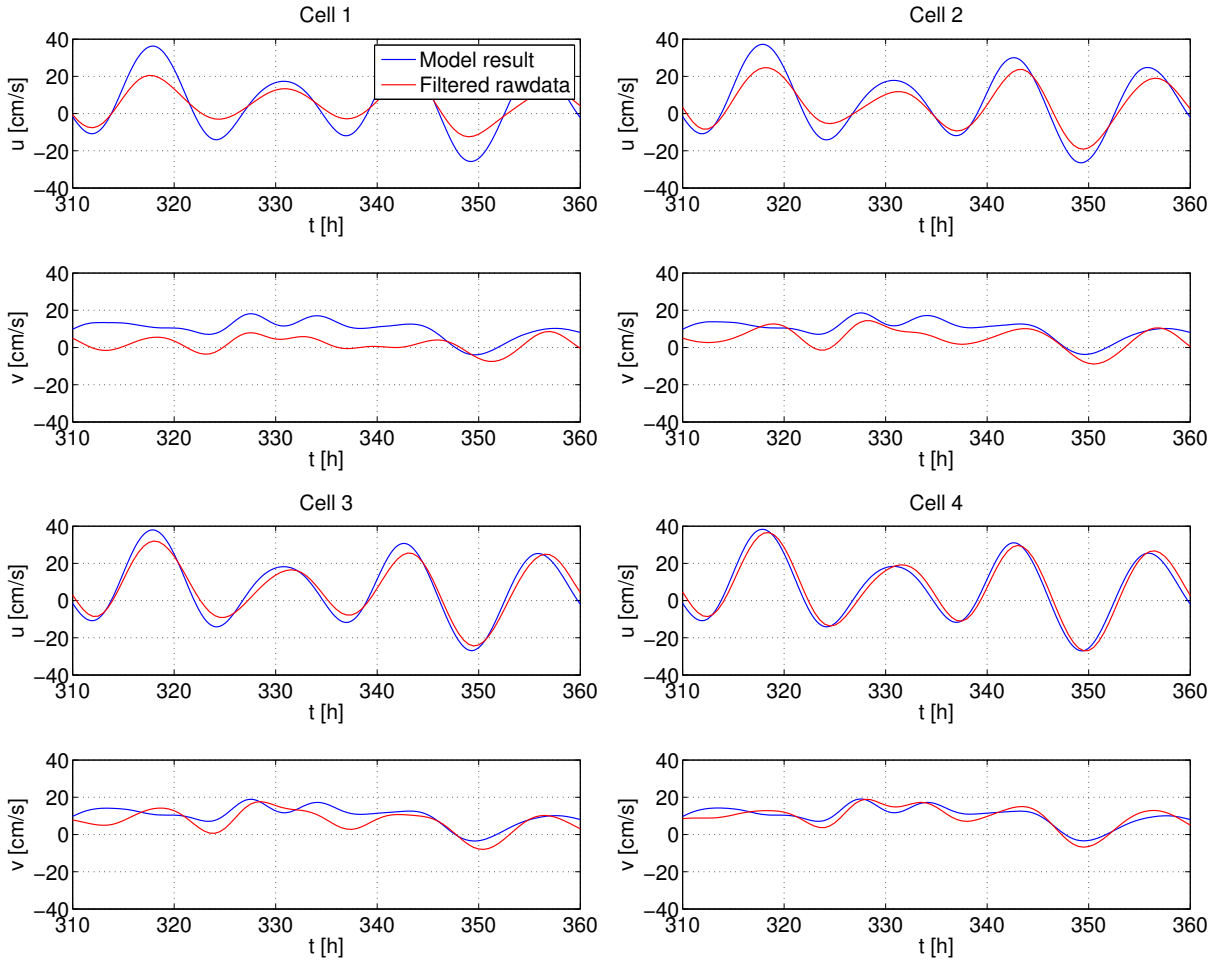

Figure 41: Model results and field data velocities in the time interval from 310 h to 360 h of February 2013. During this time interval, the wave activity was high.

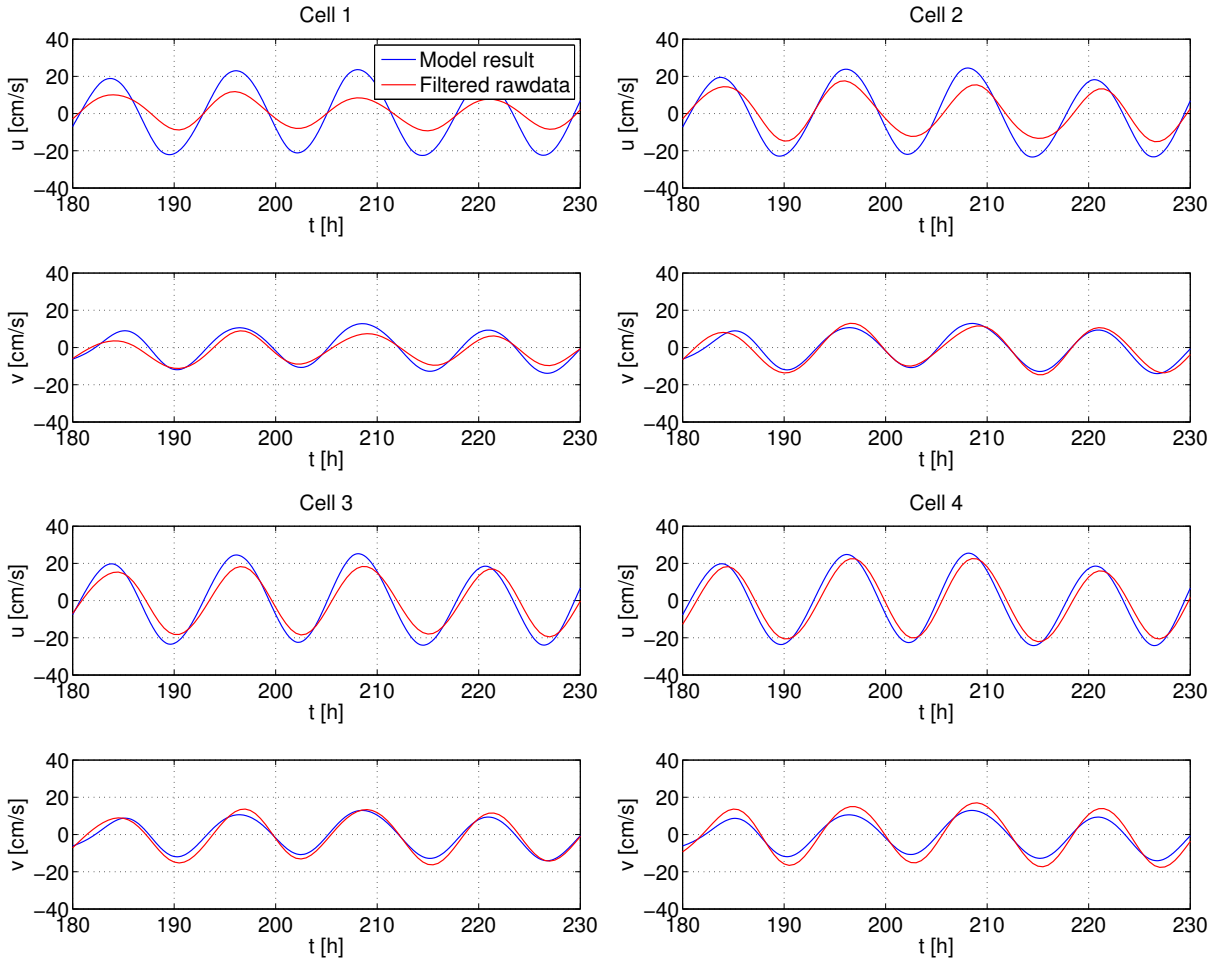

Figure 42: Model results and field data velocities in the time interval from 180 h to 230 h of May 2013. During this time interval, the wave activity was low.

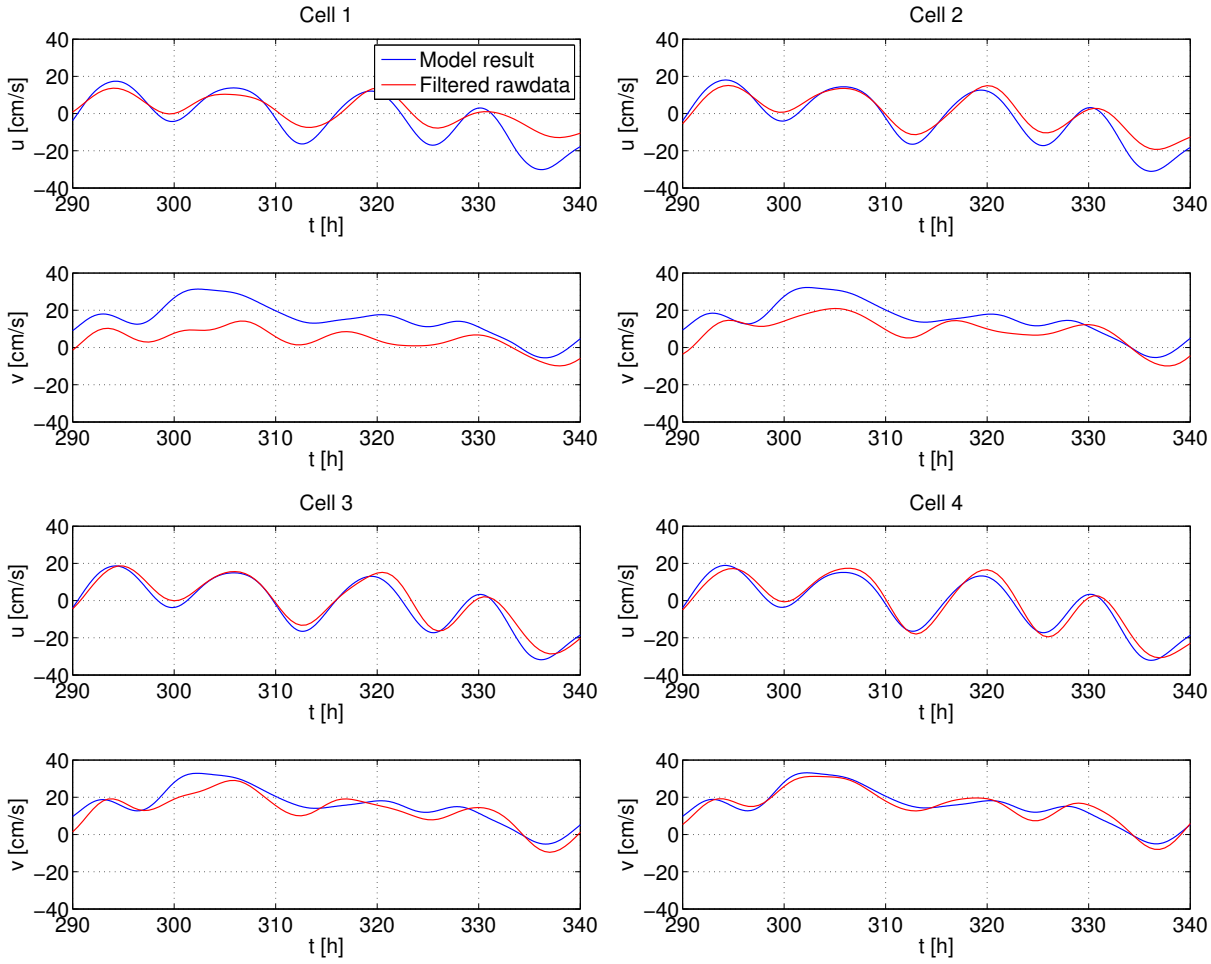

Figure 43: Model results and field data velocities in the time interval from 290 h to 340 h of May 2013. During this time interval, the wave activity was high.

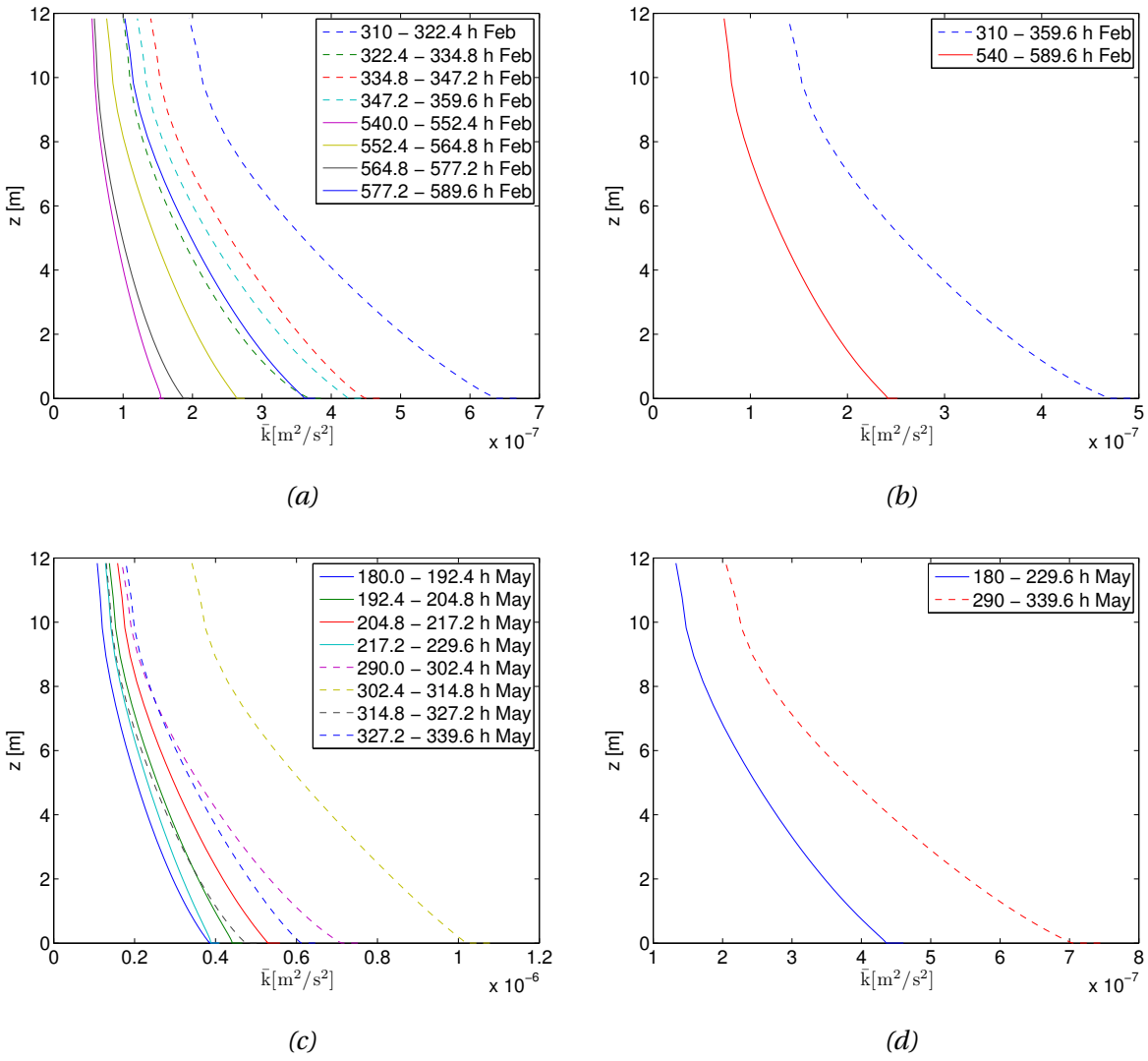

Figure 44: Mean turbulent kinetic energy $\bar{k}(z)$. Whole and stapled lines indicate low and high wave activity, respectively. In (a) and (c), each profile shows the time averaged turbulent kinetic energy over one M_2 period (i.e. 12.4 hours) from the February and May data, respectively. The whole lines in (b) and (d) are the mean of the whole lines in (a) and (c), i.e. the time averaging is done over four succeeding M_2 periods. The same applies for the stapled lines.

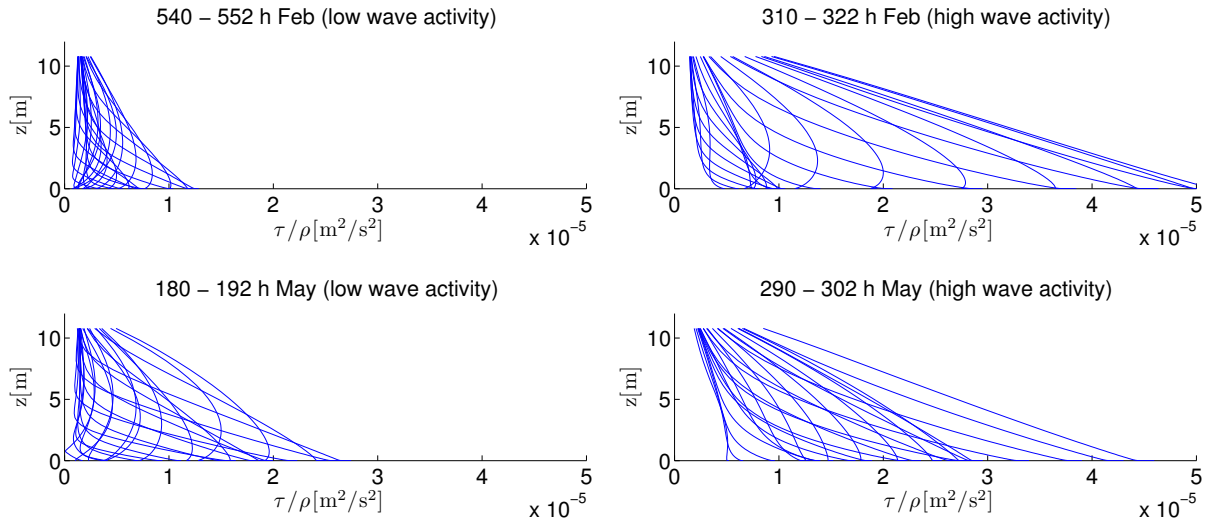

Figure 45: Total shear stress profiles (without direction), for periods of low and high wave activity, respectively. For each figure, profiles are shown for one M_2 period, with intervals of half an hour.

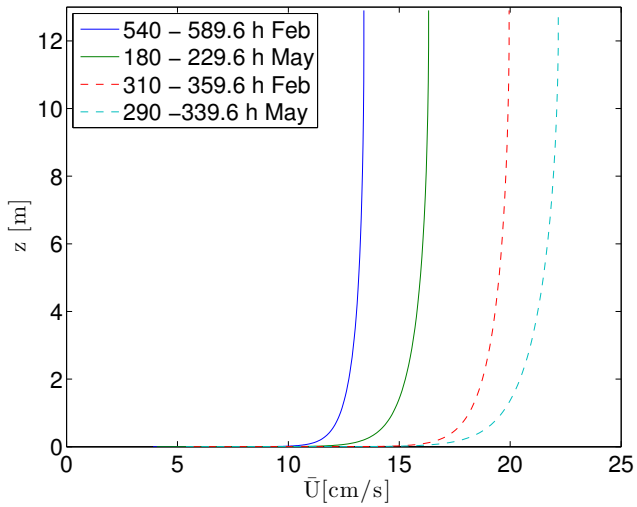

Figure 46: Comparison of mean current speed profiles from the intervals of low wave activity against those from the intervals of high wave activity. Whole and stapled lines indicate low and high wave activity, respectively.

7.7 Effect of tidal range

In the present model, the water depth h is assumed constant. In the deep sea, the magnitude of the tidal range relative to the depth is of course much smaller than close to shore. In addition, the tidal range in the deep sea is generally smaller than in the nearshore area. Therefore, this has not been an issue in the previous works using the model, i.e. Holmedal and Myrhaug (2013) and the project work presented in appendix C. In the present work, where the mean depth is about 13 m and the tidal range at spring tide is about 4.5 m, the assumption of constant depth is an important issue to address. The time intervals of either low or high tidal range chosen for comparison are t ∈ <220,320> h of February (high), t ∈ <390,490> h of February (low), t ∈ <150,250> h of May (high) and t ∈ <380,480> h of May (low), see figure 21. These time intervals were chosen with the intension to ensure somewhat similar wave conditions for all intervals. However, this was only partially possible. Times of very high wave activity was avoided, but as we see in figures 22 and 23, the wave conditions of the four intervals are not similar. Of the February intervals, the waves are a little higher in the interval of high tidal range than in the low-range interval. In the May intervals, we have the opposite case.

The modeled velocities during the above intervals are compared with the field data in figures 47 - 50. In these figures, the velocities during low tidal ranges do not seem to be more correctly modeled than the velocities during high tidal ranges. If there is a correlation between tidal range and the accuracy of the model, it is too small to detect visually from time series. Calculating the error (e.g. by using the squared error given by equation (7.1)) is not suitable, as the difference between the intervals would be too small to make a conclusion, due to the numerous possible error sources. As expected, the velocities are higher during the intervals of high tidal range. We note that the velocities are closer to sinusoidal during periods of high tidal range than in periods of low tidal range. This is also as expected, because the increase in tidally induced velocities will enhance their dominance. In figure 51, graphs are shown for the turbulent kinetic energy k averaged over the four time intervals. Due to the length of the intervals, the averaging period is not taken as a finite number of M_2 periods (as we did in the examination of wind and wave effects). This proved to make insignificant difference. For both months, $\overline{k}$ is greater in the interval of high tidal range. Similarly to

what was discussed for varying wave conditions in chapter 7.6, this is most likely a direct effect of increased velocities. Further, we see that the difference in averaged turbulent kinetic energy is significantly greater between the February intervals than the May intervals. The main reasons for this are assumably that the difference in tidal range is largest between the February intervals (see figure 21), and the differences in wave conditions mentioned above. These considerations are supported by figure 52, where the mean current speed profiles for the intervals are shown. This figure confirms that the current is stronger in the periods of high tidal range, and we see that the difference is much larger between the February intervals than the May intervals.

In the pre-master project work presented in appendix C, it was found that the water depth h has an effect on the orientation of the tidal ellipses. The field data used in the project work was made roughly 950 km south of the transducer location of the field data from the Hebrides used in the present work, hence on the same hemisphere. In the results presented in appendix C, the most important effect of depth on the tidal ellipses was that a decrease in depth resulted in a clockwise rotation of the ellipses. For a reduction of the water depth from 60 to 30 m, the tidal ellipse at an elevation of about 1 m above the bottom was rotated about 9°. This means that the assumption of constant depth in the model should have an effect on the agreement between model results and field data in the present work. In figure 63, appendix B, the velocities are plotted in the horizontal plane, for the periods of low and high tidal ranges defined above. As described in chapter 2.4, such plots will display an ellipse if only one tidal constituent is plotted. Here, the plots are more chaotic, because many tidal constituents are present and due to velocity components not induced by the tides. The figures indicate that the flow predicted by the model in the periods of high tidal range is rotated clockwise with respect to the field data. The same tendency is not found in the plots from periods of low tidal range. It should be noted, however, that these plots are more irregular, and more difficult to compare. The tendency corresponds to the findings from the project work. This can be explained as follows. We first consider one half tidal period, where the water depth is greater than the mean depth. During this period, the model assumes a too small depth, and therefore predicts an ellipse orientation rotated clockwise with respect to the field data. This effect will be counteracted during the succeeding half tidal period, when the model assumes a water depth greater than the real depth. Because the effect of depth on the

ellipse orientation is nonlinear (the effect increases with decreasing depth), the errors will not cancel each other. The error made by the model during the first of the two half periods will be greater than the error made during the latter half period. If we now assume that the effects are not purely spontaneous, but influence the flow over time, we expect the predicted ellipses to be rotated in the clockwise direction relative to the field data. This corresponds to the tendency indicated by figure 63.

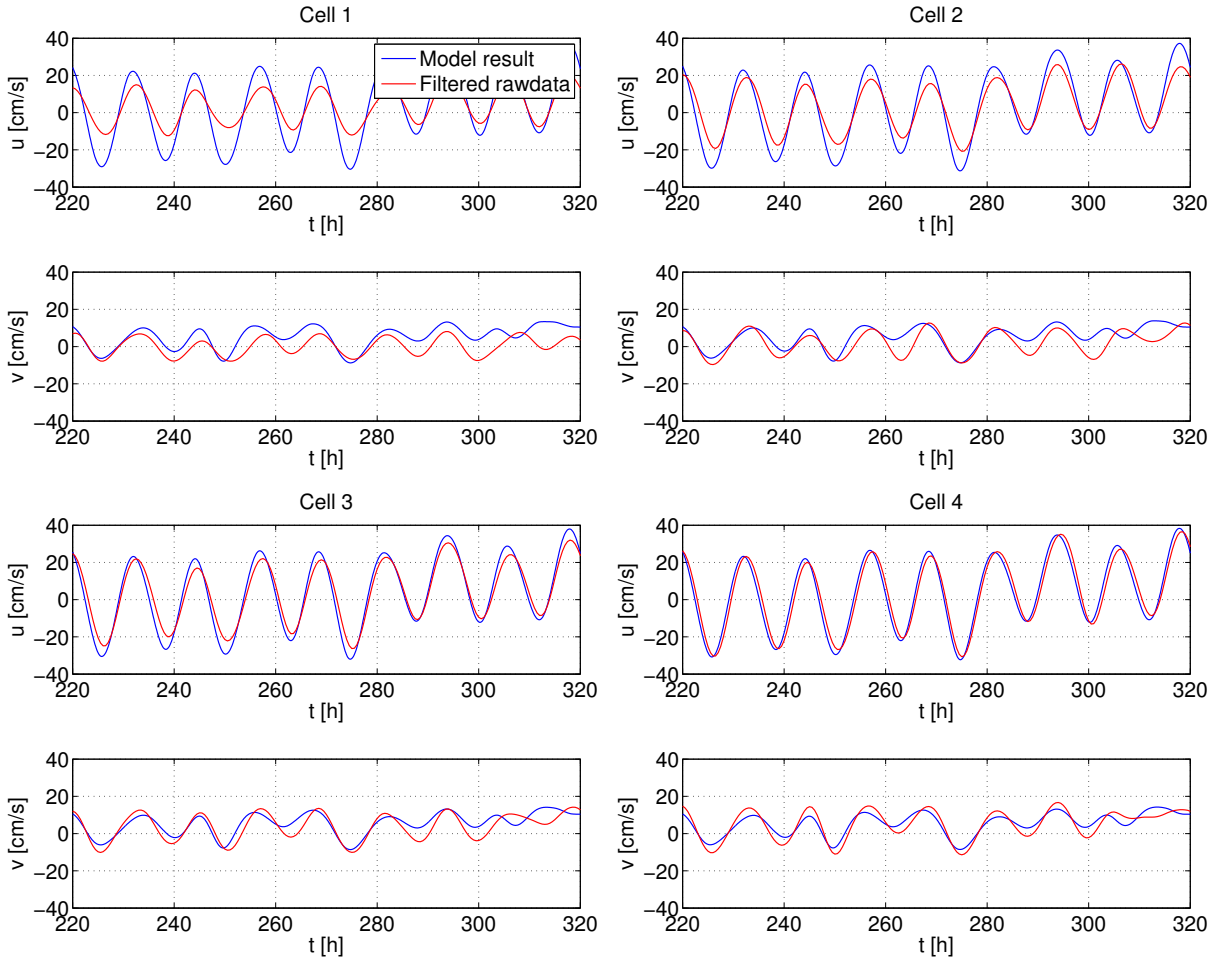

Figure 47: Model results and field data velocities in the time interval from 220 h to 320 h of February 2013. During this time interval, the tidal range was high.

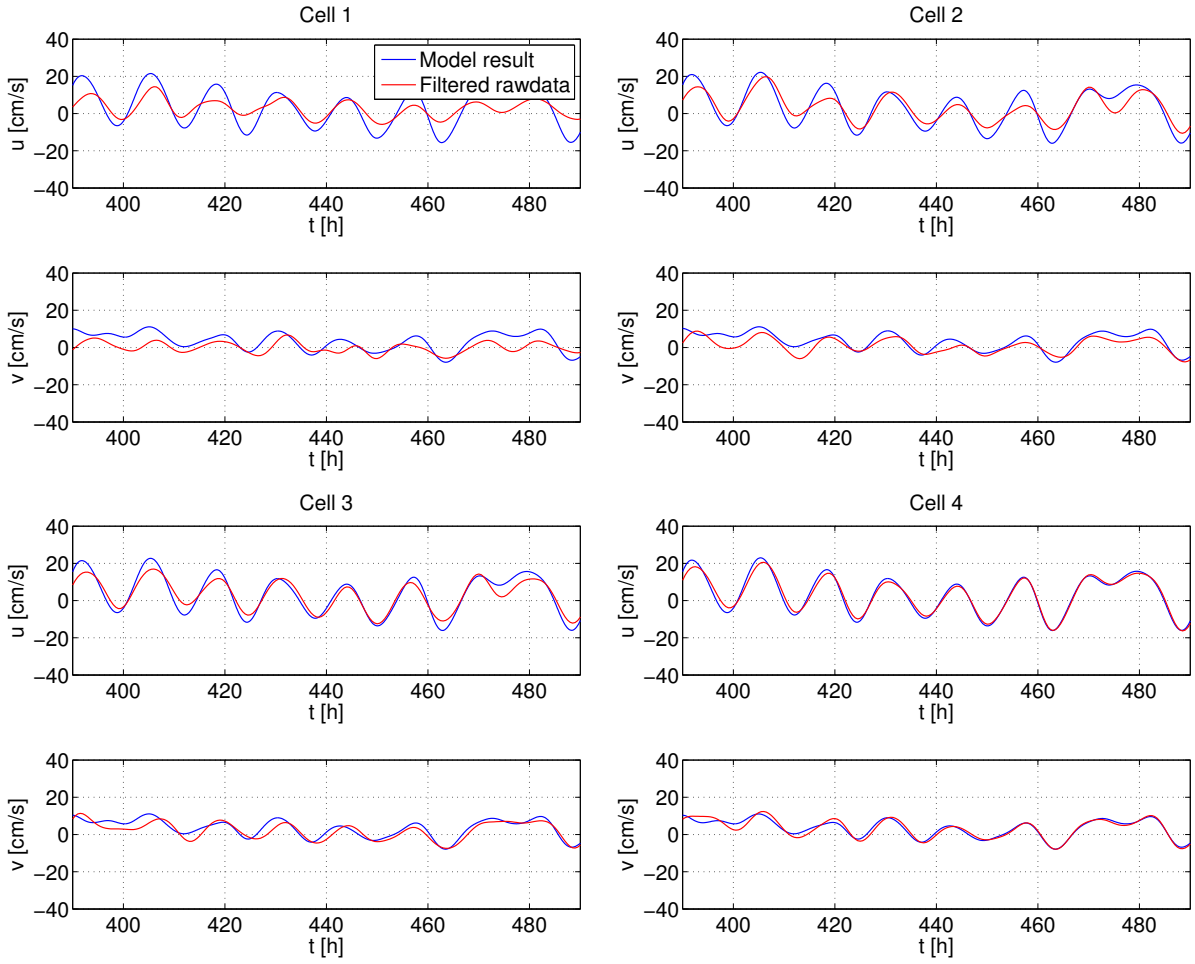

Figure 48: Model results and field data velocities in the time interval from 390 h to 490 h of February 2013. During this time interval, the tidal range was low.

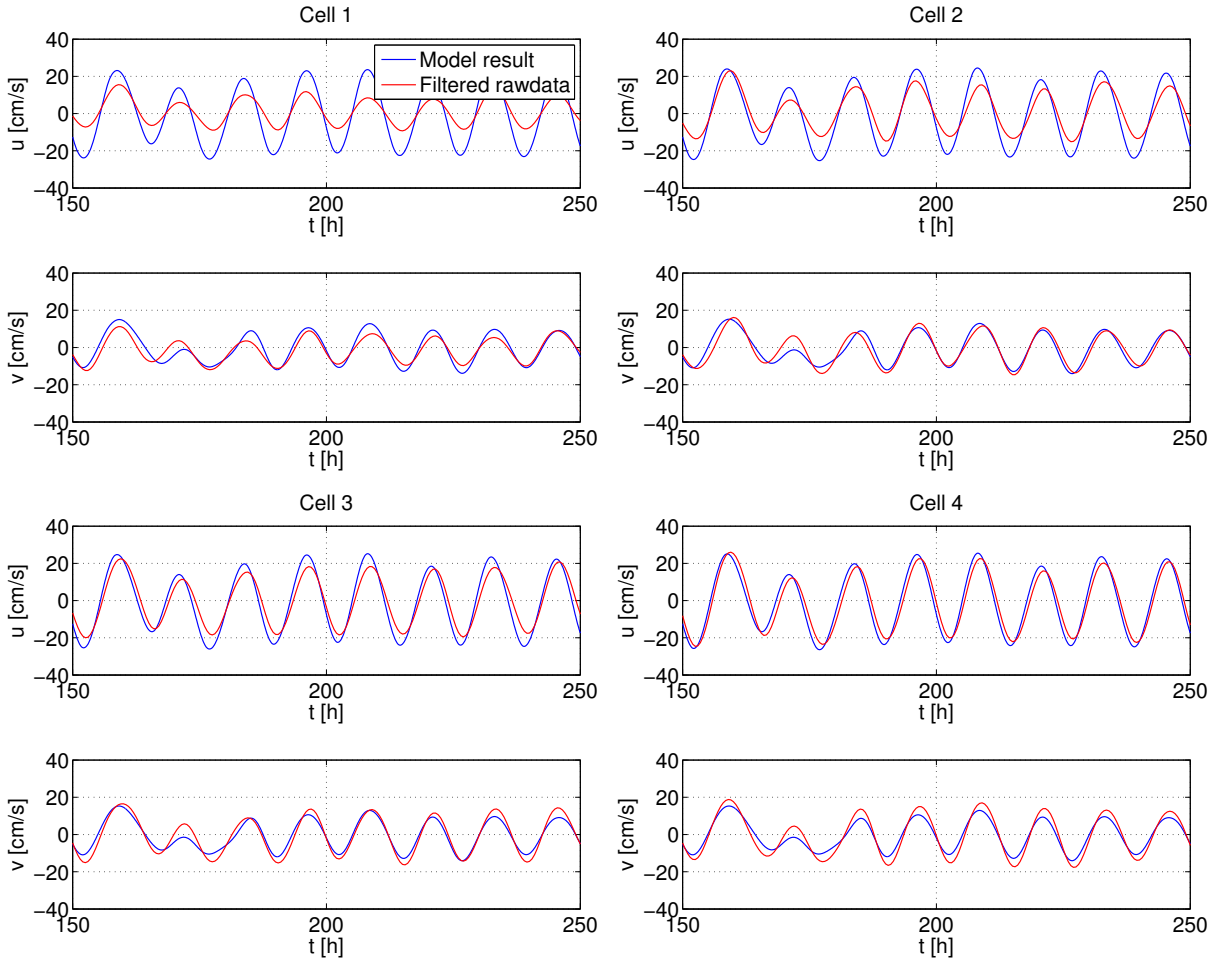

Figure 49: Model results and field data velocities in the time interval from 150 h to 250 h of May 2013. During this time interval, the tidal range was high.

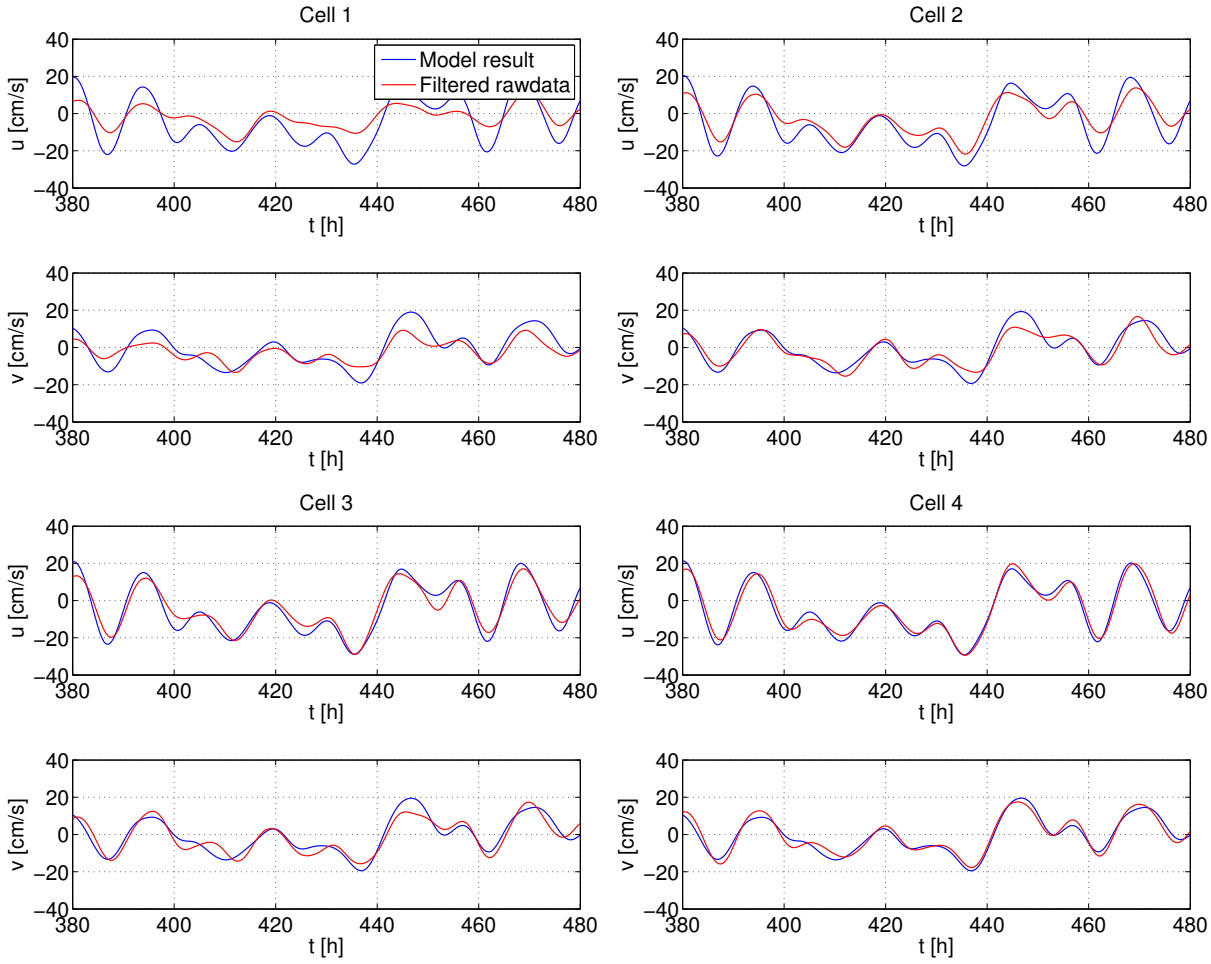

Figure 50: Model results and field data velocities in the time interval from 380 h to 480 h of May 2013. During this time interval, the tidal range was low.

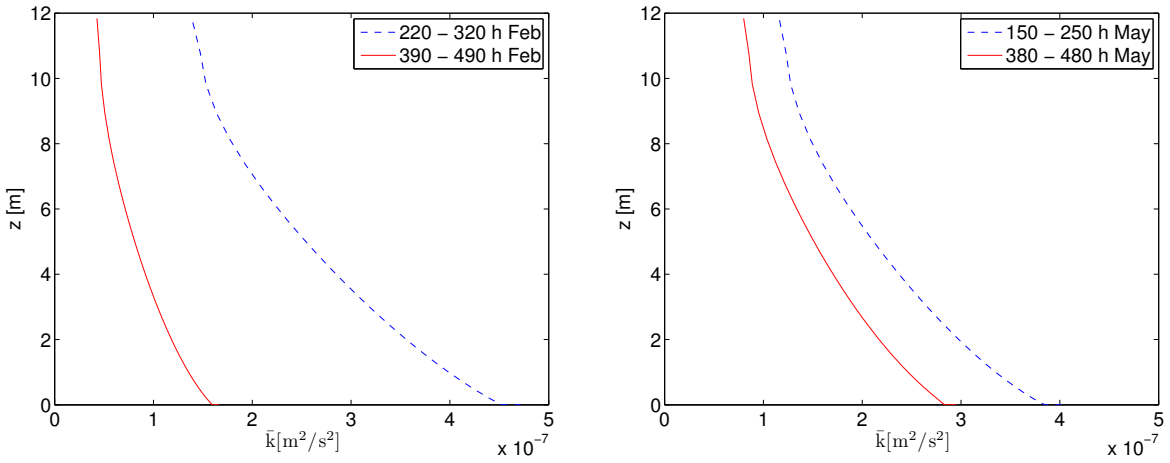

(a) *(b)*

Figure 51: Comparison of mean turbulent kinetic energy $\bar{k}(z)$ for low (whole line) and high tidal ranges (stapled lines).

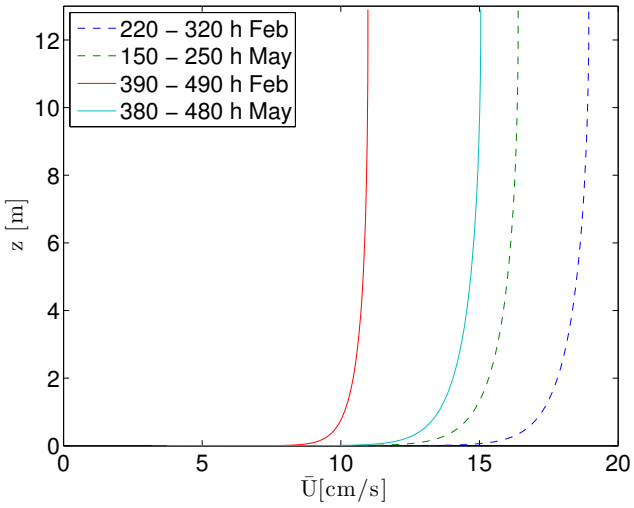

Figure 52: Comparison of mean current speed profiles from the the intervals of low tidal range against those from the intervals of high range. Whole and stapled lines indicate low and high tidal range, respectively.

8 Conclusions

Field measurements of current velocities in a coastal area at about 13 m mean depth have been applied in a one-dimensional numerical model. The purpose of the present work is to investigate the model's applicability for tidal flows in nearshore, shallow-water areas, where the flow is typically more complex than in the deep sea. The field data were filtered to remove oscillations of frequencies not related to tidal flow. However, weather effects of frequencies in the range of tidal components were present in the data. The data used to drive the flow in the model, and the data used for validation of the model results, do hence not represent pure tidal flow. Their behavior is, however, very close to that of tidal flow. The conclusions are given in the following.

The best agreement between model results and field data are obtained with a specified bottom roughness of z_0 = 0.0006 cm. This roughness gives a good agreement in the upper measuring point (quite close to the surface), but decreasing in the lower measuring points, where the velocity magnitudes are overestimated. It is emphasized that z_0 = 0.0006 cm is a very small roughness. For higher values of z_0, there is a phase shift of the time series, in opposite directions for the u and v components. This results in broader tidal ellipses than found in the field data.

The model is unable to replicate the boundary layer found in the real flow. The boundary layer in the field data covers the whole water depth, with high velocity gradients through the whole water column. In the model results, the current speed is close to constant through a large part of the water column, so that the boundary layer towards the bottom is thin. In other words, the damping towards the bottom predicted by the model is much smaller than in the measurements. This is probably a result of the complex bottom conditions at the measuring site. The bottom consists of bedrock with seaweeds and boulders. In the model, the specification of bottom conditions is limited to an equivalent sand roughness. The presence of boulders (and the measuring equipment) may result in vortex shedding, affecting the flow near the bottom. Further, the seaweed, which is quite tall, is assumed to give damping effects that cannot be replicated by specifying an equivalent sand roughness.

The boundary layer of the model results corresponds better to an empirical formula by Soulsby

(1990) than the field data does. With a specified bottom roughness of z_0 = 0.050 cm, the agreement with the formula is very good. Since the formula has previously shown to fit well to shallow-water tidal flow, this indicates that the model might be able to model tidal flow in shallow water with better accuracy than what was obtained in the present work, if the flow is less complex. For a bottom roughness of z_0 = 0.050 cm, the model predicts a hydrodynamically rough flow. For z_0 = 0.0006 cm, it predicts a hydrodynamically smooth flow. This supports the above indication of z_0 = 0.050 cm as a roughness giving a realistic boundary layer.

A tendency has been found, indicating that the model results are slightly better in time intervals of low wave activity. However, the trends are too ambiguous for a conclusion to be drawn. Further, the difference in the model's accuracy between periods of low and high tidal ranges, respectively, is very small. There is a tendency, however, indicating that the predicted tidal ellipses during periods of high tidal range is rotated clockwise relative to the field data. This corresponds to conclusions drawn in the pre-master project work. There is an increase of turbulent kinetic energy through the whole water column for both increasing wave activity and increasing tidal range. This is most likely a direct effect of the increased current speeds under these conditions. For periods of high wave activity, there is an increase in the shear stress through the water column. This is also assumed to be a direct effect of increased current speeds.

Overall, the present results are relatively good, the simplicity and efficiency of the model taken into account. The velocities at the measuring point closest to the surface is modeled with surprising accuracy. However, the discrepancies of the boundary layer means that the mass transport predicted by the model is much larger than in reality, under the present conditions. Hence, the model, in its present form, is not suitable for predictions of transport of e.g. plankton, fish larvae, algae, contaminated ballast water and other pollutants or sea bottom material. Under less complex conditions, however, there is a good chance that it might be applicable for such predictions also in shallow water.

9 Recommendations for further work

In the present results, indications are found that the model might be able to model shallow-water tidal flow with higher accuracy than found here, if the conditions are less complex. The main issue is the damping of the flow towards the bottom. Further studies should address the different natures of shallow-water tidal boundary layers and investigate the hypothesis that the results will be better for tidal flows with the more general boundary layer covering an area in the lower part of the water column and with a close to constant current speed in the upper part of the water column. In chapter 7, it is argued that also shallow-water tidal flows may exhibit this type of boundary layer.

Further works could also attempt to include the effects of seaweed on the bottom. Such effects are assumed to be the main contributors to the discrepancies in the present work. Hence, to improve the accuracy under the present conditions, this would be a natural starting point.

Effects of wave activity and tidal range on the modeling accuracy were found to be very small in this work. It is possible that analyses of longer time series would demonstrate a clearer dependency. However, the present results indicate that such effects are of little significance. Hence, the studies proposed above should be prioritized.

As described in chapter 6.3, residual currents were found in the field data used in the present work. The behavior of these current components (specifically their rotation through the water column), indicated that they could be wind-generated. However, comparison with wind measurements did not reveal any correlation. The generation effects of the residual currents could be an interesting study.

References

Brown, J., Colling, A., Park, D., Phillips, J., Rothery, D., and Wright, J. (1989). *Waves, tides and shallow-water processes*. Pergamont Press.

Cai, S., Long, X., Liu, H., and Wang, S. (2006). Tide model evaluation under different conditions. *Continental Shelf Research*, 26:104–112.

Colebrook, C. F. and White, C. M. (1937). Experiments with fluid friction in roughened pipes. *Proc. Roy. Soc., Series A*, 161:367–381.

Cushman-Roisin, B. (1994). *Introduction to geophysical fluid dynamics*. Prentice Hall, Englewood Cliffs, N.J.

Dean, R. G. and Dalrymple, R. A. (1984). *Water Wave Mechanics for Engineers and Scientists*. Prentice Hall, Inc.

Dronkers, J. (2005). *Dynamics of Coastal Systems*, volume 25 of *Advanced Series on Ocean Engineering*. World Scientific Publishing Co. Pte. Ltd.

Grant, W. D. and Madsen, O. S. (1979). Combined wave and current interaction with a rough bottom. *Journal of Geophysical Research*, 84:1797–1808.

Hicks, S. D. (2006). *Understanding Tides*. U.S. Department of Commerce, National Oceanic and Atmospheric Administration, National Ocean Service.

Holmedal, L. E. (2002). *Wave-current interactions in the vicinity of the sea bed*. Ph.d. Norwegian University of Science and Technology.

Holmedal, L. E. and Myrhaug, D. (2013). Combined tidal and wind driven flows and bedload transport over a flat bottom. *Ocean modelling*, 68:37–56.

Jones, N. L. and Monismith, S. G. (2008). Modeling the influence of wave-enhanced turbulence in a shallow tide- and wind-driven water column. *Journal of Geophysical Research*, 113.

King, H. L., Davies, A. G., and Soulsby, R. L. (1985). A numerical model of the turbulent boundary layer beneath surface waves and tides. *Technical Report*, 196.

Kolmogorov, A. N. (1942). *Equations of turbulent motion of an incompressible fluid.* Izv. Akad. Nauk. SSR, Seria fizicheska Vi (English translation: Imperial College, Mech. Eng. Dept. Rept. ON/6, 1968).

Kraus, E. B. and Businger, J. A. (1994). *Atmosphere-Ocean Interaction.* Oxford University Press, 2. edition.

LeBlond, P. H. (1991). *Tides and their interactions with other oceanographic phenomena in shallow water (review)*, book section 18, pages 357–378. John Wiley and Sons, Inc.

MacMahan, J. H., Thornton, E., and Reniers, A. J. H. M. (2006). Rip current review. *Coastal Engineering*, 53:191–208.

Madsen, O. S. (1977). A realistic model of the wind-induced Ekman boundary layer. *Journal of Physical Oceanography*, 7:248–255.

Mellor, G. L. and Yamada, T. (1982). Development of a turbulence closure model for geophysical fluid problems. *Rev. Geophys.*, 20:851–875.

Mossman, D. J. (2001). Bay of fundy tides. *Journal of the Geological Association of Canada*, 28.

Myrhaug, D. (2006). *Oceanography: Wind, Waves, Compendium for TMR4230.* Akademika forlag.

Myrhaug, D. (2012). *Oceanography: Current, Compendium for TMR4230.* Akademika forlag.

Myrhaug, D. and Slaattelid, O. H. (1996). Bottom shear stresses and velocity profiles in stratified tidal planetary boundary layer flow from similarity theory. *Journal of marine systems*, 14:167–180.

Nansen, F. (1902). *The Norwegian North Polar expedition 1893-1896, scientific results.* Longmans, Green and co., London.

Nielsen, P. (1992). *Coastal Bottom Boundary Layers and Sediment Transport.* World Scientific Publishing Co. Pte. Ltd.

Niwa, Y. and Hibiya, T. (2004). Three-dimensional numerical simulation of M2 internal tides in the East China Sea. *Journal of Geophysical Research*, 109:C04027.

Noble, M., Rosenfeld, L. K., Smith, R. L., Gardner, J. V., and Beardsley, R. C. (1987). Tidal currents seaward of the Northern California continental shelf. *Journal of Geophysical Research*, 92:1733–1744.

Parker, B. B. (2007). *Tidal Analysis and Prediction, NOAA Special Publication NOS CO-OPS 3*. U.S. Department of Commerce, National Oceanic and Atmospheric Administration, National Ocean Service.

Pinet, P. R. (2006). *Invitation to oceanography*. Jones and Bartlett Publishers, Inc., 4 edition.

Pope, S. B. (2000). *Turbulent flows*. Cambridge University Press, Cambridge.

Prandle, D. (1982). The vertical structure of tidal currents and other oscillatory flows. *Continental Shelf Research*, 1:191–207.

Prandtl, L. (1945). Über ein neues formelsystem für die ausgebildete turbulenz. *Nachr. Akad. Wiss. Göttingen, Math. Phys. Klasse*, pages 6–19.

Richardson, L. F. (1922). *Weather Prediction by Numerical Process*. Cambridge University Press.

Rodi, W. (1987). Examples of calculation methods for flow and mixing in stratified fluids. *J. Geophys. Res.*, 92:5305–5328.

Sakamoto, K. and Akitomo, K. (2008). The tidally induced bottom boundary layer in a rotating frame; similarity of turbulence. *J. Fluid Mech.*, 615:1–25.

Salon, S. and Armenio, V. (2011). A numerical investigation of the turbulent Stokes-Ekman bottom boundary layer. *J. Fluid Mech.*, 684:316–352.

Schlichting, H., Gersten, K., and Mayes, K. (2000). *Boundary-layer theory*. Springer, Berlin.

Shepard, F., Emery, K. O., and La Fond, E. C. (1941). Rip currents: A process of geological importance. *The Journal of Geology*, 49:337–369.

Soulsby, R. (1990). Tidal-current boundary layers. *The Sea, Ocean Engineering Science*, 9:523–566.

Soulsby, R. (1997). *Dynamics of marine sands: a manual for practical applications*. Thomas Telford, London.

Steele, J. H., Thorpe, S. A., and Turekian, K. K. (2001). *Encyclopedia of ocean sciences*. Academic Press, San Diego.

Svendsen, I. A. (2006). *Introduction to Nearshore Hydrodynamics*, volume 24 of *Advanced Series on Ocean Engineering*. World Scientific Publishing Co. Pte. Ltd.

Van Doorn, T. (1982). Experimenteel onderzoek naar het snelheidsveld in de turbulente bodemgreenslaag in een oscillerende stroming in een golftunnel. Report. TOW-Report M 1562-1a, Delft Hydraulics Laboratories.

Van Dyke, M. (1982). *An album of fluid motion*. Parabolic Press, Stanford, Calif.

Vögler, A. (2015). Personal communication.

Wilcox, D. C. (1988). Reassessment of the scale-determining equation for advanced turbulence models. *AIAA J.*, 26(1299-1310).

Yu, J. and Chen, S. (2015). Hydrodynamic instability mechanism for rip currents. *Studies in applied mathematics*. doi: 10.1111/sapm.12074.

Çengel, Y. A. and Cimbala, J. M. (2010). *Fluid Mechanics: Fundamentals and Applications*. McGraw-Hill, Boston. 2nd ed. in SI units.

Appendices

A Time series of model results with other bottom roughness values

The time series of the velocities from the field measurements and of the model results with bottom roughness z_0 = 0.0006 cm, which was found to give the best results, are shown in chapter 7. Here, time series from some of the model runs with other z_0 values are shown, for comparison.

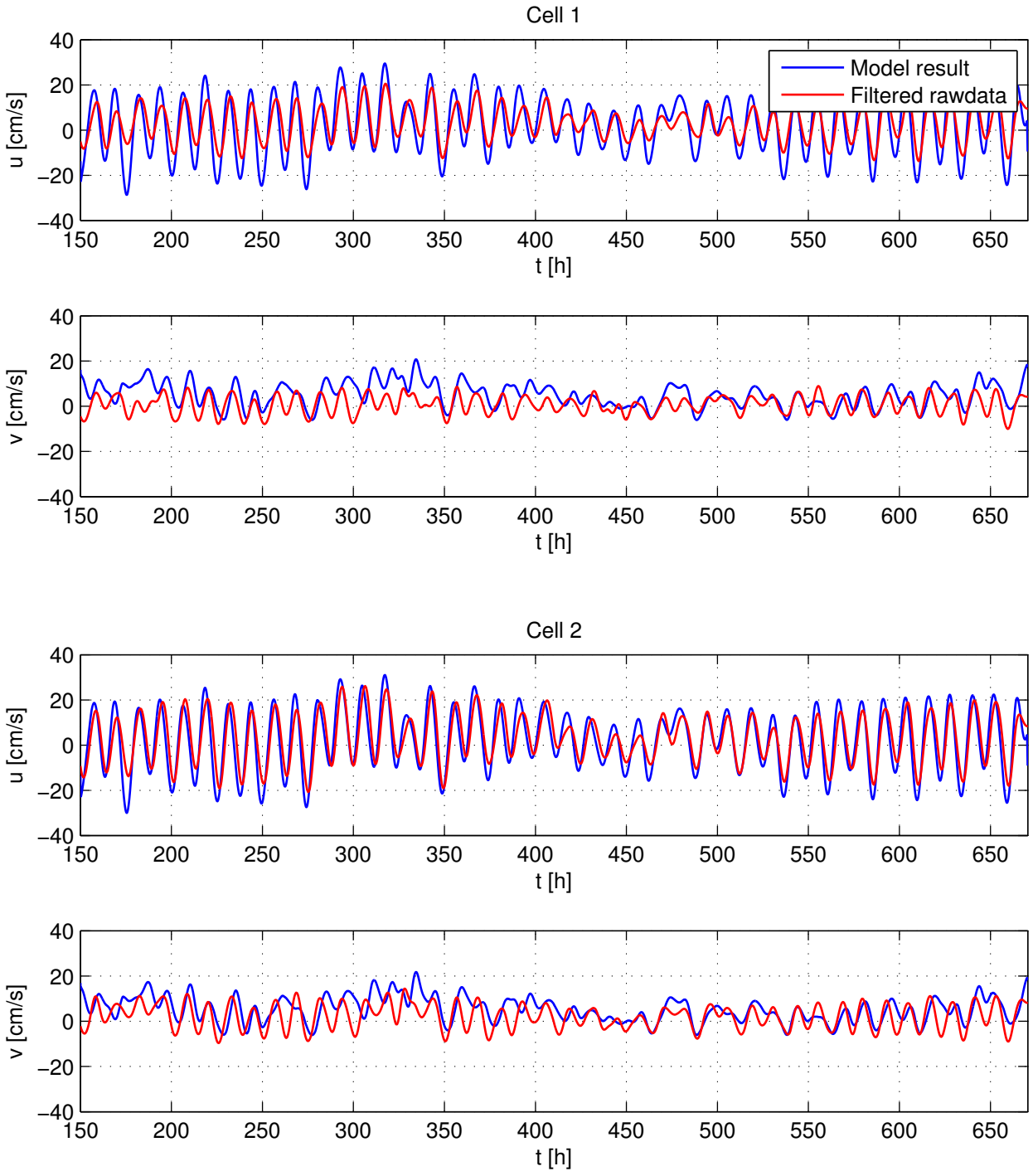

Figure 53: Model results and field data for February 2013, cell 1 and 2, with bottom roughness z_0 = 0.010 cm.

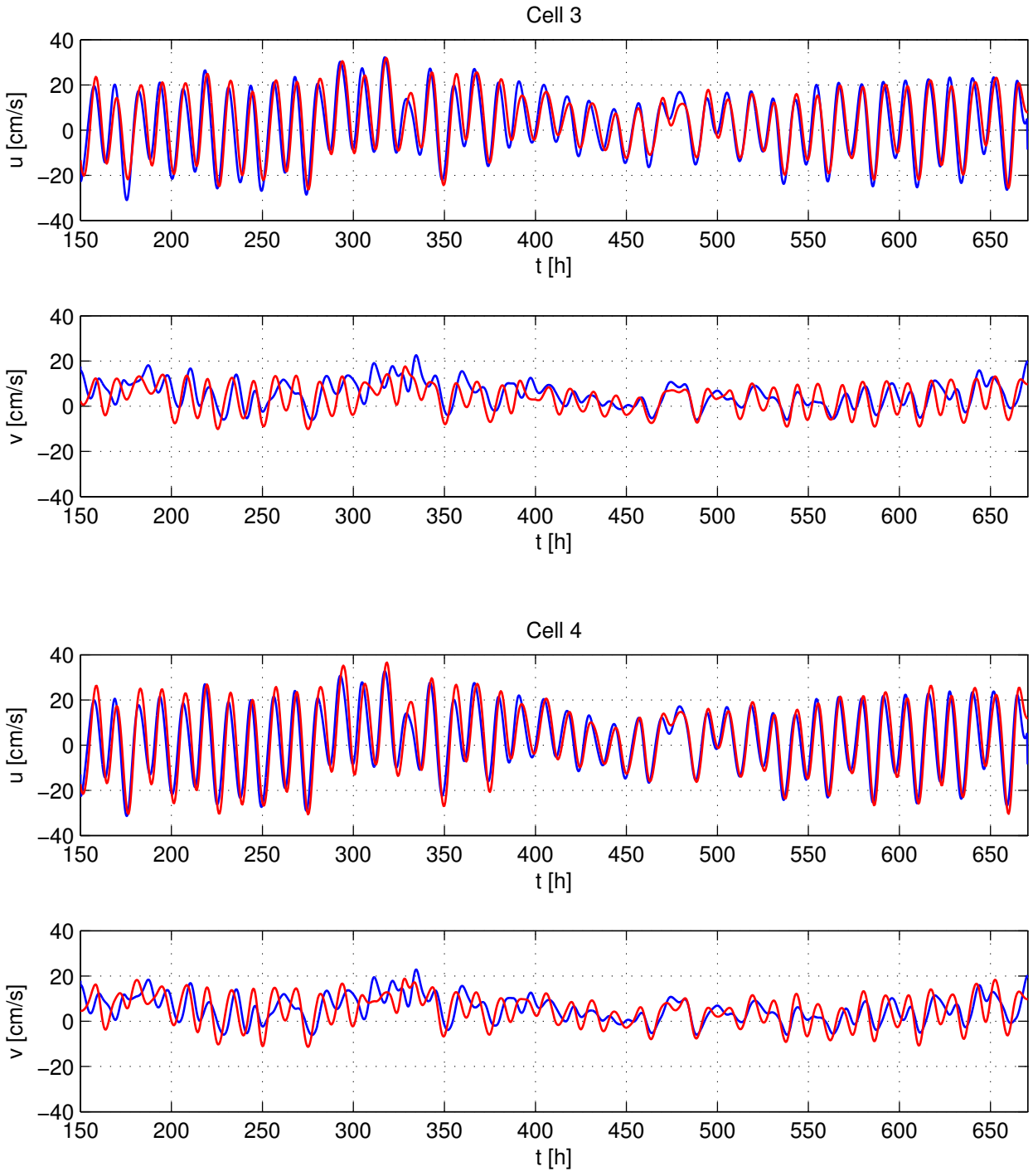

Figure 54: Model results and field data for February 2013, cell 3 and 4, with bottom roughness $z_0 = 0.010$ cm.

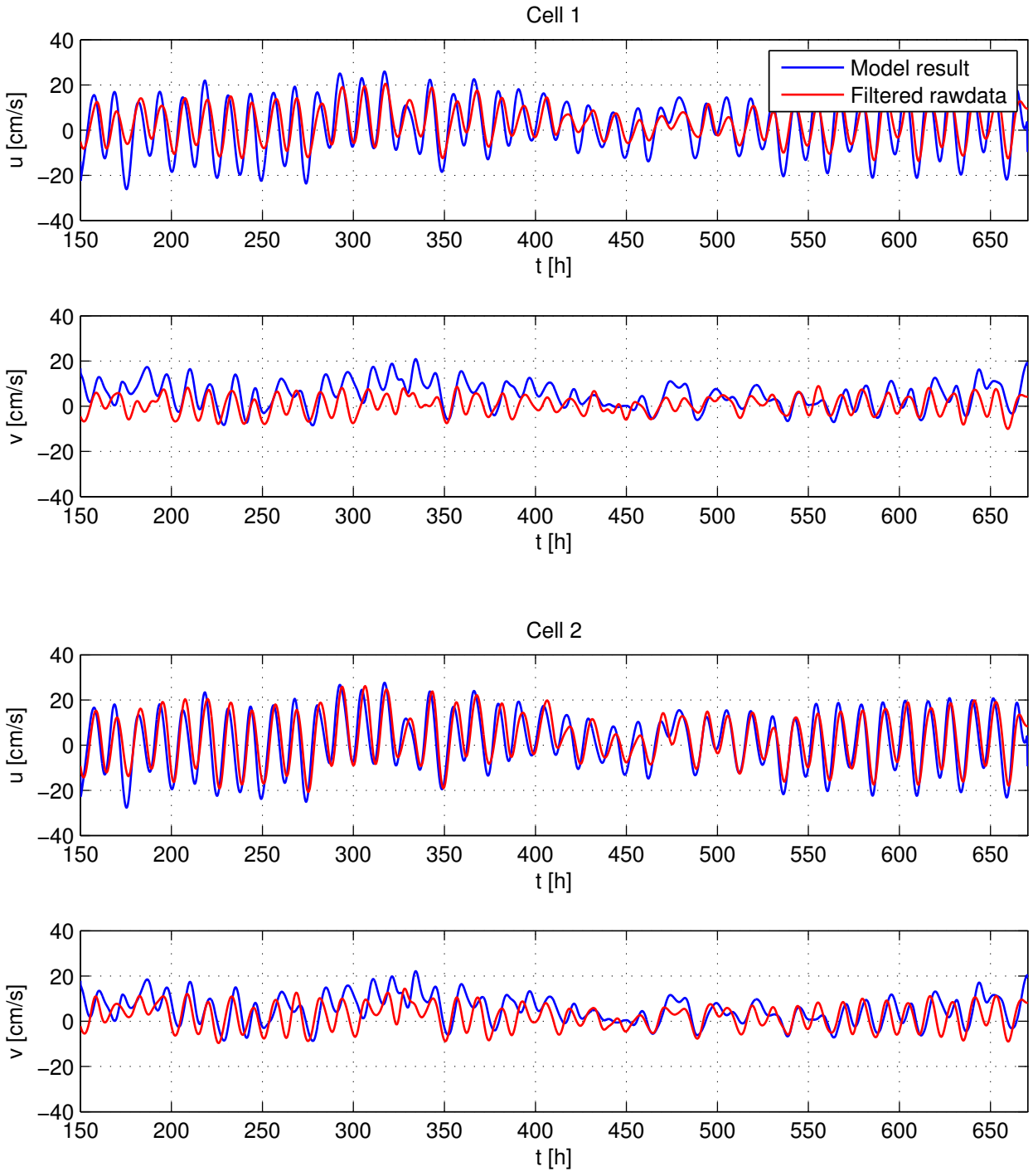

Figure 55: Model results and field data for February 2013, cell 1 and 2, with bottom roughness z_0 = 0.050 cm.

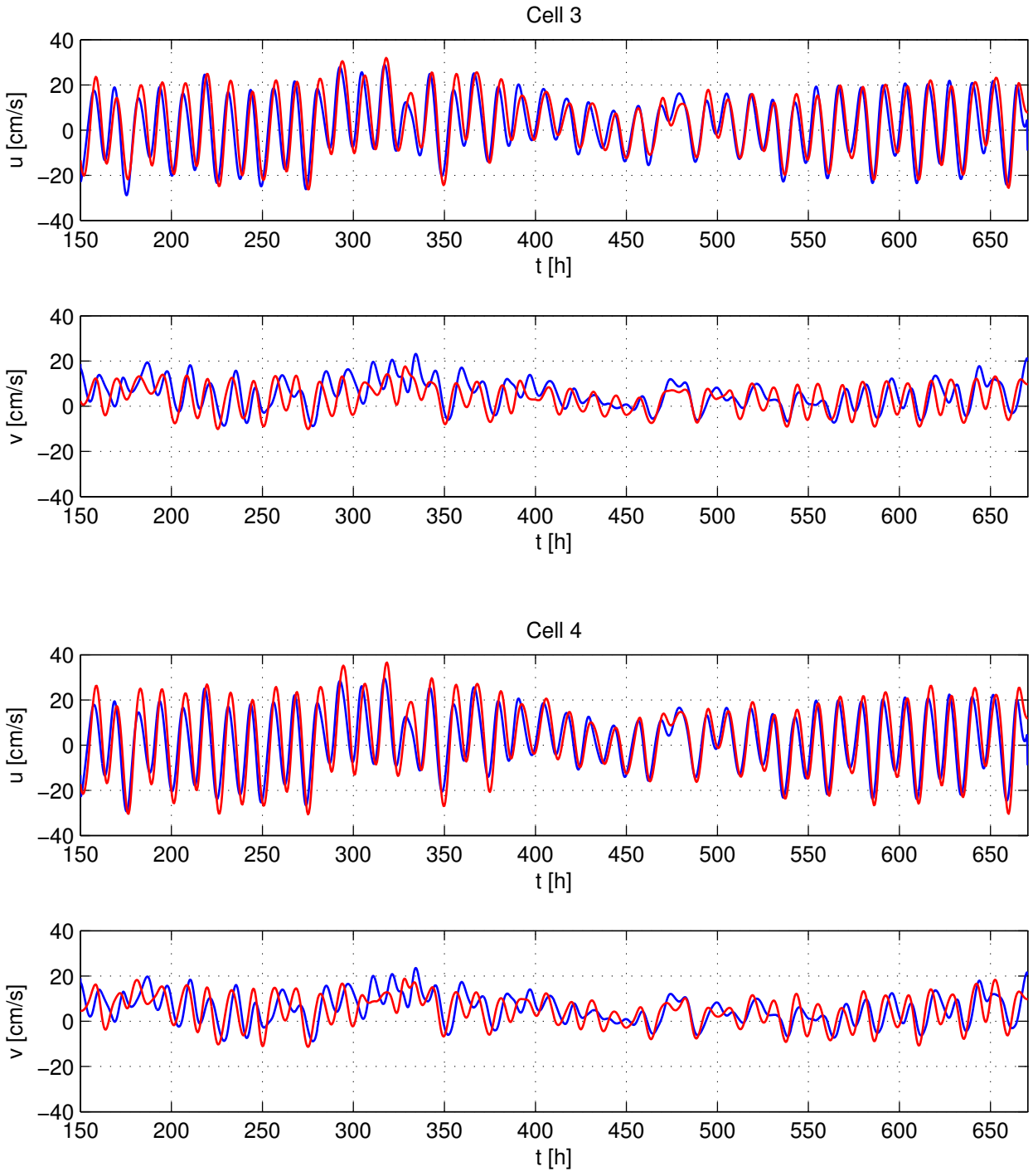

Figure 56: Model results and field data for February 2013, cell 3 and 4, with bottom roughness $z_0 = 0.050$ cm.

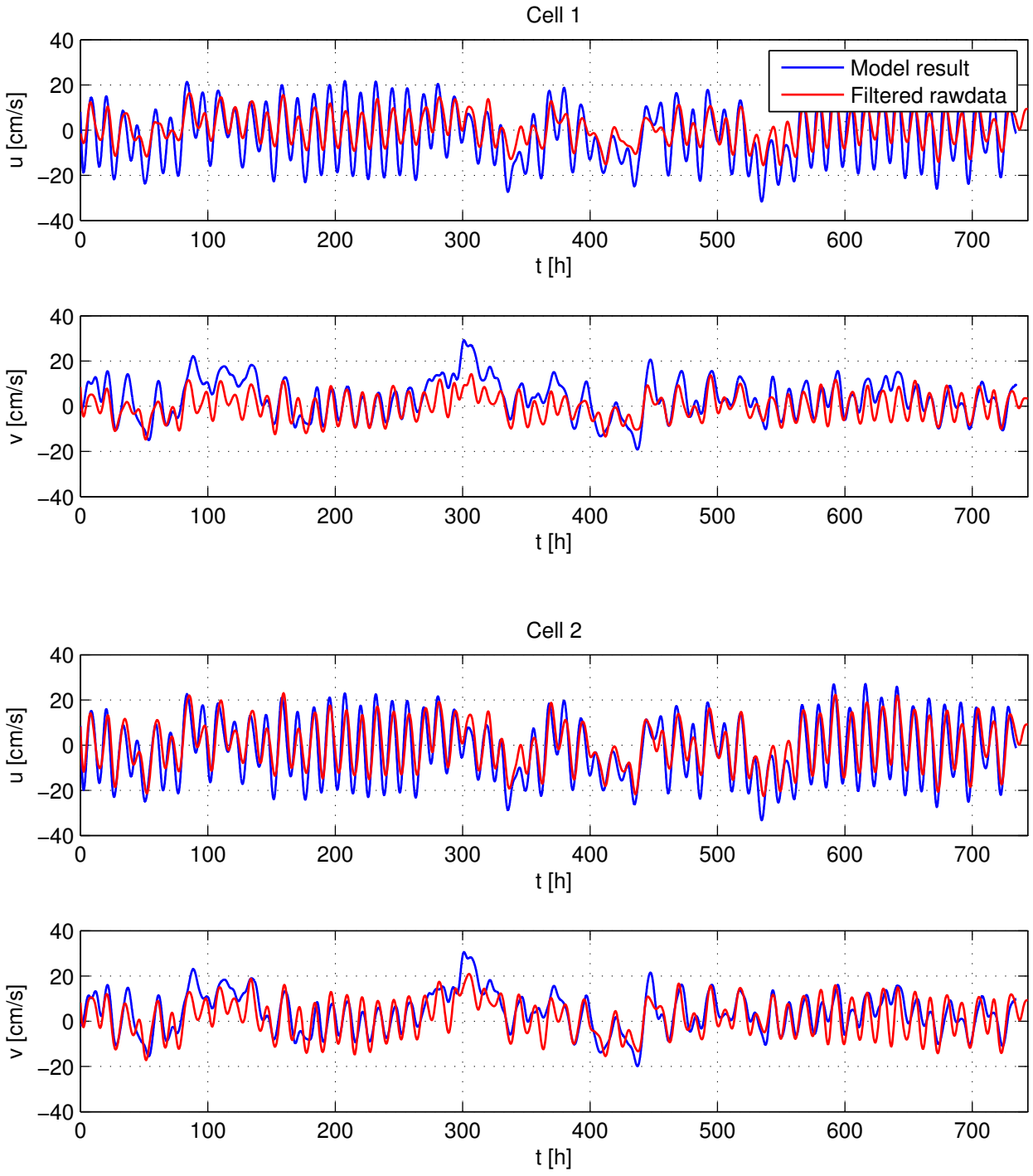

Figure 57: Model results and field data for May 2013, cell 1 and 2, with bottom roughness z_0 = 0.010 cm.

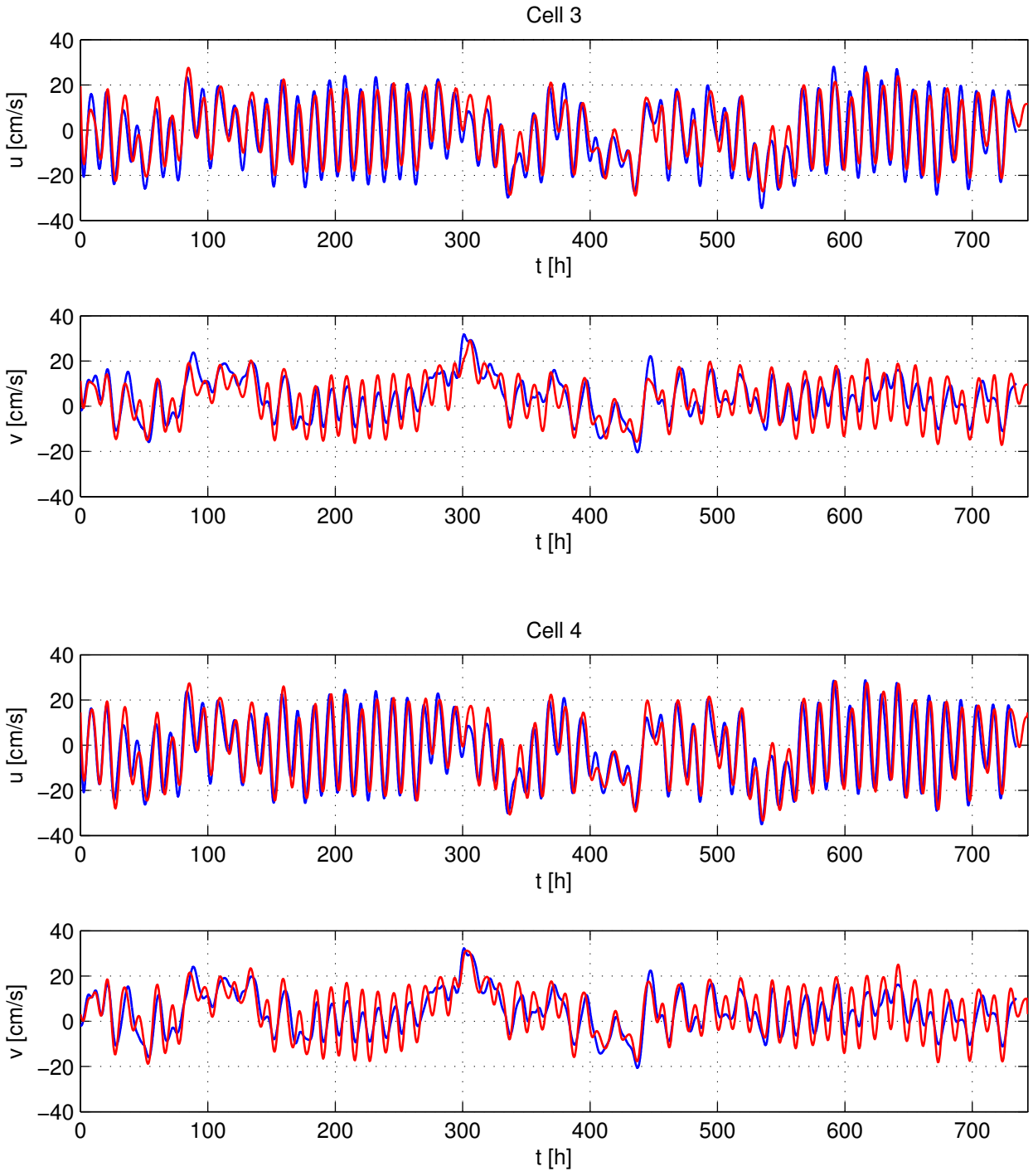

Figure 58: Model results and field data for May 2013, cell 3 and 4, with bottom roughness z_0 = 0.010 cm.

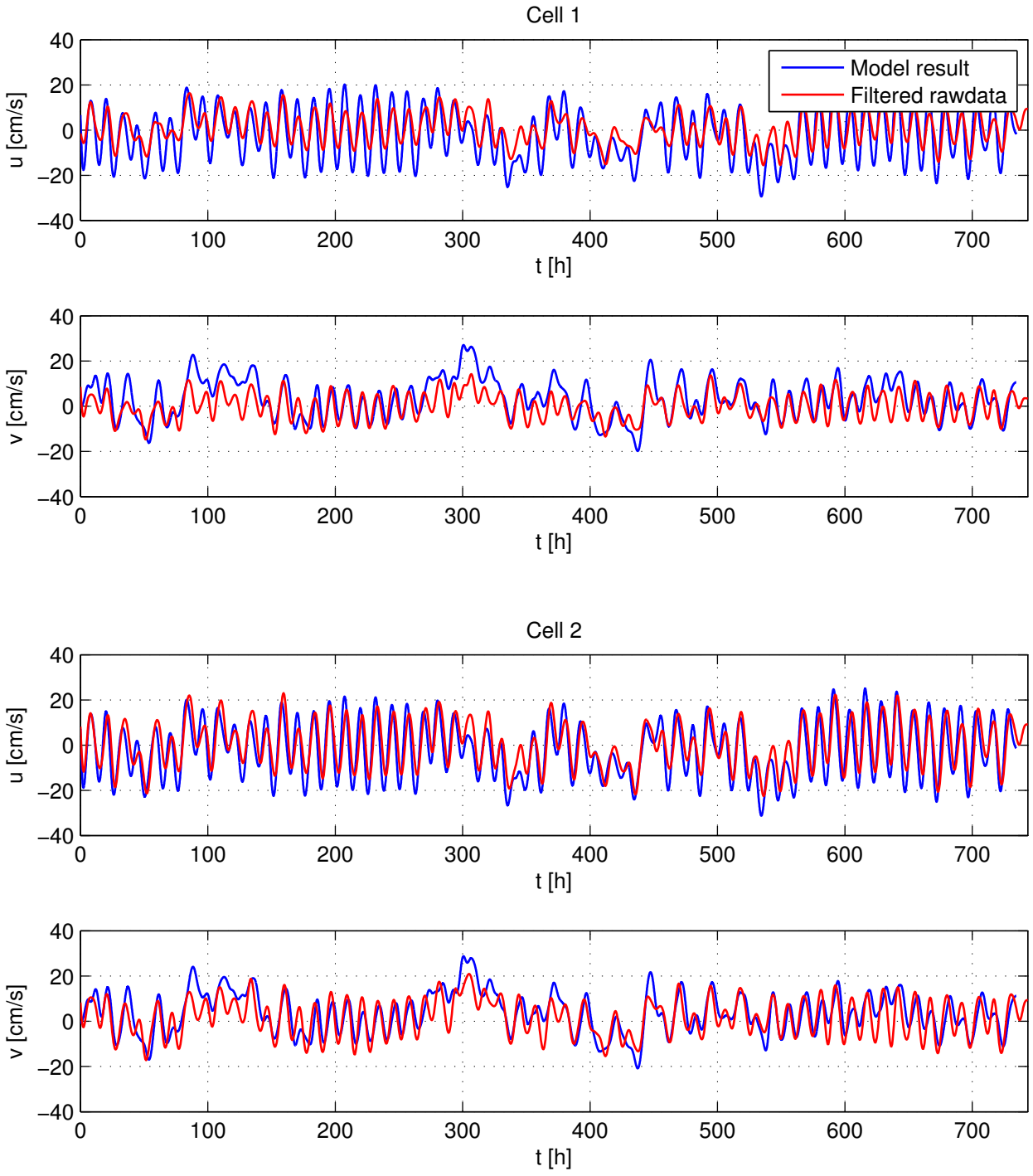

Figure 59: Model results and field data for May 2013, cell 1 and 2, with bottom roughness z_0 = 0.050 cm.

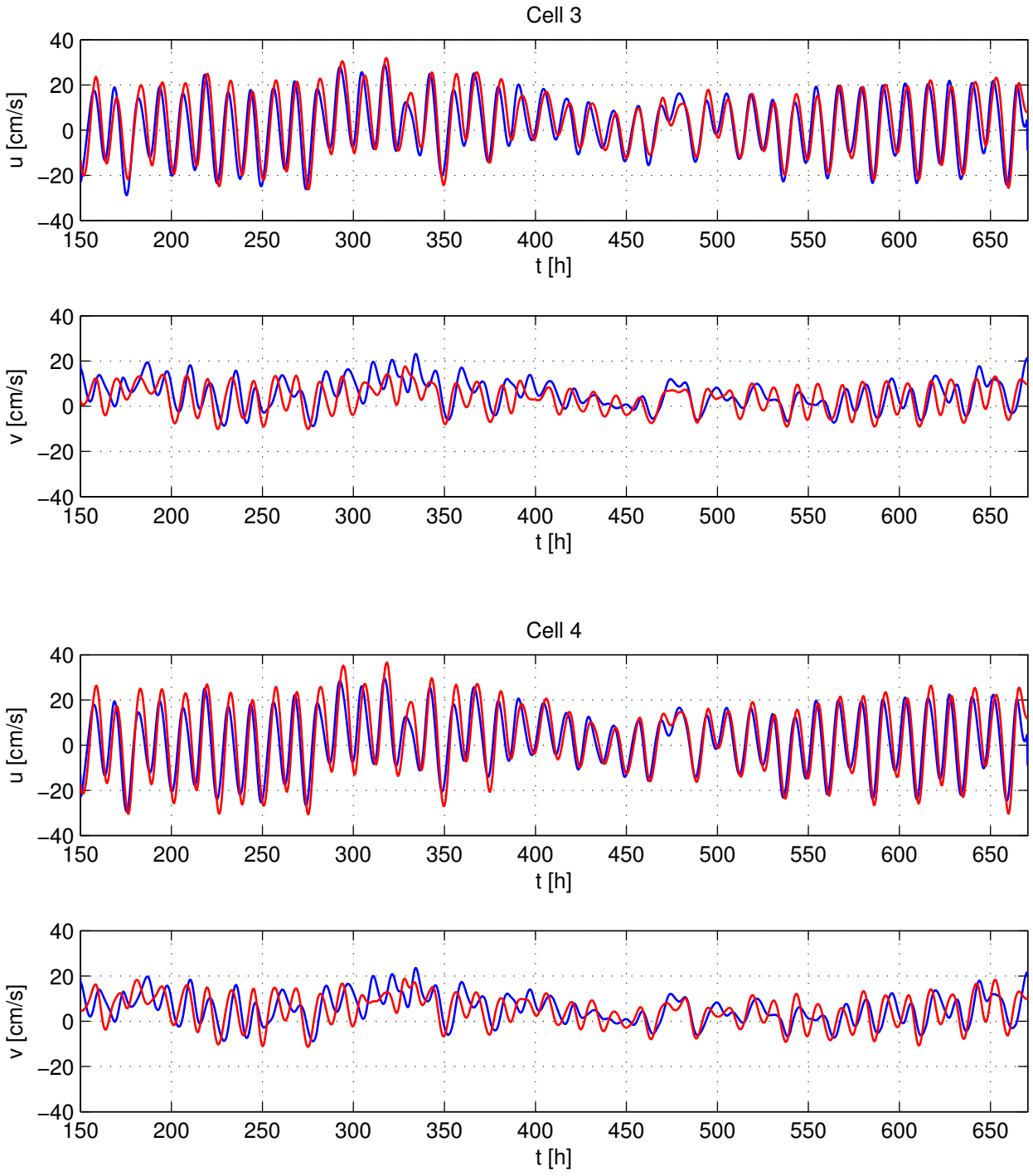

Figure 60: Model results and field data for May 2013, cell 3 and 4, with bottom roughness z_0 = 0.050 cm.

B Velocity plots in the horizontal plane

The velocities of the field data and the model results are plotted in the horizontal plane. In theory, such plots will form ellipses, at least if we plot velocities for one tidal constituent only. Here, the velocities are much more chaotic, because many tidal constituents are present and due to velocity components not induced by the tides. These plots may appear non-scientific, but they illustrate very clearly the direction and magnitude of the current (and the correlation between these) through the tidal cycle. The plots for different bottom roughnesses illustrate that the predicted mass transport (and especially its direction) at a given elevation over the bottom is highly dependent on the specified bottom roughness.

B.1 Effect of bottom roughness

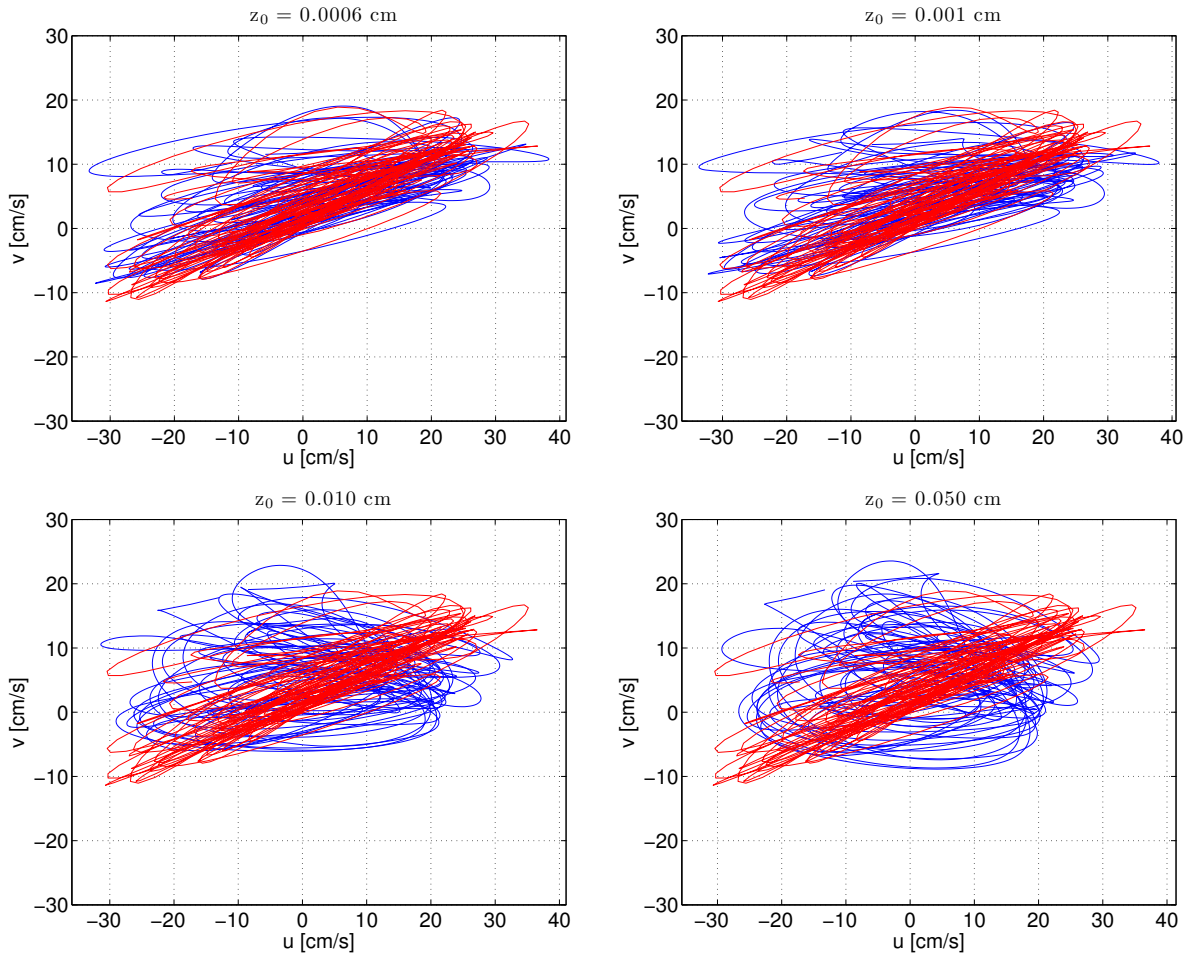

Figure 61: Velocity plots in the horizontal plane for February 2013. Red lines denote field data, while blue lines denote model results. The velocities shown are from an elevation of 9.15 m above the bottom (cell 4).

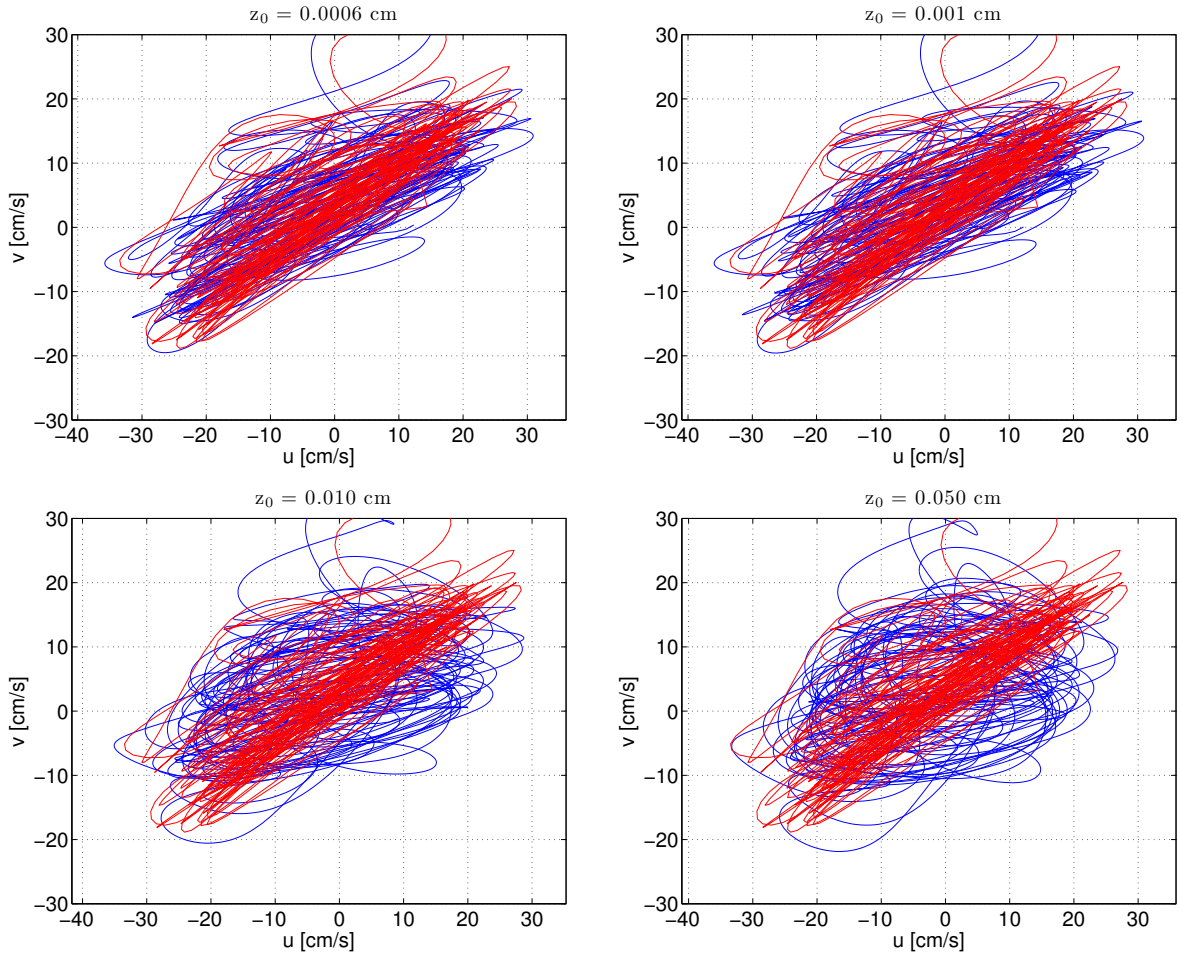

Figure 62: Velocity plots in the horizontal plane for May 2013. Red lines denote field data, while blue lines denote model results. The velocities shown are from an elevation of 9.15 m above the bottom (cell 4).

B.2 Effect of tidal range

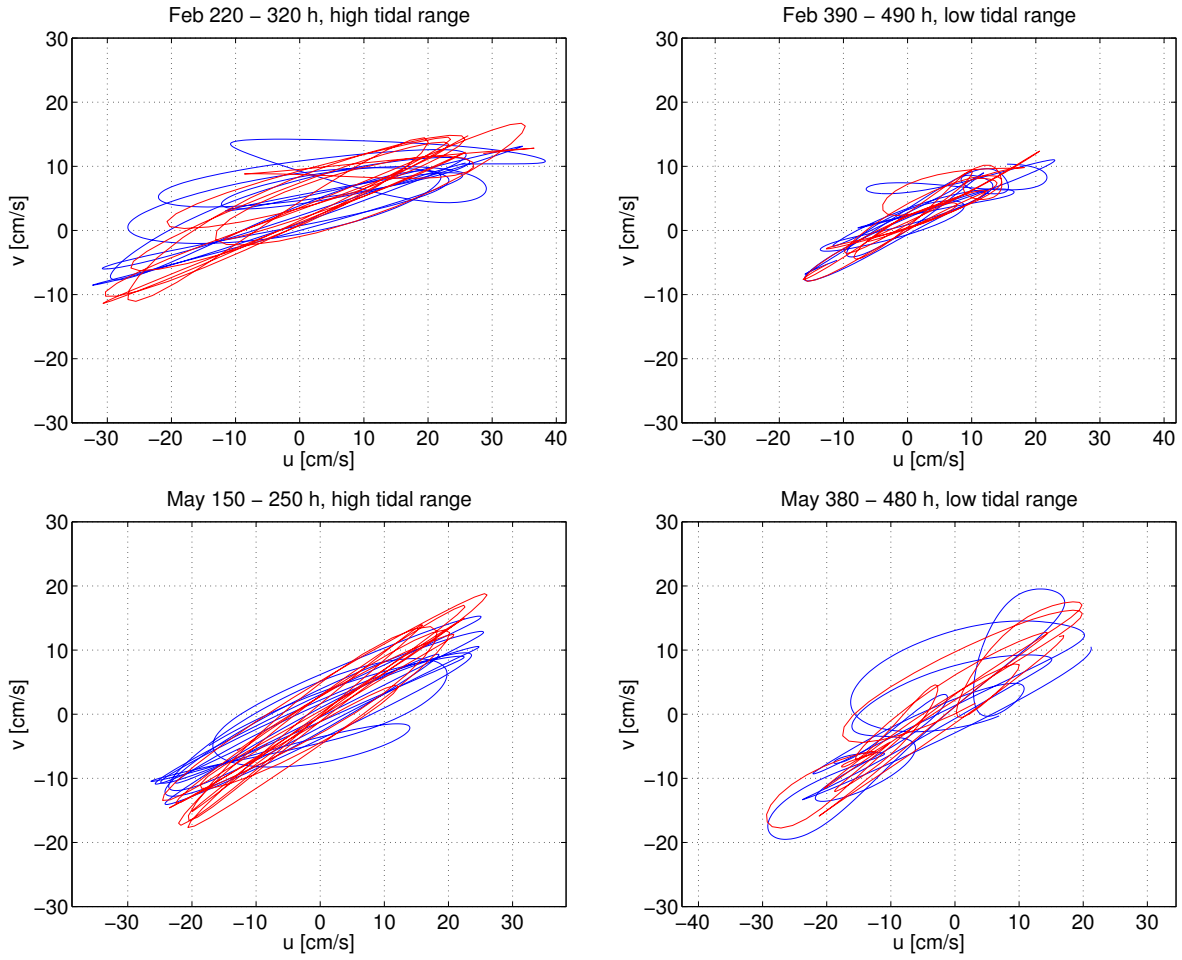

Figure 63: Velocity plots in the horizontal plane for periods of low or high tidal range. Red lines denote field data, while blue lines denote model results. The velocities shown are from an elevation of 9.15 m above the bottom (cell 4), with bottom roughness z_0 = 0.0006 cm.

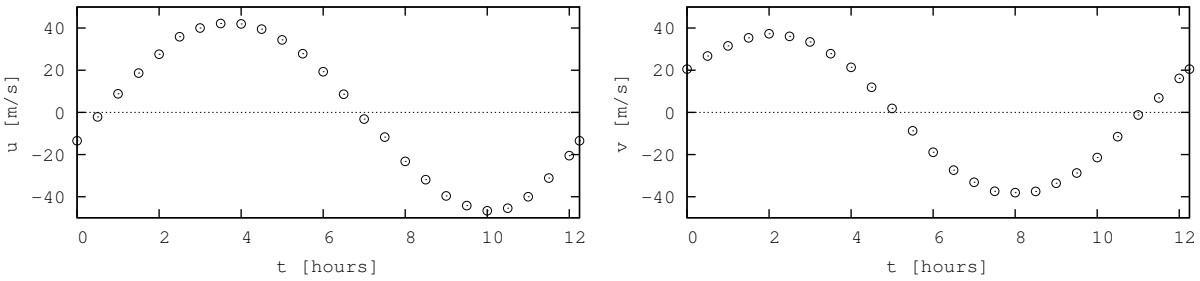

Figure 64: Horizontal velocities 70 m above the sea floor, from the field measurements tabulated by King et al. (1985).

C Results and conclusions from pre-master project work

In the following, the results of a mandatory project work leading up to this master thesis is presented. The project work was made during the fall of 2014. As it is not published, the main results are included here, because they are considered relevant for the present work. The model used in the project work is the same as the one used in the present work, described in chapter 5.

Field data from King et al. (1985) 70 m above the bottom were taken as the free-stream input values (U_0, V_0) for the forcing functions (5.10) and (5.11). The measurements were made in March 1983 in the Celtic Sea about 60 nm west of the Scilly Isles, using a string of current meters. The total water depth was 120 m. King et al. (1985) explain the choice of location by writing *"(...) it has a flat, horizontal, uniform bed that is featureless except for ripples in the silty sand"*. Measurements were done over 11 tidal cycles during the spring tide peak. The measurements were averaged over the ensemble of tidal periods, giving averaged data for one period. The data were found to contain a non-zero mean velocity, which was subtracted from all the values to obtain data for pure oscillatory flow, unaffected by e.g. wind on the surface. The resulting data (i.e. the data used here) is shown in figure 64 (for z=70 m).

C.1 Verification of the model

Results from the present model are compared with the field data from King et al. (1985) in figure 65. The agreement is found to be reasonably good. However, there are clearly discrepancies between the simulation and the field data, especially at the 90 m level and the levels close to the bottom. One possible contribution to these discrepancies is the effect of the bottom roughness height z_0. Soulsby (1990) applied a logarithmic velocity profile to the field data from King et al. (1985) to estimate the effective bottom roughness at different times through the tidal cycle. He found that z_0 varied extensively over the tidal period. The calculated roughness was about $z_0 = 1$ cm at the velocity maxima, and $z_0 = 0.1$ cm at the minima. Soulsby (1990) suggests that the reason for this is that the sand bed was rippled, and that the ripples were aligned such that the crests were normal to the maximum velocity direction. The hypothesis is that the ripples created by the stronger currents were too large for the weaker currents to deform them. Soulsby (1990) concludes that this indicates that *"(...) for accurate modelling of the bottom friction over a mobile sand bed a fixed value of z_0 is an oversimplification"*. In the present model, a constant bottom roughness is applied. Although the bottom friction is not modeled, the variation of z_0 in the field measurements might also influence the flow characteristics, causing deviations between the model predictions and field data. The influence of the bottom roughness on the tidal flow is investigated in chapter C.2. In the simulation shown in figure 65, a bottom roughness of 0.1 cm was applied. Holmedal and Myrhaug (2013) found this to give the best agreements between the model and the field data, using the same model and input data.

C.2 Effect of bottom roughness

The tidal ellipses on several elevations z over the bottom are shown for different values of the bottom roughness z_0 in figure 67. The values of z_0 are adapted from Soulsby (1990), corresponding to typical roughness values for unrippled sand (0.04 cm), gravel (0.3 cm) and rippled sand (0.6 cm). The total depth is 120 m. The expected effect of decreasing velocity close to the bottom for increasing bottom roughness is clearly visible. In addition, it is possible to see that the roughness has an effect on the orientation of the tidal ellipses. The ellipse orientation, given by the angle of the major axis relative to the x-axis, ϕ_{Ra}, is defined in figure

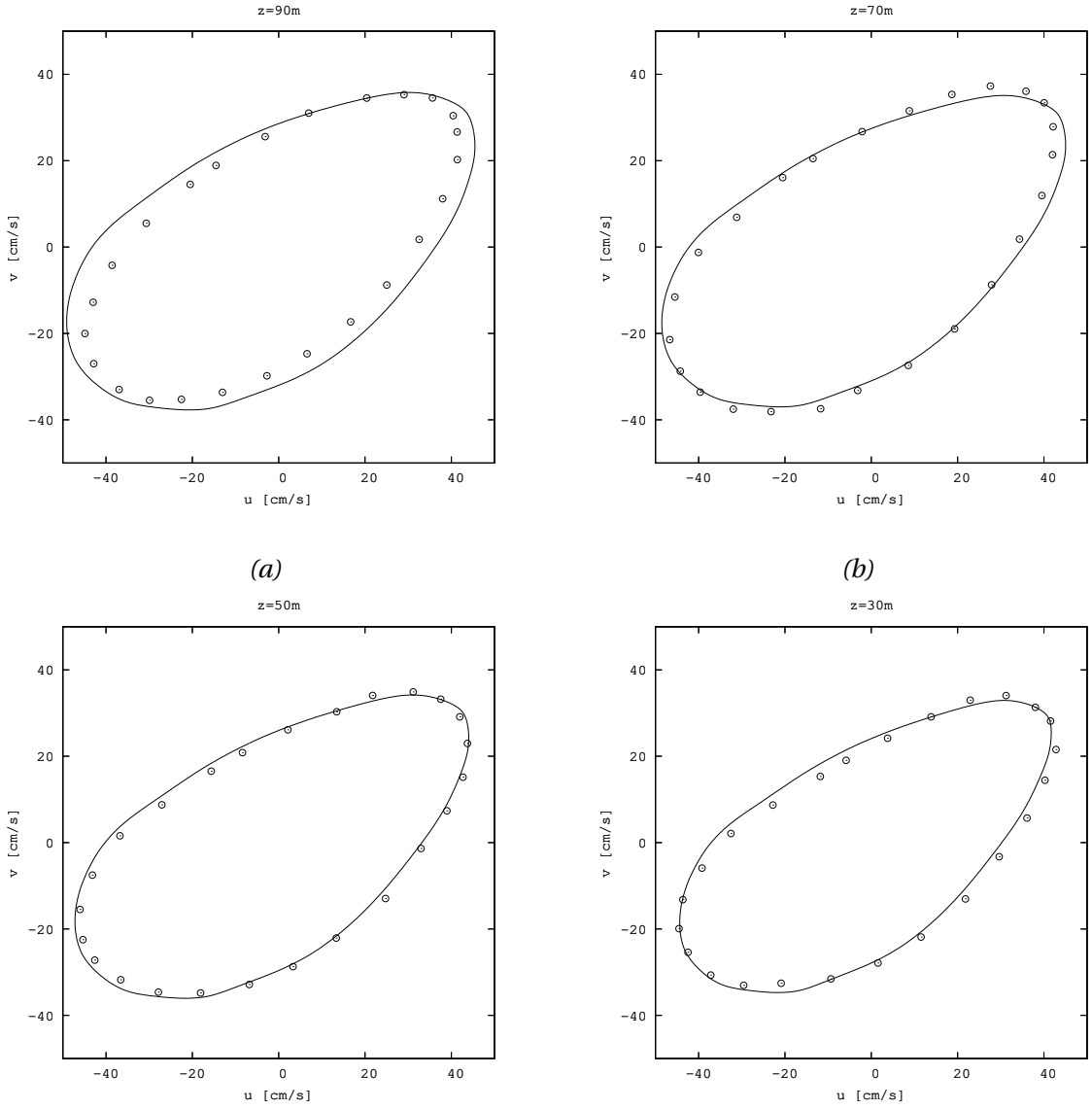

(a) *(b)*

(c) *(d)*

Figure 65: Tidal ellipses obtained from the present model (lines) compared with the field data from King et al. (1985) (circles). For the model results, the bottom roughness was taken as z_0 = 0.1 cm.

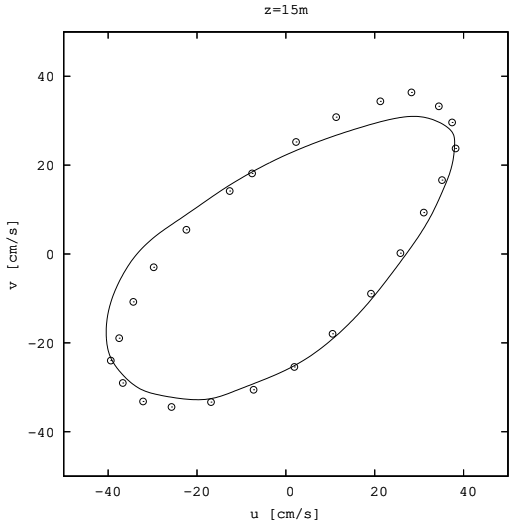

(e)

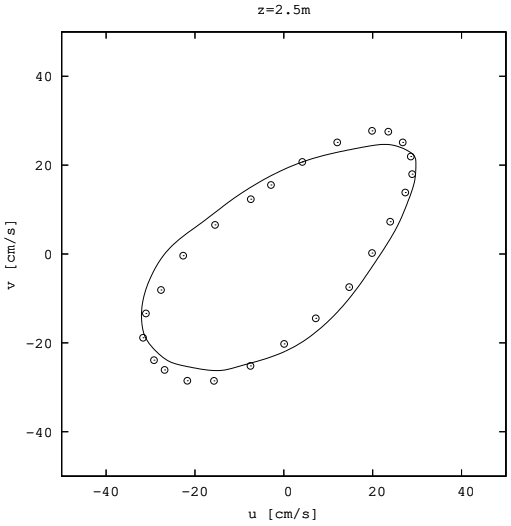

(f)

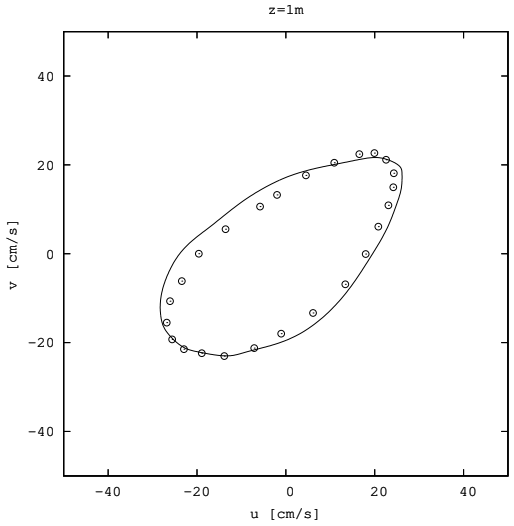

(g)

Figure 65: (continued)

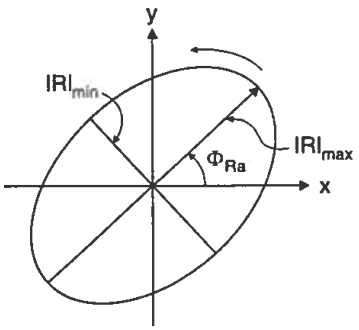

Figure 66: Definition of the tidal ellipse orientation ϕ_{Ra}. The maximum velocity during the tidal cycle is $|R|_{max}$. ϕ_{Ra} is the angle of the maximum velocity relative to the x-axis. (Myrhaug and Slaattelid, 1996).

66. In figure 68 the orientations of the ellipses are plotted for the three values of the bottom roughness. Because the tidal ellipses found here are not perfect ellipses but rather irregular, the major axis is taken as the line going through the origin and the point of highest total velocity $\sqrt{u^2+v^2}$ in the first two quadrants. Figure 68 indicates that the decrease of ϕ_{Ra} for the tidal ellipses very close to the bottom is about 1.2° for an increase of bottom roughness from 0.04 cm to 0.3 cm. A further increase of roughness from 0.3 cm to 0.6 cm gives a reduction of about 0.6°. The orientation difference caused by difference in bottom roughness increases towards the surface. 90 m above the bottom, the decrease is approximately 2.4° and 1.2°, respectively. If we study the orientation of the ellipses at different depths for one value of z_0 isolated, we see that ϕ_{Ra} decreases with increasing z, up to a certain value of z, where it starts to increase. Towards the surface, it seems to converge at an angle smaller than the angle at the bottom. The overshoot angle is visible in figure 68 for bottom roughness 0.04 cm and 0.3 cm. The convergence towards a constant orientation is only seen for roughness 0.04 cm. However, the deviation of the ellipse orientation through the water column is very similar for all three values of z_0. It is therefore reasonable to assume that there would be an overshoot angle and convergence also for the larger roughnesses, for a sufficiently large water depth h.

C.3 Effect of water depth

The effect of the total water depth h on the tidal ellipses is shown in figure 69. In figure 69 (a), i.e. for h=240 m, the outer ellipses are more or less identical, which means that we have a

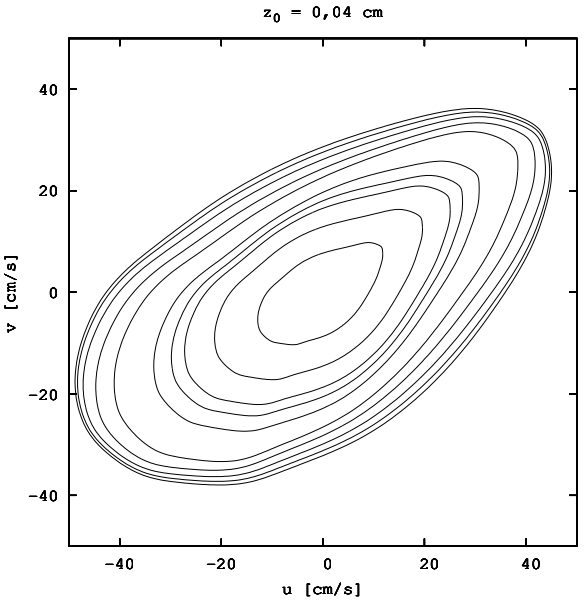

(a)

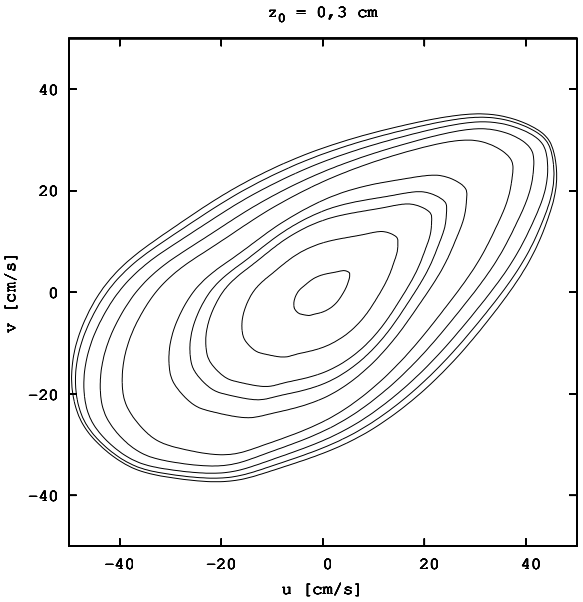

(b)

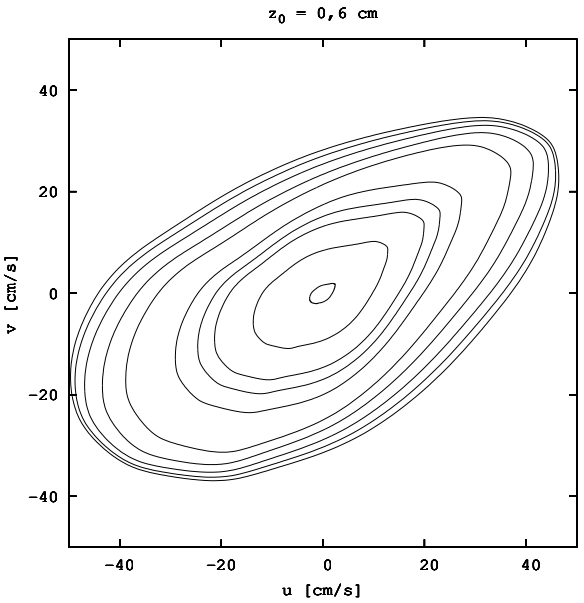

(c)

Figure 67: Effect of bottom roughness z_0 on the tidal ellipses. The ellipses are shown for z-values 0.01 m (inner ellipse), 0.1 m, 0.5 m, 1 m, 2.5 m, 15 m, 30 m, 50 m, 70 m and 90 m (outer ellipse).

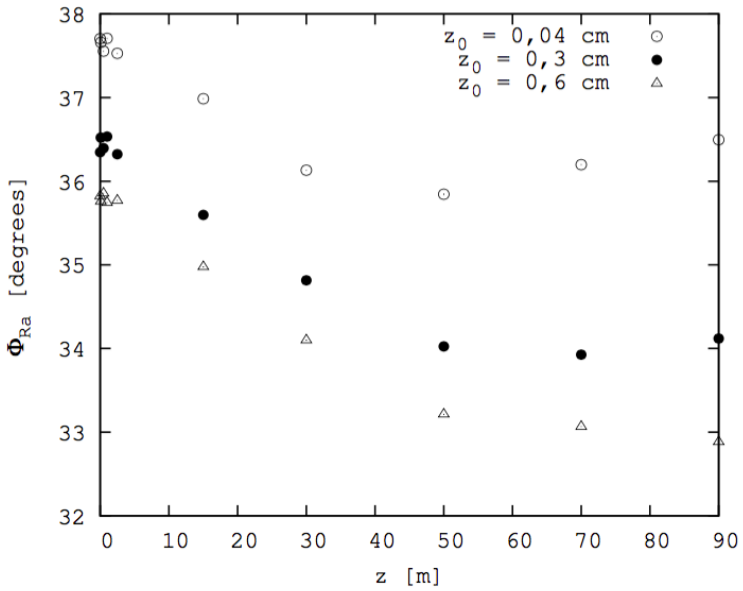

Figure 68: Orientation ϕ_{Ra} of the tidal ellipses as a function of distance from the bottom, z, for three different values of the bottom roughness z_0, corresponding to unrippled sand (0.04 cm), gravel (0.3 cm) and rippled sand (0.6 cm). The total depth is 120 m. The orientation is shown for the same values of z as was used in figure 67.

free stream where the vertical gradients of the horizontal velocities are zero above the bottom boundary layer. The thickness of the boundary layer is not well defined, but the horizontal velocities seems to be close to constant above z=150 m.

In figure 69, the effect of the depth on the orientation of the ellipses is evident. The main effect is that the angle of the major axis, ϕ_{Ra}, increases with increasing total depth. The orientations of the ellipses for different depths are plotted in figure 70. For a depth h=30 m, the orientation angle of the ellipse closest to the bottom (i.e. at z=1 m) is about 23°. A doubling of the water depth to 60 m results in ϕ_{Ra} increasing with about 9°. For an additional doubling of the depth, to 120 m, the angle increases with about 5°. Doubling the depth from 120 m to 240 m gives an increase of slightly more than 1°. This suggests that, for a given set of conditions, there exists a water depth h for which an increase in depth will not alter the direction of maximum tidal current close to the bottom.

The overshoot angle and the convergence towards a constant value of ϕ_{Ra} for increasing z, as discussed for the simulations with different bottom roughnesses, are seen also in figure 70. Figure 68 indicates that, for a given value of h, the orientation angle ϕ_{Ra} will decrease all the way up the surface (i.e. we will not experience an overshoot angle) for high values of z_0. Figure 70 indicates that, for a given value of z_0, the same applies for small values of h. This implies a coupling of the effects of bottom roughness and depth, so that z_0/h is an important parameter for the orientation of the tidal ellipses.

The above discussed properties of the tidal ellipses could possibly be strongly dependent of the thickness of the boundary layer. In figure 71, the boundary layer thickness δ is plotted for the four depths. The values of δ are found visually from plots of the velocity profiles. Since δ is not well defined, the values are somewhat arbitrary. However, the trends should be representable. For a depth of 30 m, the boundary layer was found to cover the whole depth (i.e. there is no free stream, $\delta = h$). For the greater water depths, there is a free stream in the upper layer. In figure 71, the relation between δ and h for these depths seems to be close to linear. Convergence of δ could have implied dependency of the boundary layer thickness on the ellipse orientation. However, with the present results, it is not clear to the author to what extent the orientation angle ϕ_{Ra} depends on the boundary layer thickness δ.

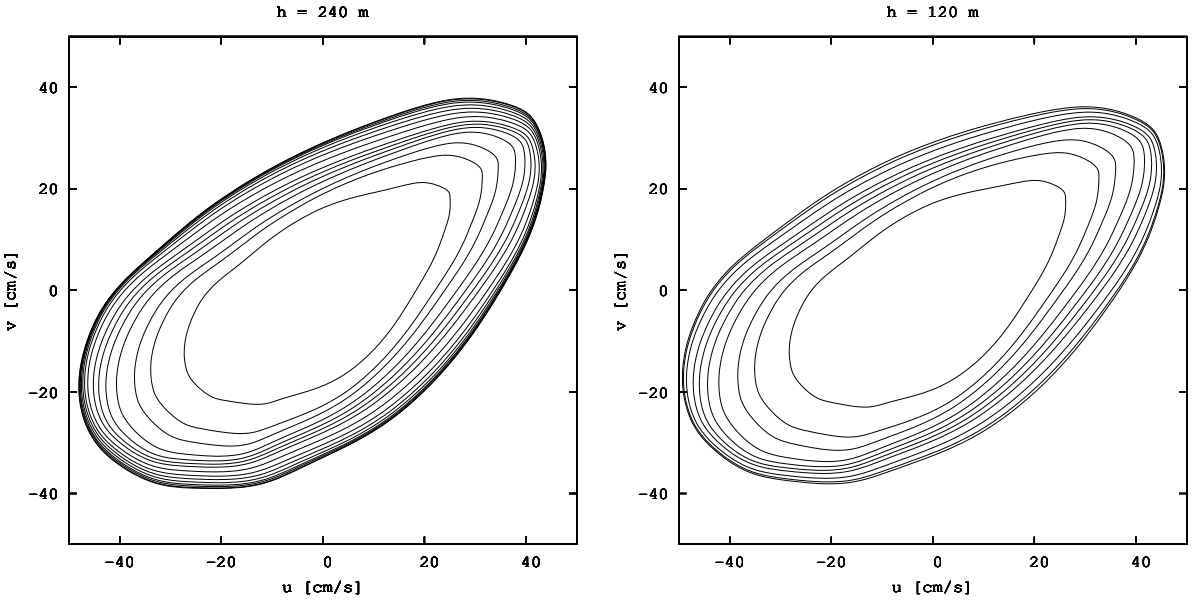

(a) *(b)*

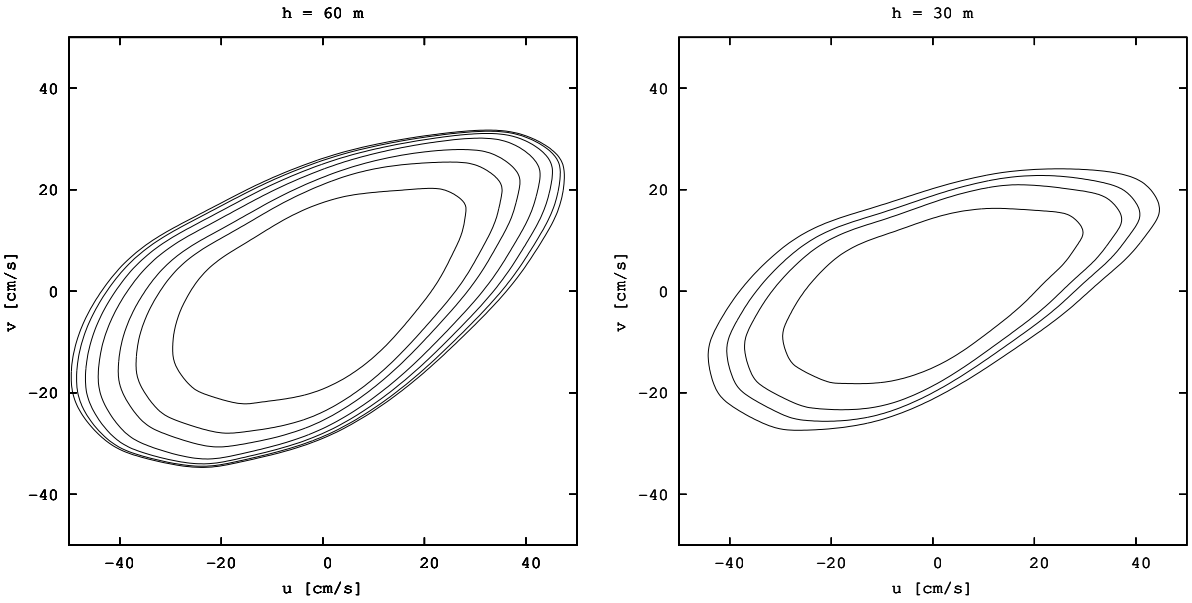

(c) *(d)*

Figure 69: Effect of total depth h on the tidal ellipses. The ellipses are shown for z-values (1, 5, 10, 20, 30, 40, 50, 70, 90, 110, 131, 152, 170, 193, 211) m. The inner ellipse is for z = 1 m for all four figures. The outer ellipse is for z = 211 m in (a), z = 110 m in (b), z = 50 m in (c) and z = 20 m in (d). The bottom roughness is 0.01 cm.

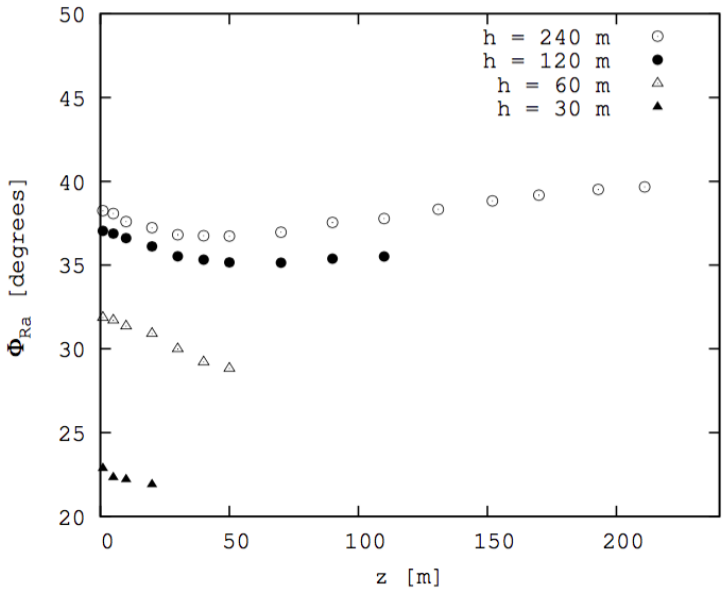

Figure 70: Orientation ϕ_{Ra} of the tidal ellipses as function of distance from the bottom, z, for four different values of the total water depth h. The bottom roughness is 0.01 cm. The orientation is shown for the same values of z as was used in figure 69.

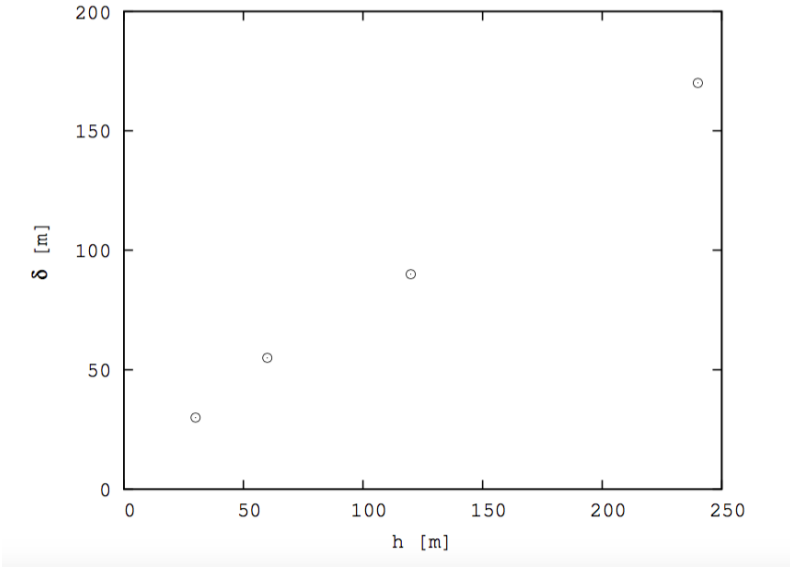

Figure 71: Boundary layer thickness δ for the depths h in figure 69 and 70. The boundary layer thicknesses were found visually from plots of the velocity profiles.

C.4 Conclusions

The present model was compared with the field data from King et al. (1985) and found to comply reasonably well. Effects of bottom roughness and total water depth on tidal flow over a flat bottom were investigated. Special emphasis was given to the effects on the orientations of tidal ellipses. The main conclusions are:

- With the field data from King et al. (1985) taken as input for the forcing function, the main axes of the tidal ellipses are oriented from the south-west to the north-east. In general, the orientation angle at all depths decreases with increasing bottom roughness and with decreasing total water depth, such that the main axes are rotated to a direction closer to the x-axis (west-east).

- For a total water depth of 120 m, the bottom roughness affects the ellipse orientation through the whole water column. The effect increases towards the surface. For a sufficiently small bottom roughness, the orientation angle decreases up to a certain height over the bottom, where it starts to increase, before it converges towards the surface. For larger bottom roughnesses there is no overshoot angle, meaning that the angle decreases with increasing height over the bottom all the way up to the surface.

- The effect of total water depth is very similar to the effect of bottom roughness. For a sufficiently large water depth, the characteristic overshoot angle and convergence of the orientation angle towards the surface are evident. For shallower water, these effects vanish.

- For the values of bottom roughness and depths investigated in the project work, the effect of total depth is much more significant than the effect of bottom roughness. Increasing the bottom roughness from a value corresponding to unrippled sand to one corresponding to rippled sand resulted in a decrease of the orientation angle of about 2° close to the bottom. For a decrease of the total water depth from 240 m to 30 m, the angle was decreased with about 15°.

- The results suggests a coupling between the effects of bottom roughness and total depth. However, this needs to be analyzed further.

D Deduction of the surface Ekman layer

We consider the surface boundary layer induced by wind. The interior flow is considered to be geostrophic, with velocities given by (u_g, v_g). The fluid is considered homogeneous.

The simplified momentum equations for a boundary layer of incompressible fluid can be written as (see e.g. Cushman-Roisin, 1994):

$$\text{x-momentum: } \frac{\partial u}{\partial t} + u\frac{\partial u}{\partial x} + v\frac{\partial u}{\partial y} + w\frac{\partial u}{\partial z} - fv = -\frac{1}{\rho}\frac{\partial p}{\partial x} + \nu\frac{\partial^2 u}{\partial z^2} \tag{D.1}$$

$$\text{y-momentum: } \frac{\partial v}{\partial t} + u\frac{\partial v}{\partial x} + v\frac{\partial v}{\partial y} + w\frac{\partial v}{\partial z} + fu = -\frac{1}{\rho}\frac{\partial p}{\partial y} + \nu\frac{\partial^2 v}{\partial z^2} \tag{D.2}$$

$$\text{z-momentum: } \frac{\partial p}{\partial z} = 0 \tag{D.3}$$

$$\text{Continuity equation: } \frac{\partial u}{\partial x} + \frac{\partial v}{\partial y} + \frac{\partial w}{\partial z} = 0, \tag{D.4}$$

where (u, v, w) are the velocity components in the (x, y, z) directions, respectively. f is the Coriolis parameter, ρ is the water density and ν is the kinematic viscosity. p is the dynamic pressure. These equations are often referred to as the *boundary layer equations*. The basis of the simplification is that, in a boundary layer, the vertical velocities are much smaller than the horizontal velocities. This can be shown by a scale analysis.

To simplify the equations, we restrict the vertical velocity w to be zero in the boundary layer. The flow is considered to be stationary, so that the time-dependent terms vanish. The wind and the geostrophic flow are considered uniform, so that the flow in the boundary layer is uniform in the horizontal plane. Subjected to these assumptions, our governing equations are reduced to

$$-fv = -\frac{1}{\rho}\frac{\partial p}{\partial x} + \nu\frac{\partial^2 u}{\partial z^2} \tag{D.5}$$

$$fu = -\frac{1}{\rho}\frac{\partial p}{\partial y} + \nu\frac{\partial^2 v}{\partial z^2} \tag{D.6}$$

$$\frac{\partial p}{\partial z} = 0. \tag{D.7}$$

The continuity equation remains unchanged. The boundary conditions are

$$u = u_g, \;\; v = v_g \text{ towards the geostrophic flow } (z \to -\infty) \tag{D.8}$$

$$\rho\nu\frac{\partial u}{\partial z} = \tau_x, \;\; \rho\nu\frac{\partial v}{\partial z} = \tau_y \text{ at the surface } (z = 0). \tag{D.9}$$

As stated by Cushman-Roisin (1994), it follows from (D.7) that the dynamic pressure is the same at all depths, including both the boundary layer and the interior (geostrophic) flow. Hence, the horizontal gradients of p are constant through the water column. The governing equations (D.5) and (D.6) subjected to the boundary conditions towards the geostrophic flow give

$$-f v_g = -\frac{1}{\rho}\frac{\partial p}{\partial x} \tag{D.10}$$

$$f u_g = -\frac{1}{\rho}\frac{\partial p}{\partial y}. \tag{D.11}$$

The last terms of (D.5) and (D.6) are set to zero because there is no friction in the interior flow. We have now found a relation between the horizontal pressure gradients and the geostrophic velocity. Inserted in the governing equations (D.5) and (D.6) this gives

$$-f(v - v_g) = \nu\frac{\partial^2 u}{\partial z^2} \tag{D.12}$$

$$f(u - u_g) = \nu\frac{\partial^2 v}{\partial z^2}. \tag{D.13}$$

To solve these equations under the given boundary conditions, we start by defining $U = u + iv$, where i is the imaginary unit satisfying $i = \sqrt{-1}$. By multiplying (D.13) with i and adding the resulting equation and equation (D.12), we obtain

$$\nu\frac{\partial^2}{\partial z^2}U = if(u + iv) - if(u_g + iv_g). \tag{D.14}$$

Further, we define $U_g = u_g + iv_g$, so that

$$\nu\frac{\partial^2}{\partial z^2}U = ifU - ifU_g. \tag{D.15}$$

We also define the *defect velocity* $U_d = U - U_g$. Since U_g is a constant, we can write

$$\frac{\partial^2}{\partial z^2}U - \frac{\partial^2}{\partial z^2}U_g = i\frac{f}{\nu}U_d, \tag{D.16}$$

XXX

which can be written as

$$\frac{\partial^2}{\partial z^2}U_d - i\frac{f}{\nu}U_d = 0. \tag{D.17}$$

This is a second order ordinary differential equation (ODE), which has the solution

$$U_d(z) = Ae^{\lambda_1 z} + Be^{\lambda_2 z},$$

where λ_1 and λ_2 are the roots of the characteristic equation

$$\lambda^2 + a\lambda + b = 0.$$

The solution of the ODE is then

$$U_d(z) = Ae^{\sqrt{i\frac{f}{\nu}}z} + Be^{-\sqrt{i\frac{f}{\nu}}z}. \tag{D.18}$$

The boundary condition towards the interior flow, $U_d(z \to -\infty) = 0$, gives B=0. Given the definitions we have made for U, U_g and U_d, we see that we can write

$$\frac{\partial U_d}{\partial z} = \frac{\partial u}{\partial z} + i\frac{\partial v}{\partial z}. \tag{D.19}$$

Inserting the boundary conditions at the surface, equation (D.9), we get an expression for A leading to

$$U_d = \frac{1}{\rho\sqrt{if\nu}}(\tau_x + i\tau_y)e^{\sqrt{i\frac{f}{\nu}}z}. \tag{D.20}$$

We would now like to extract the i's from the square roots. By using the relation $i = e^{i\frac{\pi}{2}}$ and Euler's formula $e^{ix} = \cos(x) + i\sin(x)$, we can show that

$$\sqrt{i} = \frac{\sqrt{2}}{2}(1+i)$$
$$\frac{1}{\sqrt{i}} = \frac{\sqrt{2}}{2}(1-i).$$

By inserting this in (D.20) and by using Euler's formula, we get

$$U_d = \frac{\sqrt{2}}{2}\frac{1-i}{\rho\sqrt{f\nu}}\left(\tau_x + i\tau_y\right)e^{\frac{z}{d}}\left\{\cos(\frac{z}{d}) + i\sin(\frac{z}{d})\right\}, \tag{D.21}$$

where d is a distance defined by

$$d = \sqrt{\frac{2\nu}{f}}. \tag{D.22}$$

This can be rewritten as

$$U_d = \frac{1}{\rho f d} e^{\frac{z}{d}} \left[\tau_x \left(\cos(\frac{z}{d}) + \sin(\frac{z}{d}) \right) + \tau_y \left(\cos(\frac{z}{d}) - \sin(\frac{z}{d}) \right) + i \left\{ \tau_x \left(\sin(\frac{z}{d}) - \cos(\frac{z}{d}) \right) + \tau_y \left(\sin(\frac{z}{d}) + \cos(\frac{z}{d}) \right) \right\} \right] \tag{D.23}$$

It can be shown that

$$\begin{aligned}
&\cos(\frac{z}{d}) + \sin(\frac{z}{d}) = \sqrt{2}\cos(\frac{z}{d} - \frac{\pi}{4}), \\
&\cos(\frac{z}{d}) - \sin(\frac{z}{d}) = -\sqrt{2}\sin(\frac{z}{d} - \frac{\pi}{4}), \\
&\sin(\frac{z}{d}) - \cos(\frac{z}{d}) = \sqrt{2}\sin(\frac{z}{d} - \frac{\pi}{4}).
\end{aligned}$$

By inserting this in (D.23) and using the definitions of U_d and U_g, we get

$$U = u_g + i v_g + \frac{\sqrt{2}}{\rho f d} e^{\frac{z}{d}} \left[\tau_x \cos(\frac{z}{d} - \frac{\pi}{4}) - \tau_y \sin(\frac{z}{d} - \frac{\pi}{4}) + i \left(\tau_x \sin(\frac{z}{d} - \frac{\pi}{4}) + \tau_y \cos(\frac{z}{d} - \frac{\pi}{4}) \right) \right] \tag{D.24}$$

It follows from the definition of U that

$$\begin{aligned}
&u = \mathrm{Re}\{U\}, \\
&v = \mathrm{Im}\{U\}.
\end{aligned}$$

This implies

$$u = u_g + \frac{\sqrt{2}}{\rho f d} e^{\frac{z}{d}} \left\{ \tau_x \cos(\frac{z}{d} - \frac{\pi}{4}) - \tau_y \sin(\frac{z}{d} - \frac{\pi}{4}) \right\} \tag{D.25}$$

$$v = v_g + \frac{\sqrt{2}}{\rho f d} e^{\frac{z}{d}} \left\{ \tau_x \sin(\frac{z}{d} - \frac{\pi}{4}) - \tau_y \cos(\frac{z}{d} - \frac{\pi}{4}) \right\}, \tag{D.26}$$

where d is defined by (D.22). The equations (D.25) and (D.26) describe the surface Ekman layer.